The Tensile Properties and Toughness of Microstructures Relevant to the HAZ of X80 Linepipe Steel Girth Welds

by

Michael J. Gaudet

B. Applied Science in Materials Science and Engineering, University of Toronto, 2007

A THESIS SUBMITTED IN PARTIAL FULFILLMENT
OF THE REQUIREMENTS FOR THE DEGREE OF

Doctor of Philosophy

in

THE FACULTY OF GRADUATE AND POSTDOCTORAL STUDIES
(Materials Engineering)

The University of British Columbia
(Vancouver)

August 2015

Abstract

In the transportation of oil and gas products from and over remote locations, such as Canada's Arctic environment, pipelines are used. Girth welding to join sections of steel pipelines creates a substantial heat affected zone (HAZ) within the base pipeline steel. While there is significant concern as to the fracture and mechanical properties of the HAZ as whole, detailed knowledge about the mechanical properties of the microstructural constituents is lacking. For this research, measurements of the temperature time profile in the HAZ of single and dual torch welds were made. This was then used to guide heat treatments of X80 steel in a Gleeble simulator to create samples of 8 different bulk microstructures with differing amounts and morphologies of bainite, ferrite and martensite-retained austenite (MA). From the heat treated samples tensile and Kahn tear test specimens were made for testing at ambient, -20°C, and -60°C. The highest strength microstructure proved to be the finest, lower bainitic microstructure, while the lowest strength microstructure was the coarsest, upper bainitic sample containing a significant amount of MA. This was observed to be true at all testing temperatures. As part of the tensile behaviour investigation, the Bouaziz dislocation based model for work hardening was applied and shown to fit well across all temperatures and conditions. The Kahn tear test, a machine notched, thin-sheet, slow strain rate test, showed all tests failed in a ductile manner. Relative toughness measurement from this test showed that the fine, lower bainitic microstructure was the toughest and the coarse, ferritic microstructure was the least tough. This work presents a novel measurement of dual torch temperature time profiles in a real HAZ, an extensive mechanical testing program of isolated microstructures relevant to the X80 HAZ at potential pipeline operating temperatures, and an applied a robust model to fit the work hardening behaviour for all conditions. This work has the potential for future application in microstructure evolution-property models, and in a combined mechanical model of the different microstructures to further improve understanding of HAZ mechanical responses.

Preface

Portions of the text were taken and modified with permission of myself, as the author, from the publications of M.J. Gaudet and W.J. Poole, "Tensile Behaviour and Fracture Properties of X80 Linepipe Steel", Materials Science & Technology 2011, pages 717-724, M.J. Gaudet and W.J. Poole, "Tensile Behaviour and Fracture Properties of X80 Linepipe Steel", Iron & Steel Technology, August 2012, 99-104, and M.J. Gaudet and W.J. Poole, "Tensile and fracture properties of X80 steel microstructures relevant to the HAZ." 2012 9th International Pipeline Conference, American Society of Mechanical Engineers, 2012. Figures 4.6, 4.7, 4.12, 5.6, and 5.7 were modified from these publications and used within. In these publications, I wrote the entirety of the manuscripts, created the figures, and performed the experiments with my supervisor, W.J. Poole, providing discussion points and editing support.

Dr. Warren Poole provided much input and support that guided this work, but specifically assisted in the initial analysis using the Bouaziz model. Gary Lockhart provided help with the design, and technical support for the weld trials held at Evraz NA Inc in Regina. Chris Penniston formerly of Evraz NA Inc was in charge of the selection of weld procedures to use, as well as the setup and operation of the welding equipment during the weld trials. Etienne Caron developed the methods used to analyze the data from the weld trials that I modified and applied. Fateh Fazeli assisted in the modification of the cooling setup of the Gleeble 3500 for my experiments. Jennifer Reichert provided assistance in the methods used for the characterization of my microstructures as well as data from her own characterization work for comparison. Quentin Puydt modeled the triaxial stress state of flat strip tensile specimens that allowed for my correction to observed final fracture stress. Thomas Garcin provided microstructure evolution model results using my Gleeble heat treatment data to compare with my observed microstructures from metallography. Design of the Kahn testing rig was made by myself and fabricated by the Materials Engineering machine shop.

Table of Contents

List of Tables

List of Figures

List of Symbols

t_{8-5}	Time to cool from 800 °C to 500 °C.
γ	The austenite phase of steel.
α	The ferrite phase of steel.
MA	The mixed phase of martensite and austenite in steel.
T_{start}	The transformation start temperature upon cooling from the austenite phase in steel.
σ_0	The intrinsic lattice strength of a microstructure.
σ_{ss}	The solid solution strengthening component of a microstructure.
σ_{ppt}	The precipitate strengthening component of a microstructure.
σ_{dis}	The dislocation strengthening component of a microstructure.
σ_{gb}	The grain boundary strengthening component of a microstructure.
ρ_{dis}	The dislocation density.
$\sigma_{\text{ys 0.5\% offset}}$	Yield strength as determined using the 0.5% offset strain method.
σ_{UTS}	The ultimate tensile strength.
ε_{UEL}	Engineering strain at the point of final uniform elongation (i.e. necking point).
ε_{frac}	True strain at the point of final fracture in a tensile test.
σ_{frac}	True stress at the point of final fracture in a tensile test.
θ	The work-hardening rate.
$\sigma_{ys\ 0}$	Work-hardening model parameter related to initial yield stress.
ξ	Characteristic length scale related to capture distance for dynamic recovery.
σ_{tear}	The tear strength from a Kahn tear test.
UPE_{d0-1}	The unit propagation energy in a Kahn tear test from max load to 1 mm of further pin-to-pin displacement.
E_{tear}	The energy of tearing in a Kahn tear test, calculated in this study from 0 to 3 mm of crack length.

Acknowledgments

This research was made possible through the support of the project industry sponsors, Evraz Inc. NA and TransCanada PipeLines Ltd., and the Natural Sciences and Engineering Research Council of Canada (NSERC).

I am grateful to be surrounded by a great number of people that have been supportive and understanding during my research. I wish to first thank my supervisor Dr. Warren Poole for his continued support and inspiring discussions throughout the entirety of my time here. I wish to thank all of the members that have been a part of the X80 project here at UBC, but in particular for their assistance of my own work by action or through discussion, Dr. Matthias Militzer, my friend Jenny Reichert, Mehran Maalekian, Gary Lockhart, Fateh Fazeli, Thomas Garcin, Quentin Puydt, Morteza Toloui, and Etienne Caron. Jacob Kabel provided assistance to me while working with the SEM, and has grown to be a friend. The support of the machine shop, Ross Mcleod, Carl Ng, and Dave Torok at UBC was crucial for my work, particularly for helping me with my Kahn tear testing rig. Wonsang Kim consistently provided quick assistance with minor issues with testing equipment. Michelle Tierney was always a friendly expert at helping me with handling the administrative side of UBC from the start to the end.

Outside of those that have been directly involved with my work I am thankful to have a number of people that I have been able to rely on for support. I give a very deep thanks to my colleagues and best of friends, Beth Sterling and Phil Tomlinson whose experience, intelligence, humour and insight have provided much motivation and support at the most challenging times. I have been fortunate to have had many friends outside of the program, of these I wish to thank Stephen Kim, Alison Schatz, Joanna Palermo, Elaine Fuertes and Patrick Bielstein, Seth and Claire Gilchrist, Sabrina Higgins, and Raymond Jones for their support, kindness and friendship. While I may not be the best at staying in contact, I wish to thank those friends I made from back in my life back in

Toronto and Oakville who always are able to pick up our friendship where we left off; Lily Cheng, Geoff Young, Michael Favero, Clarence Chiu, and Thomas Arato.

Finally, may these few words impart the depth of my gratitude; I wish to give the biggest thanks of all to my family, both those living and those passed, for their unwavering support that has always provided a comfort and for which I will remain eternally grateful. Except for my brother Andrew, who despite our friendship apparently never got over the fact that his bike broke because of a poor weld in 2007 [A. Gaudet, UBC Doctoral Thesis, 2010, pg. xv]. Considering there was that time he forgot to gas up the Jimny in the mountain range south of San José, Costa Rica in 2012, forcing us to coast down a mountain in neutral for half an hour in the rain, I think we are even.

CHAPTER 1

Introduction

1.1 Introduction

In North America, significant oil and gas reserves can be found in remote locations that have yet to be fully developed. To access these reserves requires transportation of these resources from the extraction sites to refineries and distribution centres. Pipelines have proven to be the most efficient, safe, and economical way to transmit these resources over the long distances required. However in more extreme environments, such as the Arctic, there are a number of technical and financial challenges facing pipeline design, construction, and operation. In order to make future projects viable, these challenges must be overcome through the research and development, in particular, of materials.

Steel is well established as the material of choice for long distance transmission of oil and gas resources. Higher strength steels, such as X80 or X100 grades have been shown to be more cost effective than conventional steels and are of importance for the so-called strain based design approach [1–5] . Strain based design for pipelines puts an additional demand on linepipe steels by setting a limiting strain value, typically 0.5%, to which the steel must remain structurally stable. Axial strains arise in all pipelines, but for pipelines traversing permafrost like the Alaskan Pipeline, Mackenzie Valley Pipeline, and the Northern Gateway Pipeline, these axial strains are of particular concern due to issues such as frost heave and thaw settlement [6–9]. It is in important to gain a more complete understanding the mechanical behaviour, specifically the yield and initial work hardening

response, for these new strain-based design grades of steel.

In construction of transmission pipelines, joining sections of pipe requires girth welding in the field. With more remote locations, and in extreme environments, any improvements to welding productivity results in significant time and thus cost savings. Pipeline girth welding is typically performed using a gas metal arc welding (GMAW) process in which a single weld torch deposits weld metal in the joint. To fully weld the thickness of a typical transmission pipeline requires multiple passes of the single weld torch. One proposed change to this process is to add a second welding torch which trails the first torch at a set distance (typically 50 to 200 mm) during certain passes. Consequently fewer passes would be required in this so-call dual torch welding compared to the typical welding procedure and this productivity gain resulting in a significant cost reduction for welding in the more remote and extreme environments. For comparison, if a single pass of around a 30" diameter pipe requires 2.5 minutes and requires 7 passes in total, replacing two passes with the dual torch procedure could potentially reduce total welding time by 5 minutes i.e. greater then 25% savings in welding time.

Both single and dual torch welding cause changes to the microstructure, mechanical properties, and toughness in the region of the base linepipe steel adjacent to the weld. This region, the so-called heat-affected zone (HAZ), exhibits variations dependent on the temperature-time profile, termed the thermal cycle, experienced at a given point in the HAZ. The HAZ in a dual torch weld may be more complex then a single torch HAZ due to the fact that heat flows from the two torches interact to cause complicated thermal cycles resulting in greater variation of microstructure and properties. As well, the influence of multiple passes of the welding torch also leads to variations of microstructure and properties. Regardless of which process is used, the HAZ from girth weld operations will result in a highly complex situation with relations between the welding process, the resulting thermal cycles, and the final observed microstructures and properties.

Considering the cost reduction opportunities of using higher strength steel in strain based designed pipelines and utilizing new, higher productivity welding practices it is of interest to gain further understanding into the most pertinent challenges. The HAZ, being a complex region that may show less desirable properties is of particular concern to applying these higher strength grades and more productive welding processes. While there is a large amount of literature on testing of welds, there is very little research on the local response within the HAZ beyond the use of simple

hardness values. The research proposed here is to examine the microstructures observed in the HAZ in multipass welds with both single and dual torch procedures, isolate and then generate pertinent microstructures in bulk samples that then can be tested for their mechanical properties. This research will use a commercially produced steel pipe of X80 chemistry that is appropriate for strain based design.

CHAPTER 2

Literature Review

2.1 Steel in Oil and Gas Pipelines

High strength low alloy (HSLA) steels with microalloying additions have been used extensively to meet design criteria as pipelines moved to increasingly high strength grades. These alloys are typified by low carbon contents (i.e. between 0.05-0.25 wt%), with an amount of manganese up to 2 wt%, and microalloying constituents of molybdenum, nickel, copper, niobium, titanium, vanadium, and boron which total less then 1 wt% [10, 11]. The highest strength grades for pipelines typically have lower carbon contents, in the range of 0.03-0.06 wt% . These steels are fabricated into plates for pipelines using thermomechanical controlled processing (TMCP) [12]. TMCP is a series of processes starting with heating a steel slab into the austenitic phase then deforming the steel at a temperature below the recrystallization temperature. This deformation refines the grain size and shape as well as increases the dislocation density which impacts the transformation upon cooling. Immediately following this deformation, accelerated cooling is applied to the slab before coiling to control the phase transformation. With careful control over the alloying, deformation, and cooling the final microstructure is typically very fine, composed ideally of acicular ferrite or bainite, resulting in high strengths [10, 13]. For X80 steels, the typical microstructure observed is a mixture of mainly fine grain ferrite and bainite [12]. To form the plates into the pipelines, typically either a spiral mill process [3], or the double-bend then expansion process [14] is used. Spiral mill pipes are made by applying a constant bending radius to the steel plate at a certain angle and then welding

the seams along the formed tube. In the double bend then expansion process the plate is formed into a U, then O, and then is expanded and welded along the longitudinal seem and is termed the UOE process. These processes both create a length of pipeline that is then shipped to the pipeline construction site, ready to be girth welded to form the transmission pipeline.

A basic understanding of the metallurgy of these HSLA pipeline steels provides a context to discuss the effects of welding and the HAZ, particularly with regard to how it relates to mechanical and fracture properties. This understanding begins with a discussion of typical phases and microstructures observed in HSLA linepipe steels, and then the role steel chemistry with respect to specific alloying elements.

Figure 2.1 shows the typical phase diagram of the iron-carbon system at low carbon contents. Over a range of elevated temperatures and low carbon content, only the face-centered cubic (FCC) austenite (γ) phase is seen. This ductile phase has a high solubility for carbon. Cooling from austenite results in solid phase transformation into various microstructures. At ambient

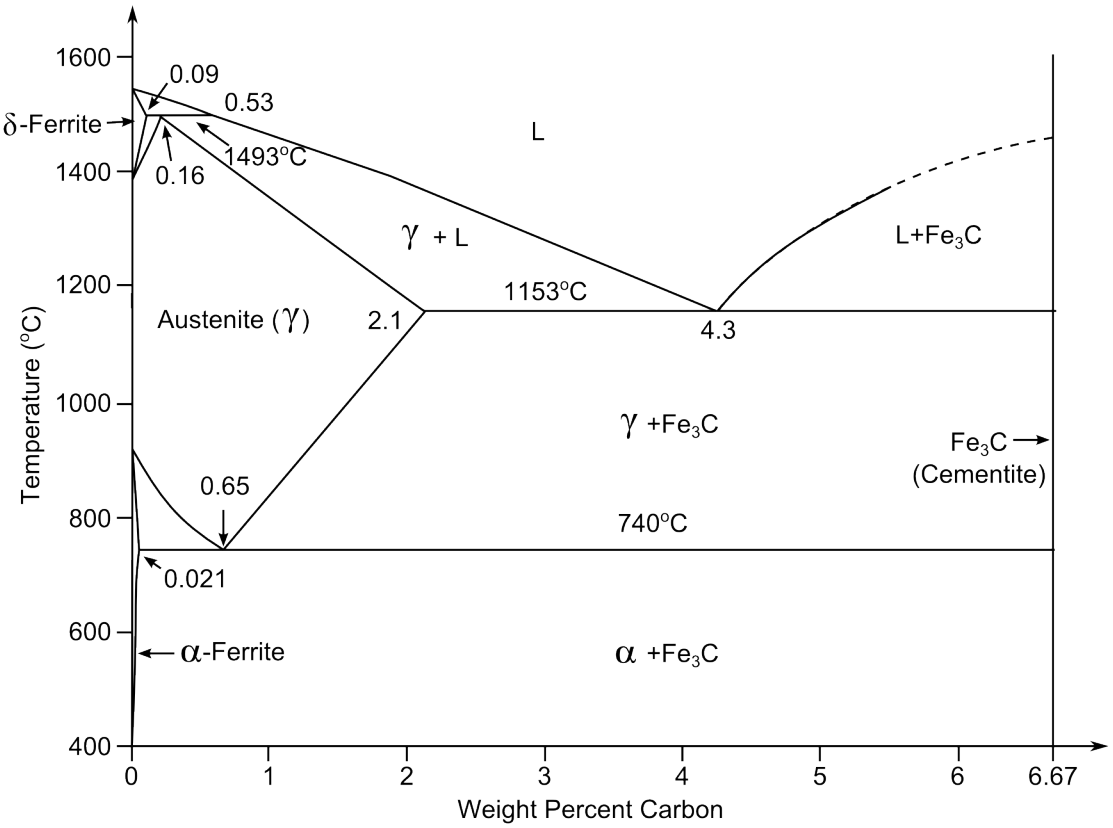

Figure 2.1: Fe-C phase diagram with C content relevant for steels, based on data from [15].

temperatures the primary equilibrium phase consists of α-ferrite, which has a body-centered cubic (BCC) structure with a low carbon content. Relative to other phases that can be produced, α-ferrite is a ductile, low strength phase [10]. The other equilibrium phase at ambient temperatures is iron-carbide (Fe_3C), also called cementite. Fe_3C is a strong but brittle phase that will be found as plates in a ferrite-Fe_3C sandwich structure (i.e. pearlite) if the cooling rate is slow enough.

As non-equilibrium cooling is typical in both the production of HSLA pipeline steels and in their HAZ, the microstructures and phases that can be produced differ vastly from what is represented in the the equilibrium phase diagram. At slow cooling rates, the austenite decomposes into a primarily ferritic phase where the grains are fairly equiaxed and is often called polygonal ferrite. At slightly faster cooling rates, an orientation relationship between the growing ferrite and parent austenite phase develops resulting in an acicular ferrite microstructure. At faster cooling rates, bainitic microstructures are seen. Upper bainite structures are bainitic structures formed at higher temperatures and are typified by packets of lath-shaped sheaves of ferrite with carbides that have had time to form between sheaves of the progressing ferrite-austenite interface [16]. Lower bainite, which forms at lower temperatures and faster cooling rates, is observed again to be packets of lath-shaped sheaves of ferrite but with the less time for diffusion, carbides form much finer and within the ferrite sheaves [16]. At even faster cooling rates, a diffusionless transformation takes place to form metastable martensite. In low carbon steels ($<$0.2% C), the form of martensite seen is a lath-like structure. This martensite phase, with its body-centered tetragonal (BCT) crystal structure and higher carbon content is a considerably harder phase. The relation of these microstructures to the mechanical behaviour is discussed in a later section.

The role of alloying (or residual) elements in HSLA steels and their relation to the microstructure-property relationship is complex. They can directly effect strength through solid solution strengthening, or they may form precipitates that can also add to the strengthening. Beyond direct interactions on physical properties like strength or toughness these alloying elements and/or their precipitates can indirectly effect properties through their interaction with phase transformations, for instance by promoting stability of certain phases or slowing the transformation kinetics. The following is a general summary of the individual role of each these alloying elements, while later sections contain separate and more specific discussion of chemistry effects on microstructure evolution, and of chemistry effects on physical properties.

Carbon

Carbon is found either dissolved into the solid solution at interstitial sites in the lattice or as a precipitate (or carbide) with other elements, such as Fe_3C, MoC, NbC, and TiC. As an interstitial alloying element it gives a very strong solid solution strengthening effect in ferritic microstructures. Carbon precipitates (carbides) are often brittle and with increasing amounts and sizes will lead to decreasing toughness of the steel [10]. The solubility of carbon differs with the structure of the iron lattice. Carbon is more soluble in the austenite phase and will tend to stabilize this phase.

Carbon is a potent strengthener both directly and indirectly through its promotion of martensite, a microstructure often associated with low toughness. A carbon equivalent (CE) is often used to make an empirical comparison of steel chemistries' ability to form high hardness microstructures, and thus is a measure of hardenability. As high hardness microstructures are related to hydrogen induced cold cracking in welds, the carbon equivalent is used also as a measure of the steel's ability to be welded without significant defects, simply referred to as a steel's weldability. Yurioka [17] has provided a good review of weldability and carbon equivalent equations. One such common and simple equation to determine weldability in low carbon steels is given by [17]:

$$P_{cm} = \%C + \frac{\%Si}{30} + \frac{\%Mn}{20} + \frac{\%Cu}{20} + \frac{\%Ni}{60} + + \frac{\%Cr}{20} + \frac{\%Mo}{15} + \frac{\%V}{10} + 5\%B \qquad (2.1)$$

where P_{cm} is the composition parameter, and the percentages of each element are in weight percent. Higher P_{cm} values will be expected to have a higher potential for martensite which is typically an undesirable phase due to its low toughness. P_{cm} values in combination with empirical evidence can be used then to classify a steel's weldability.

Nitrogen

Nitrogen is an interstitial alloying element, and like carbon is very effective as a solid solution strengthener [10]. Similar to carbon, it has greater solubility in the austenite phase then the ferrite phase causing it to precipitate out if the cooling rate is slow enough. Nitrogen, like carbon, will precipitate with other elements. Significant amounts of nitrogen in solution is associated with lower toughness, so it is often controlled by adding nitride forming alloy elements.

Manganese

Manganese is a common alloying element due to its affinity with sulphur (i.e. prevents harmful iron-sulphide inclusions), and its low cost [10]. Furthermore, it provides a moderate solid solution strengthening effect while being a stabilizer to the austenite phase.

Silicon

Silicon is an inexpensive, strong deoxidizer and also acts as a moderate solid solution strengthener [10]. The presence of silicon promotes ferrite formation. At high Si contents, a significant decrease in toughness is observed.

Nickel

Nickel is a strong austenite stabilizer, and thus has a tendency to form martensitic structures [10]. It also promotes acicular ferrite structures over equiaxed ferrite structures, which in turn increases toughness. In a ferrite microstructure, it provides minor solid solution strengthening.

Molybdenum

Molybdenum is a ferrite former, but promotes acicular ferrite over equiaxed ferrite microstructures. This is resulting from its strong retarding effect of the austenite-to-ferrite phase transformation [18]. It has a strong solid solution strengthening effect, but also forms carbide precipitates [10].

Chromium

Chromium is an expensive alloying element that stabilizes ferrite phases and also will form carbides [10]. As a solid solution strengthener it is not effective.

Titanium, Niobium, and Vanadium

Titanium, niobium and vanadium all form carbides and nitrides, often in complexes with each other when all elements are present [10]. With the high temperature stability of the TiN precipitates, austenite grain growth at elevated temperature can be limited. Niobium carbides, nitrides, and carbonitrides add significant precipitation strengthening [10]. These precipitates of Nb are stable to moderately high temperatures in the HAZ and can help keep a refined austenite grain size. Nb has a moderate solid solution strengthening effect. Its presence has been noted to help promote bainitic transformations. The presence of V and its precipitates has been seen to improve strength and toughness through promotion of finer structures such as acicular ferrite and bainite [19]

Residual Elements

Copper is typically a residual element often found in steels produced in electric arc furnaces due to their use of recycled steel. Copper provides solid solution strengthening, while at higher concentrations it forms precipitates but may also cause issues with embrittlement at high temperatures [10]. Sulphur is a residual element that is associated with low toughness and production issues in steel due to the formation of iron-sulphides, a precipitate that causes a number of problems [10]. Additions of manganese are typical, as discussed previously, so as to form manganese-sulphides preferentially over the detrimental iron-sulphides. Phosphorus acts as a strong substitutional solid solution strengthener; however, it segregates to grain boundaries, leading to an embrittlement effect and low toughness [10]. Thus, efforts are taken to limit the amount of phosphorus and sulphur.

2.2 Pipeline Girth Welds

In order to construct a pipeline on site, the individual lengths of pipeline are welded at their ends around the girth typically using a mechanized multipass gas metal arc weld (GMAW) procedure. These girth welded joints, including the resulting heat affected zone (HAZ), need to meet the demands set by the pipeline design [20–24]. Since these joints represent a portion of the pipeline with significantly different properties compared to the base plate, it is an area that has been the focus of many investigations. Research on weld joints in pipeline steel can be broadly categorized into those that study welding process developments [23–25], weld metal properties [26–28], complete joint assessment [29–34], and HAZ properties and structure which will be discussed later. Of interest to pipeline construction is how to reduce the costs of completing a girth weld. One such method is to replace the commonly used single torch GMAW welding with higher productivity weld processes, such as dual torch welding. With a high productivity weld process, more welds can be completed in the same amount of time and field labour costs can be reduced.

2.3 Dual Torch Welding

Dual torch welding is a high productivity welding process which has a second welding torch that trails the lead torch at a set distance. The result is that there is significantly more weld metal that can be deposited on a single pass of the welding equipment, which allows for increased welding productivity. Figure 2.2 schematically shows the difference between single torch and dual torch

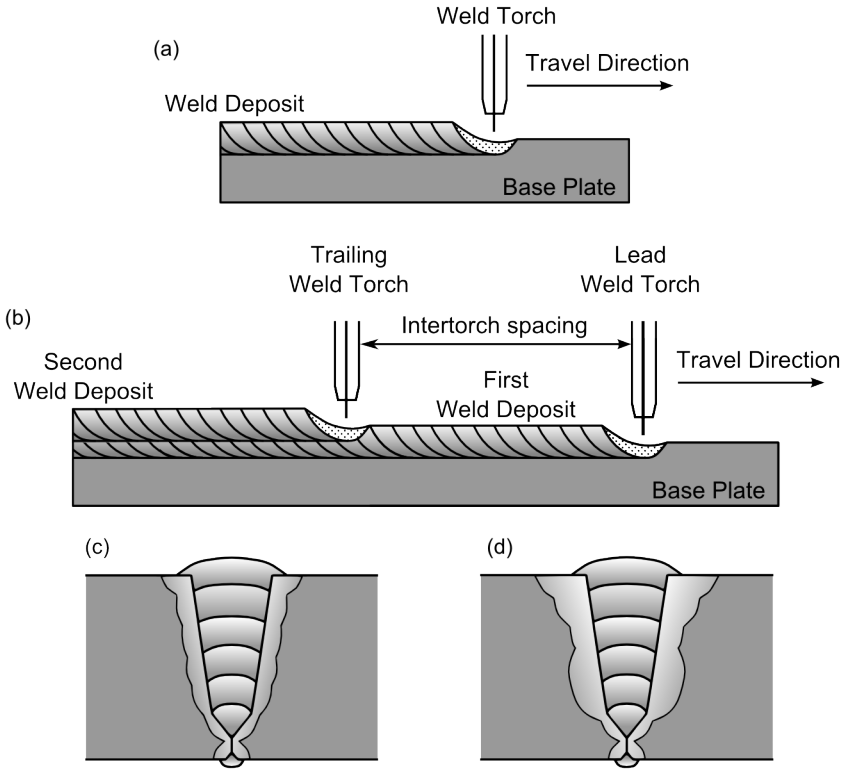

Figure 2.2: Schematics of (a) single torch welding, (b) dual torch welding, (c) the cross-section of a multipass single torch girth weld, (d) the cross-section of a multipass dual torch girth weld.

welds. For a dual torch weld, the parameters of each torch may vary in order to achieve desirable mechanical and fracture results of the final weld. One of these parameters that is being considered is shown in Figure 2.2 (b), which is the inter-torch spacing in a dual torch weld. It is of interest to consider how the heat from the lead torch influences the peak temperatures and cooling rates in the HAZ of the second torch. With decreasing inter-torch spacing, this influence would become greater, resulting in higher peak temperatures and slower cooling rates if measured from the same location in the HAZ. Figures 2.2 (c) and (d) showing schematic diagrams of the cross-section of the deposits from a typical pass schedule for single and dual torch pipeline girth welds and the expected HAZ that would result from it. Specifically, note the wider HAZ expected in the dual torch weld.

While there is significant research into development of dual torch procedures, there is relatively little on the effects of this procedure on the HAZ. The most substantial work can be found in the

doctoral thesis by Hudson [35]. In this work dual torch and dual torch tandem weld procedures are used to produce joints on X100 strength steel. Tandem welding is a high productivity weld procedure where two wires feed a single welding torch. In Hudson's work he showed that for the welding speed and heat input applied that a 100 mm torch spacing meets the desired properties. He also showed that a 50 mm torch spacing produces a lower toughness in the HAZ than is desired. Hamad et al. [36] investigated dual torch girth welds for X80 with a 50 mm torch spacing. Their work also showed a decrease in toughness in comparison to single torch weld that was related to the HAZ. Gianetto et al. [26] and Hamada et al. [28] investigated the properties of the weld metal for dual torch processes. These studies revealed some interesting aspects of dual torch welds, but lack comprehensive link between dual torch procedures, microstructure development, and mechanical properties.

2.4 Welding Temperature Measurements

The microstructure evolution in the HAZ is determined by the time-temperature profile, the so-called thermal cycle, that it is exposed to. The thermal cycle varies with weld procedure, weld parameters, and position. For a single torch pass the thermal cycle at a point will rapidly reach a peak temperature and cool from there. In the case of a single pass of a dual torch weld, two peaks are reached. Figure 2.3 is a schematic showing thermal cycles of a single torch and a dual torch pass. In industry practice the time to cool between 800 °C and 500 °C (t_{8-5}) is used to characterize if a thermal cycle will potentially result in detrimental microstructures in steel. In the dual torch pass thermal cycle, an individual torch should give a similar thermal cycle to that of a single torch. However, the thermal cycle of the second or trailing torch of a dual torch pass may be affected by the initial or leading torch, potential slowing the cooling rate which would increase the t_{8-5}. While there is much research into predicting the thermal cycles in the HAZ of a single torch pass, such as the most commonly used analytical solutions of Rosenthal [37], there has been little work to predict thermal cycles in a dual torch pass. The work by Chen et al. [38] investigated a dual torch thermal cycle using FEM models but provides no predictive tools to expand to other procedures.

With no established predictive tool to estimate dual torch thermal cycles for a given procedure, direct temperature measurements provide a solution. For thick plate welds, like those in a pipeline, embedded thermocouples are necessary for these direct measurements. Embedded ther-

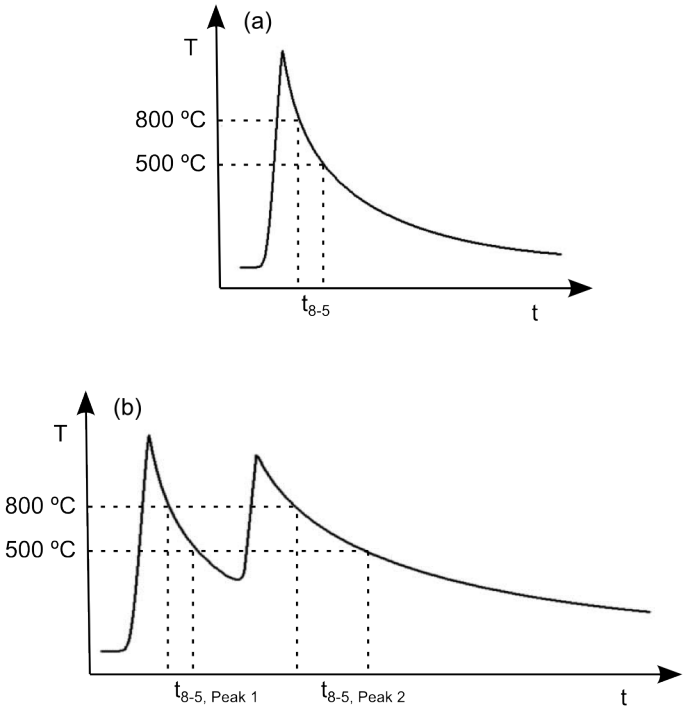

Figure 2.3: Time-temperature schematics of a point in the HAZ of (a) a single torch weld, (b) a dual torch weld.

mocouples for measuring weld thermal cycles have a number of potential issues. Ensuring good contact between the thermocouple junction and the end of the hole is difficult. Welding processes also introduce a large amount of electrical noise. The presence of a hole can influence the heat flow and may introduce error into the measurements. In spite of the difficulties, direct temperature measurements have been used to validate weld heat flow models in single torch thick plate welds. The work of Hudson [35] used direct temperature measurements to determine thermal cycles in X100 GMAW girth welds, including some dual torch procedures. His measurements involved both plunging thermocouples into the molten weld pool and embedding the thermocouples under the weld via drilled holes. In the investigation of Nuruddin [39], embedded thermocouples were used to investigate both tandem metal inert gas welds and submerged arc welds of X65, X70 and X100 linepipe steels. Bilat et al. [40] measured thermal cycles of a dual torch GMAW girth weld using embedded thermocouples. With this thermal cycle data they fit a model to the observed thermal cycles and used this to guide laboratory thermal simulations. Poorhaydari-Anaraki [41] drilled holes in X100 plate and embedded thermalcouples to measure thermal cycles from gas tungsten welds in a bead-on-plate procedure. Kou and Le [42] embedded thermocouples in the bottom of a 6061-T6

aluminum plate to validate their heat flow mode. There are numerous other works that have also used embedded thermocouples in thick plates in order to determine HAZ thermal cycles [43–46]. While each technique varies slightly in terms of hole design, how it makes a junction with the plate, the material used, and so forth, it is seen that direct temperature measurements through embedded thermocouples can be used to determine thermal cycles in the HAZ.

2.5 Heat Affected Zone in Steel

The heat affected zone (HAZ) is the region of material adjacent to a weld where metallurgical changes have occurred. The thermal cycle and specific steel chemistry will determine the extent of the HAZ and the microstructural evolution within the HAZ. Reference books by Grong [37] and Easterling [47] provide excellent reviews of microstructural development in the HAZ. For a single pass of a welding torch with a steel base plate the HAZ is typically categorized into four regions. From closest to furthest from the fusion line, these regions are the coarse grain HAZ (CGHAZ), fine grain HAZ (FGHAZ), intercritical HAZ (ICHAZ), and subcritical HAZ (SCHAZ). Comparison of peak temperature reached to the iron-carbon phase diagram, as shown in Figure 2.4 can help ratio-

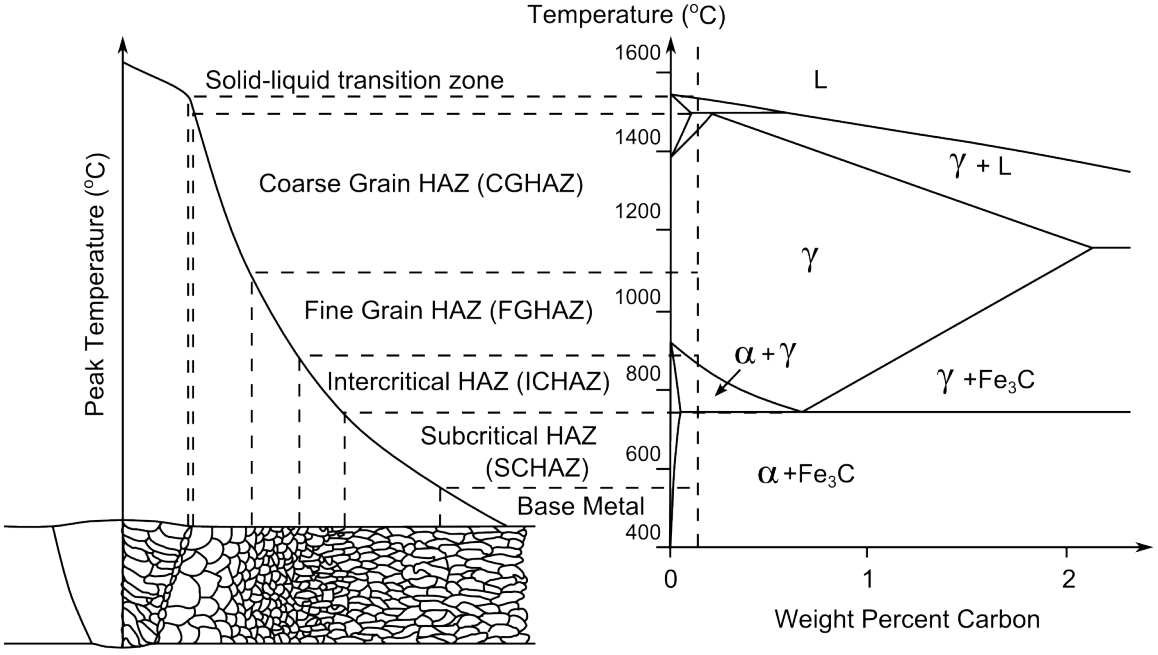

Figure 2.4: Schematic showing the relation between HAZ position, peak temperature, HAZ region, and Fe-C phase diagram for a single torch weld, after [47]

nalize the HAZ categories. It should be noted that welding is a non-equilibrium practice. Thus, non-equilibrium values, such as austenite formation start and finish temperatures (A_{c1} and A_{C3} respectively), should be used instead of the equilibrium phase diagram. In the diagram it can be seen that the final observation of the CGHAZ is related to high peak temperature of the weld pass causing significant grain growth in the austenite grain size prior to cooling and forming the final transformation products. The FGHAZ is seen to be related to when the steel is fully austenitized but has not seen significant grain growth in the prior austenite grains before cooling and forming the final transformation products. The ICHAZ represents a portion of the microstructure where peak temperatures have not allowed for the microstructure to become fully austenitized. The SCHAZ is a region that has not be austenitized at all, but has perhaps had coarsening of carbides or other tempering effects on the microstructure at the elevated temperature.

In a multipass or dual torch weld there are some additional complexities as HAZ regions from each pass or torch may interact in such a way so as to create potentially different microstructures. Figure 2.5 shows a schematic of a multipass weld microstructure related to the peak temperatures reached. While there may be only slight differences in microstructure of most of these multipass regions compared to single torch, the intercritically reheated coarse grain HAZ (ICCGHAZ) has potential to be a drastically different microstructure. As a result the ICCGHAZ as well as the CGHAZ has been the focus of a significant amount of research, particularly with regards to strength and toughness, which will be discussed later.

The classification of HAZ regions gives a broad understanding of what is occurring in the HAZ. A more detailed understanding of the HAZ comes with knowledge of how the thermal cycle and steel chemistry lead to austenite decomposition products. In a given region of the HAZ for pipeline steels, the final microstructure typically consists of a complex microstructure of at least two of the following decomposition products, which are listed in order of decreasing transformation temperature: polygonal ferrite, Widmanstätten ferrite, acicular ferrite, upper bainite, lower bainite, martensite.

As martensitic structures typically have a portion of retained austenite which is extremely difficult to distinguish from the martensite phase, and thus are often referred to as the martensite-austenite (MA) phase. In general, characterization of the amounts of each structure in the HAZ is difficult due to the presence of multiple microstructures that are difficult to differentiate based

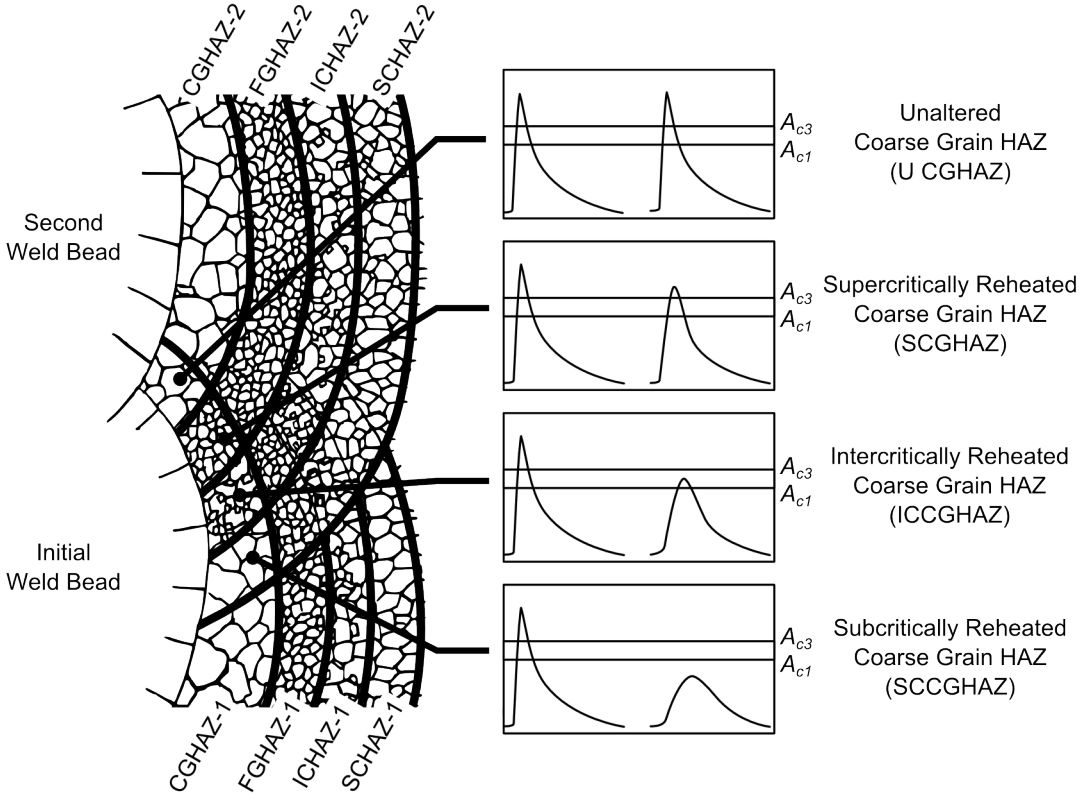

Figure 2.5: Schematic showing the interaction between initial and following torches on the HAZ regions in a multipass weld, after [48].

on optical observations particularly in finer morphologies of the microstructures. Further difficulty in characterization of microstructures in the HAZ is that there is significant changes in the microstructures over very short distances in the HAZ. In literature it is seen that there is often also different terminology used to describe microstructures [49–52] which emphasizes the uncertainty in microstructure classification. Often, laboratory thermal simulations are used to isolate the thermal cycle at a specific point within a HAZ and use a combination of metallography and dilatometry techniques to characterize the microstructure.

The use of thermal simulations also allows for the construction of a continuous cooling transformation (CCT) diagram for a given composition, which can be used to predict the final microstructures along an HAZ cooling path [37, 47, 53]. However, caution must be used in the strict usage of CCT diagrams. In the work by Spanos et. al. [54] and the study by Shome and Mohanty [55], CCT diagrams for HSLA-80 and HSLA-100 grades of steel differ between the CGHAZ and FGHAZ. This difference is attributed to the differences in prior austenite grain size and the dissolution of

precipitates resulting in alloying elements being put into solid solution.

Austenite grain size is important to the transformation to final microstructures in the HAZ. It has been noted that the larger grain sizes typical of the CGHAZ promote bainitic and martensitic transformation products [56]. The prior austenite grain size in the HAZ is affected by a number of factors. For HSLA steels there are typically pinning precipitates that are used to limit grain growth during reheating and hot rolling during production, and in the HAZ during welding. These precipitates can coarsen or dissolve at higher peak temperatures in the HAZ, lessening the Zener pinning force and allowing the austenite grains to grow to sizes consistent with the CGHAZ. One such set of precipitates in niobium-bearing steels are niobium-carbonitride (Nb(C,N)) complex precipitates. These precipitates have been noted to dissolve at temperatures in the range of 1000 - 1300 °C [56–58]. Titanium-nitride (TiN) precipitates have shown to be much more stable than Nb(C,N), however these can coarsen at high temperatures (above 1300 °C) [59]. Moon et. al. [60] showed that Nb and Ti can also form complex (Ti,Nb)(C,N) precipitates and that these can result in larger austenite grain sizes than just TiN precipitates alone.

The effect of the thermal cycle is extremely important in determining the final microstructure in the HAZ. This is primarily through the effect of cooling rate during the austenite decomposition but as well through the temperature effect on austenite grain size and state of precipitates. Figure 2.6 shows schematically how all of these effects interact on a CCT diagram to promote or slow certain transformations in the HAZ.

In multipass welds the final microstructure can prove to be even more complex. This is most true of the ICCGHAZ as the formation of austenite upon reheating will contain both the microstructure of the first pass that produced CGHAZ and new decomposition products from the second pass. In investigations by Lee et al. [61], Davis and King [62], Li et al. [63] and Bonnevie et al [64] it is seen that the ICCGHAZ typically has higher amounts of MA and a higher number of large or massive MA compared to CGHAZ. Later passes in a multipass weld were shown to reduce the amount of MA in the ICCGHAZ by Bayraktar and Kaplan [65].

There is an extensive number of HAZ studies across all types of steel chemistries and welding conditions, most of which are not relevant (i.e. very different chemistry and welding conditions) to this study. The studies with relevant cooling rates in the HAZ and steel chemistries are those of Hamad et al. [36], Gianetto et al. [66], Fairchild et al. [67], and Moeinifar et al. [68]. Table 2.1

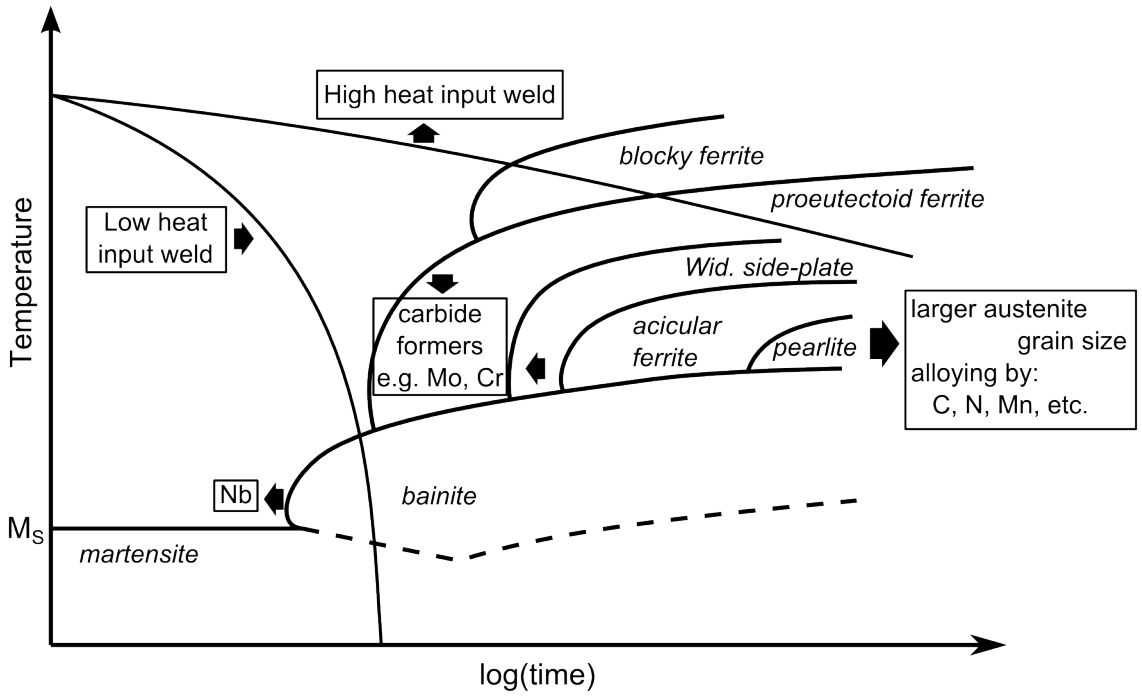

Figure 2.6: Schematic of a continuous cooling transformation diagram showing how various factors influence the final microstructure, after [47].

Table 2.1: Steel chemistries (wt %)

	C	N	Mn	Si	Ni	Mo	Cr	Ti	Nb	V	S	P	Cu
Hamad et al. [36]	0.06	<60ppm	1.6	-	N/A*	0.2	N/A*	N/A*	N/A*	-	-	-	N/A*
Gianetto et al. [66]	0.1	<0.0025	1.5	0.18	0.68	<0.03	0.02	0.006	0.027	-	0.004	0.01	0.18
Fairchild et al. - A [67]	0.11	0.0041	1.53	0.23	0.12	0.011	0.012	0.011	0.028	0.076	0.001	0.011	0.26
Fairchild et al. - B [67]	0.094	0.0049	1.4	0.31	0.014	0.011	0.011	0.048	<0.001	0.005	<0.001	0.008	0.011
Moeinifar et al. [68]	0.072	0.004	1.805	0.25	0.26	0.29	0.02	0.012	0.035	0.003	0.001	0.008	0.009

reports the steel chemistries of the steels and a review of the cooling conditions and observed microstructures follows.

The work by Hamad et al. [36] is relevant to the current study as it was done at an industry sponsor using similar chemistry and weld procedures. In their work, the single torch and both torches of a dual torch weld on a X80 pipeline steel used a low heat input of approximately 0.5 kJ/mm. While there is limited measured thermal data provided, it is seen that the second torch gives an average cooling rate of 30 °C/s (t_{8-5} of 10 seconds). In their observation it is seen that the dual torch HAZ microstructures showed significantly larger prior austenite grain sizes compared to the single torch samples. The dual torch microstructure also shows to be largely upper bainitic while

the single torch microstructure is lower bainite and lath martensite.

Gianetto et al. [66] investigated microstructures that developed in the CGHAZ and ICCGHAZ from submerged arc welds with two heat inputs. The two heat inputs investigated lead to estimated average cooling rates of 41 °C/s (t_{8-5} of 7.3 seconds) and 21 °C/s (t_{8-5} of 14.5 seconds). CGHAZ microstructures in both cases gave a bainitic microstructure with some isolated intragranular ferrite regions. With the higher heat inputs a larger prior austenite grain size was seen. In revealing the ICCGHAZ it was seen that carbides were seen at prior austenite grain boundaries with some smaller amounts transformed in the grain interior. The carbides in the ICCGHAZ were observed to increase in size with temperature in the ICCGHAZ.

In the study by Fairchild et al. [67] the CGHAZ was investigated for different alloys. At an average cooling rate of 48 °C/s (t_{8-5} of 6.2 seconds) the microstructure observed in both alloys was seen to be primarily bainite with an amount of lath martensite. With a slower average cooling rate of 8.8 °C/s (t_{8-5} of 34 seconds) the microstructure was seen to still be primarily bainite but with no martensite. At an average cooling rate of 5.6 °C/s (t_{8-5} of 54 seconds) both alloys showed to be a mixture of different types of ferrites and upper bainite.

The CGHAZ and reheated CGHAZ was investigated by Moeinifar et al. [68]. The cooling rate of 3.75 °C/s (t_{8-5} of 80 seconds) resulted in blocky MA as well as MA forming in stringer-like patterns in the CGHAZ. In the ICCGHAZ it was seen that the blocky MA at prior austenite grain boundaries had coarsened. CGHAZ that was reheated just into the fully austenitic region showed MA content as well, but were less blocky and did not form the thick network at prior austenite grain boundaries as in the ICCGHAZ. For CGHAZ that was reheated below the austenite transformation start temperature a similar observation is made.

2.6 Fracture Testing

The emphasis on preventing failure in pipelines has resulted in the usage of a wide range of tests to asses the fracture properties of linepipe steels, their welds and their HAZs. The Charpy V notch (CVN) [69] test is the most common toughness assessment method used, but other common tests include the compact tension (C(T)) [70], single edge bend (SE(B)) [70], and drop-weight tear test (DWTT) [71]. A brief review of the toughness parameters obtained from the CVN, C(T) and SE(B) tests are presented below. A description of the DWTT will not be considered in detail, in spite

of the technique being continually used and improved for pipeline fracture testing as its sample dimensions are not favourable for HAZ testing or simulated HAZ testing [72–76].

The CVN is an impact test where the energy absorption of breaking the sample, measured by energy loss of the hammer, is used to quantify toughness. For ferritic steels, tests are done over a range of temperatures; as the temperature decreases, the fracture mechanism may change and the ductile-to-brittle transition temperature (DBTT) can be observed with higher DBTT representing lower toughness qualities [77]. The difference of the ductile and brittle fracture mechanisms will be discussed in a later section. The DBTT can occur over a range of temperatures and is often associated with significant scatter in absorbed energy values. Alternatively, this transition temperature can be determined by the observation of shear area on the fracture surface. In the ductile region, the energy to failure is called the upper shelf energy and is also used as a measure of toughness. Instrumented CVN tests provide load-time data, which is used to determine energy related to crack initiation (E_I) and crack propagation (E_P) where the peak load reached separates the portion of the load-time data relating E_I and E_P [77]. Less commonly, precracked CVN tests can be used to determine the dynamic critical stress intensity factor (K_{Id}) using a relation that require measurements of the critical stress intensity factor (K_{IC}) from statically loaded tests [77].

The C(T) test is the most common test to determine K_{IC} values and involves static loading of the sample in tension. With the load being applied by two pins ahead of the notch and precrack this creates a bending stress state on the remaining ligament with the root of the crack being placed under tension. Similarly, SE(B) tests are three-point bending tests loaded statically with a notch and precrack oriented on the side of the specimen that will be in tension. Using two of either the load, crack mouth opening displacement (CMOD) or crack length measurements the K_{IC} value can be calculated [70]. The critical J-integral (J_{IC}) can be determined using C(T) tests, but requires a large sample set or a more difficult procedure with careful measurement of crack extensions [77]. Crack tip opening displacement (CTOD) measurements can be made; these characterize toughness when they reach a critical value (δ_c) [78]. The critical crack tip opening angle ($CTOA_{cr}$) has been applied in the ductile fracture of pipelines and it has recently been shown that this value can be obtained using load-displacement data from thin-sheet C(T) samples [79]. The review by Zhu and Joyce [80] provides a review of these typical testing methods to obtain these fracture parameters, and on the relationship between these values.

The advantages of the CVN tests are that they are easy to perform, requires a relatively small amount of material, and minimal preparation. The drawback is that they provide only a relative measure of toughness from a dynamic loading situation. Conversely the advantage of C(T) and SE(B) testing is that it provides toughness values that are more robust and transferable to the final component. Unfortunately, regular C(T) and SE(B) tests require significantly more amounts of material, and are more difficult to prepare specimens due to having to create a fatigue precrack. There is opportunity for a fracture toughness measurement technique that can provide more information than a CVN test, but does not require extensive preparation as C(T) or SE(B) tests.

2.7 Kahn Tear Tests

The Kahn tear test utilizes notched sheet samples which are then pulled in tension along the same axis as the initial root of the notch to initiate then propagate a crack through the sample. The specimen is similar to that of a C(T) test in that a tensile load is applied off of the center of the sample. However the differences are that for the Kahn test the initial notch length to uncracked ligament is lower, load is applied in alignment with the root of the machined notch to start and that the notch is made with a constant angle from the edge to the root of the notch. The original sample design by Kahn and Imbembo was used for investigation of a variety of steel chemistries with plates of thicknesses from 12.5 to 25 mm [81–83]. The test provides load-deflection data which gives the tear strength (σ_{tear}), unit propagation energy (UPE) and unit initiation energy (UIE) of a crack, given by:

$$\sigma_{tear} = \frac{4\,P_{max}}{b\,t} \tag{2.2}$$

$$\text{UIE} = \frac{\text{initiation energy}}{b\,t} \tag{2.3}$$

$$\text{UPE} = \frac{\text{propagation energy}}{b\,t} \tag{2.4}$$

where P_{max} is the maximum load, b is the width from notch root to back edge of the specimen,

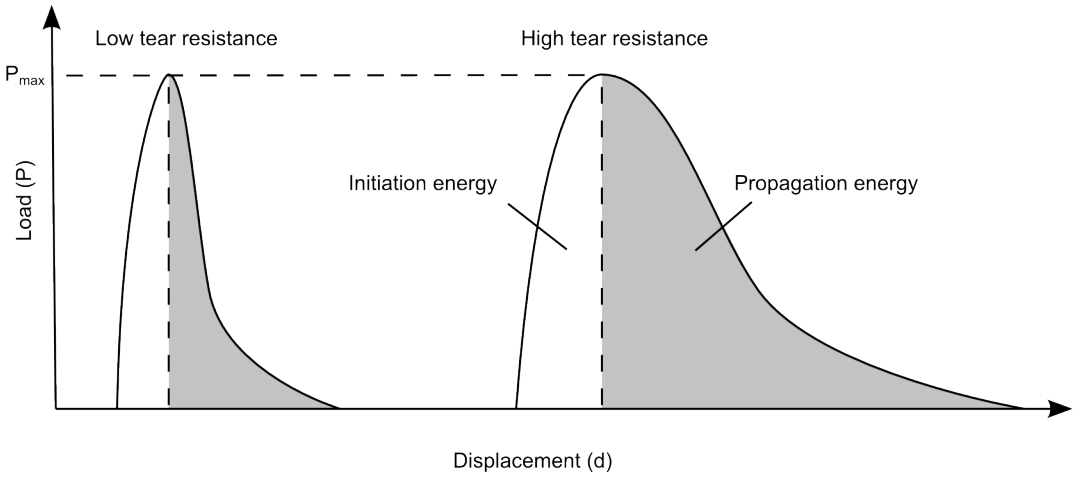

Figure 2.7: Schematic of representative Kahn tear test data showing low and high tear resistance results, after [84].

initiation and propagation energies are taken as the area under the load-deflection curve prior to and after maximum load respectively. Figure 2.7 shows how these values are defined.

The study by Kaufman and Knoll [84] reduced the dimensions of Kahn's original specimen in order to evaluate its potential to provide crack toughness data. Their study on aluminum alloys with thicknesses between 1.52 and 1.65 mm demonstrated a linear proportionality between UPE, and the sum of UPE and UIE from Kahn tests with the critical strain-energy release rate (G_c) determined from middle cracked toughness tests. The ratio of tear strength of the material to the yield stress was also shown to have a potential relation to G_c. The work by Kaufmann and Knoll constitutes the basis of the current ASTM standard [85] for the Kahn tear testing of aluminum products.

While studies such as those by Kirman [86], and Senz and Spuhler [87] utilize the same analysis as Kaufmann to characterize fracture behaviour between various aluminum alloys, the important works by Dumont, Deschamps et al. [88–90] on 7000 series aluminum alloys expands the analysis. Their first work [88] revealed the proportionality between the G_c from regular compact tension test and the UIE of the Kahn tear test. In their major subsequent work [89] they went on to use this data to formulate a model based on energy dissipation per unit area. The model accurately predicted UIE evolution with respect to yield stress of samples quenched slowly after different amounts of aging. However, the model had limited success in predicting the UIE evolution for the tougher samples observed when using fast quench rates after aging.

The work by Bron, Besson and Pineau [91] analyzed the Kahn test for aluminum alloys in a different way. They considered the crack energy dissipation rate (R) by correlating crack extension measurements to the load deflection data. They observed that the R value increases disproportionately more with yield strength for the middle cracked tension (M(T)) samples in comparison to the Kahn test. Their plausible explanation is that this is due to the plastic zone size increasing more with yield for the small scale yielding condition in the M(T) in comparison to the Kahn tests where the large scale yielding limits the plastic zone sizes. Fractography demonstrated that the failure mechanisms were identical for both the M(T) and Kahn samples which supports the notion of a relation between the two R values. Bron and Besson [92] subsequently modeled the M(T) and Kahn tests by applying continuum damage mechanics based on parameters determined from their earlier work. The model has some drawbacks, such as the large number of fitting parameters and shows a delay in crack initiation, but does provide fairly good accuracy in the prediction of load and crack growth rate. Asserin-Lebert, Besson and Gourgues [93] improved upon the measurement of R from Kahn test by limiting the crack extension measurements to the region of stable crack propagation for their investigation of specimen thickness on toughness in an aluminum 6056 alloy.

The study by Pirondi and Fersini [94] investigated the possibility of using crack tip opening angle (CTOA) measurements as a way to transfer between Kahn and M(T) test for aluminum alloys. They proved successful in applying a finite element model to achieve this relation when steady-state CTOA values from Kahn testing are compared to those of smaller sized M(T) tests. This is due to their similar evolution of crack propagation with respect to the ratio of applied force to plastic limit load. For regular sized M(T) tests, such as those used in the Bron et al. study [91], the relation is seen to simply work only after the fully plastic load is reached.

The modern Kahn tear test has been shown to be capable for determining fracture properties of aluminum alloys but has seen very limited application for testing steels. The work by Devgun, Carrillo and Roosen [95] has applied the modern Kahn tear test for their limited investigation of low carbon mild steels. Their analysis shows promising relationships between crack initiation and propagation energies and the yield strength, ultimate tensile strength and Charpy impact values. More recently, the work by Ying et al. [96] used Kahn tear tests in the investigation of tempering temperature effects on toughness in a high strength boron steel. Their analysis made use of the UPE and σ_{tear}, both of which showed a dependence on thickness in the range tested between 1 and 2 mm.

Their work did not investigate the Kahn tear testing technique with any significant detail. Lack of extensive investigations of the Kahn tear test on steels gives the prospect for novel studies.

2.8 Microstructure-Property Relationship

This microstructure-property relationship defines the variation in properties seen in the HAZ. The use of phenomenological models affirm our knowledge of the crucial factors in the microstructure-property relationship, while empirical models based on microstructural measurements also provides insight into these relationships in absence of a valid physical based model. Gladman [10] has discussed microstructure-property relationships and their modelling for HSLA steels. Of particular concern to the HAZ is toughness, which is related to the mechanical behaviour (i.e. strength and strain-hardening). Microstructure relations to the mechanical behaviour are discussed first, followed by their relations to ductile fracture, brittle fracture and the transition between ductile and brittle fracture. As linepipe steels may operate in sub-zero temperatures, considerations of a decreasing temperature on the microstructure-property relation will be emphasized.

2.8.1 Microstructure-Strength Relationships

Deformation in steel is defined by the resistance to plastic flow (i.e. the yield stress) and the evolution of this resistance with increasing strain, known as the strain hardening behaviour. The relation between microstructure and mechanical behaviour can be understood using an isolating mechanisms of strengthening, modeling these mechanisms, then combining the separate models to provide an overall strength of the microstructure. For a single phase material (e.g. ferrite), most of these models apply superposition of separate strengthening mechanisms taking the form of:

$$\sigma_{tot} = \sigma_0 + \sigma_{ss} + \sigma_{ppt} + \sigma_{dis} + \sigma_{gb} \tag{2.5}$$

where σ_{tot} is the strength of the phase, σ_0 is the inherent strength of the lattice to dislocation movement, σ_{ss} is solid solution strengthening, σ_{ppt} is precipitation strengthening, σ_{dis} is strengthening from dislocations (both those generated from phase transformation and from work hardening), and σ_{gb} is the grain boundary strengthening. Such an approach is used by numerous authors [10,97–102]

for steels.

The inherent strength of the lattice to dislocation movement, σ_0, can be qualitatively understood through the Peierls-Nabarro stress which is calculated according to [103]:

$$\tau_p = \frac{2G}{1-\nu} \cdot exp\left(\frac{-2\pi w}{b}\right) \tag{2.6}$$

where τ_p is the Peierls stress, G is the shear modulus of the material, ν Poisson's ratio, b is the magnitude of dislocation's Burger's vector (i.e. the unit slip distance), and w is the width of a dislocation. As the Peierls stress is a function of the width of the dislocation it is seen that FCC structures with large dislocation widths will typically have a smaller Peierls stress while BCC structures with small dislocation widths will result in high Peierls stresses. In the case of a high Peierls stress, as in steels, a strong temperature dependence is observed [77]. For BCC structures, the movement of dislocations occurs through the nucleation of a kink-pair, and then the motion of these kinks [103]. The formation of the double-kink pair has an activation energy and it is assumed that this gives rise to the temperature dependence of the intrinsic stress to move the dislocation. Unlike BCC metals, FCC metals have a weakly temperature-dependent Peierls stress.

Solid solution strengthening is broadly a complex interaction of chemical, electrical and geometrical effects of the solute atom, the parent lattice, and dislocation movement. However it can be generally stated that the solid solution strengthening effect is a consequence of the lattice dilation that the solute elements incur [10] and the elastic interaction of the solute atoms with the dislocations. It is typical to simplify the problem by assuming the strengthening due to solutes can be represented as the solute atoms acting as a set of weak obstacles on the glide plane. The strengthening contribution for solutes then can take the form of [10, 104]:

$$\sigma_{ss} = \sum k_i \cdot c_i^n \tag{2.7}$$

where c_i is the solute concentration of element i, k_i is its strengthening contribution, and n is a constant between 1/2 and 1. For a low concentration, n is approximately unity [10], otherwise it

can be taken to be 1/2 [105, 106] or 2/3 [107]. Since HSLA steels, such as X80, have low solute concentrations this empirical approximation is appropriate at room temperatures, though the values of the coefficient k_i will vary with the parent phase (e.g. ferrite vs. austenite). In BCC iron, interstitial elements (i.e. C and N) impose an asymmetric strain (i.e. both hydrostatic and shear components) which allows them to interact with both edge and screw dislocations making them the most potent solid strengtheners by weight. Substitutional solute atoms give rise to only hydrostatic distortions and will interact primarily with edge dislocations. By weight, it is seen that P is a strong strengthener (though the mechanism appears to be unrelated to lattice dilation for this element), while Si, Cu, and Mn are seen to be moderate solid solution strengtheners. Mo is seen to be to be a weak strengthener, while Ni is seen to have little or no solid solution strengthening effect. Cr actually shows a negative contribution to solid solution strengthening, though it is unclear if this is a result of it removing solute N from solid solution, or due to electron bond weakening of the lattice by its presence [10]. This highlights the need to differentiate between the alloy content levels and the portion of that content that is in solid solution or in precipitates.

Precipitates are present in HSLA steel and can cause strengthening through a number of possible mechanisms. In HSLA steels the primary particles of interests are carbides (e.g. Fe_3C, MoC, NbC) or nitrides (e.g. NbN, TiN), or complex carbonitrides (e.g. Nb(C,N), (Nb,Ti)(C,N)). The strengthening of these precipitates relate to how they interact with dislocations, which categorizes precipitates into those shearable and non-shearable by a dislocation. Also important is the size, spacing, and distribution of precipitates. The Orowan-Ashby equation considers only non-shearable precipitates, which is appropriate for hard carbides, nitrides and carbonitrides, and takes the form of [108]:

$$\sigma_{ppt} = \frac{0.538Gbf^{1/2}}{X} \cdot \ln\left(\frac{X}{6.125\times10^{-4}}\right) \tag{2.8}$$

where G is the shear modulus, b is magnitude of the Burgers vector, f is volume fraction of precipitates, and X is the diameter of precipitates. As the activation energy for a dislocation energy to bow or bypass is quite large, there is effectively little effect of temperature on precipitate strengthening [109].

The strength to move a dislocation increases with dislocation density according to the well known Taylor relation [110–113]:

$$\sigma_{dis} = \alpha M G b \rho_{dis}^{1/2} \tag{2.9}$$

where α is a constant dependent on temperature, M is the Taylor factor and ρ_{dis} is the dislocation density. Due to volumetric changes during austenite decomposition, certain phases have been observed to have high dislocation densities (e.g. martensite, acicular ferrite) prior to any extra plastic deformation of a sample. The generation, storage and annihilation of dislocations during plastic deformation leads to a change in the dislocation density giving rise to the strain-hardening behaviour observed in stress-strain curves. The evolution of dislocation density can be described by the model of Kocks and Mecking [114]:

$$\frac{d\rho_{dis}}{d\varepsilon_p} = k_1 \rho_{dis}^{1/2} - k_2 \rho_{dis} \tag{2.10}$$

where ε_p is plastic strain, k_1 is a constant related to dislocation storage, and k_2 is a constant related to the dynamic recovery of dislocations. While dislocation storage is not temperature dependent, dynamic recovery is via thermal activation aiding in the cross-slip of screw dislocations allowing for dislocations to meet and annihilate. As a result, with decreasing temperatures less dynamic recovery is expected which should increase the strain-hardening response (i.e. an increase in strength for a certain amount of plastic deformation for lower temperatures).

The well-known Hall-Petch relation is used extensively for determining strengthening due to grain size, given by [10, 113]:

$$\sigma_{gb} = k_{H-P}\, d^{-1/2} \tag{2.11}$$

where k_{H-P} is the Hall-Petch constant and d is the grain size. There have been a number of proposed theories to explain the Hall-Petch equation, however the physical basis for the relation remains un-

certain [113]. Nonetheless, the Hall-Petch equation adequately describes the grain size strengthening effect for more practical application. The Hall-Petch constant k_{H-P} has been observed to vary with alloy contents and with test temperature. Note that in the case of a complex microstructure d may be related to other specific features of the microstructure, such as the lath size in bainite.

As it is common to have more then one phase present in steel (e.g. MA is always present in at least some amount), there must be a consideration for determining the composite strength of the microstructure. One example comes from Bouquerel et al. [100] who determined the overall stress-strain behaviour of a transformation-induced plasticity steel by using stress mixture laws. Their approach was more detailed than most as they computed the strengthening for each of the polygonal ferrite, bainitic ferrite, retained austenite and strain-induced martensite phases using a method similar to equation 2.5 prior to invoking rule of mixtures. As the rule of mixtures is typically used to determine the composite strength of a steel, understanding the strengthening mechanisms within each phase provides insight into the overall microstructure-mechanical behaviour relationship.

2.8.2 Microstructure-Fracture Behaviour Relationships

Fracture occurs either through a process with extensive plastic deformation, referred to as ductile fracture, or with minimal plastic deformation, referred to as brittle fracture. In ductile fracture, a large amount of plasticity occurs prior to failure and requires relatively high amounts of energy. In brittle fracture, the amount of plasticity is limited and will require relatively low energy to fracture. While brittle fracture is absolutely undesirable, ductile failure in pipelines can lead to running cracks under certain conditions, and thus ductile fracture properties are also of concern [115]. It is important to understand how the microstructure affects toughness with respect to ductile fracture, brittle fracture and the transition from the ductile to brittle fracture.

Ductile fracture occurs via the nucleation, growth and coalescence of voids. The nucleation of these voids are associated with inclusions or second phase particles (e.g. precipitates, martensite islands) through particle cracking or interface decohesion [116]. As these voids grow, the volume fraction of voids is found to progress with a dependency on the initial volume fraction and shape of voids, which in turn are related to the fraction and shape of particles or hard phases acting as void nucleation sites [117]. At some point in the void growth process, mechanical stability in the remaining ligaments is lost resulting in voids coalescing and a ductile crack forming then

propagating from void to void [116]. The strain to final fracture has been observed to decrease with increasing volume fraction of particles or hard phases, and as the shape of these change from elongated in the tensile loaded direction to elongated in a direction normal to the tensile direction [116].

Brittle fracture in steels typically occurs through a cleavage mechanism. Cleavage, as described originally by Cottrell, occurs in a crystal through a separation along specific crystallographic planes when stress reaches a critical level [10]. The nucleation of a crack may be associated with stress intensification processes such as particle (e.g. carbonitrides) cracking, debonding between phases, or at dislocation pile-ups. At a critical stress, this initial crack will propagate across the grain. Depending on the temperature and the grain size, this cleavage crack across a grain may be arrested by a grain boundary until the applied stress along with the stress concentration at this crack tip is raised enough to cause cleavage in the next grain [118]. Consequently it is seen that the stress to cause cleavage fracture is inversely proportional to the grain size [77]. This is important as while other strengthening mechanisms do not also improve cleavage fracture resistance, microstructure refinement provides an improvement both to strength and cleavage fracture resistance.

Brittle fracture is of particular concern to the HAZ of pipeline steels. Measured DBTT from CVN tests are typically used to determine susceptibility to brittle fracture. This transition temperature has typically been characterized by empirical models, for example one used by Koo et al. [99] for high strength pipeline steels is given by:

$$DBTT = F(\sigma_0 + \sigma_{ss} + \sigma_{ppt} + \sigma_{dis}) - k_{CVN}\, d_{eff}^{-1/2} \tag{2.12}$$

where F and k_{CVN} are constants and d_{eff} is the facet size in cleavage, which is the grain size in a simple ferritic structure, or related to the size of low-angle boundary domains in complex structures containing bainite or martensite.

As the stress concentration of a crack causes the development of a plastic zone which influences the stress field, the stress-strain behaviour including strain-hardening is important to consider. Strain-hardening considerations have been applied previously, and are well reviewed in the book by Thomason [116]. It is seen that the strain-hardening behaviour is included through Hollomon-based

equations. To this author's knowledge, only the work of Spätig et al. [119] applied the Kocks-Mecking view of strain-hardening to an assessment of fracture. Their study on a ferritic-martensitic steel used Kocks-Mecking analysis in part to determine constitutive temperature behaviour of their steel. Subsequently, they used a 2D FEM model of a C(T) test in the plane strain condition in combination with the determined constitutive behaviour to estimate the stress-strain field ahead of the crack tip. They considered cleavage to occur when a critical tensile stress is reached over a critical area ahead of the crack tip. Comparison of the resulting effective critical stress intensity (K_{eff}) from the model with experimental data showed good predictions at temperatures below the DBTT. This highlights the practical use of investigating the relations between microstructure, mechanical behaviour, and fracture.

2.9 HAZ Mechanical Properties & Fracture Toughness

As mechanical and fracture properties are directly related to microstructure, and the HAZ is noted to be a gradient of microstructures, it can be expected that a gradient in properties will exist in the HAZ. Testing to determine properties in a HAZ subregion from an actual weld is not straightforward, as the microstructural gradient changes over a very small distance. Mechanical properties are most commonly investigated using hardness measurements, which provide only limited information [47]. While there are studies that have investigated other methods of testing, such as subsize or micro tensile testing [120–122], microshear testing [123], and shear punch testing [124], they are subject to potential errors by testing a gradient in microstructure across the HAZ and have not seen wide acceptance. Typically CVN and SE(B) tests are used to investigate real HAZ toughness properties. It has been discussed by many authors [36, 47, 125–127] that placing a fatigue crack or even a notch in the correct subregion of a real weld HAZ is extremely difficult. Measurements based on these techniques are clearly sensitive to sample preparation and may not properly isolate an individual subregion of the real HAZ. As such it is common to make use of laboratory thermal simulations to investigate the microstructures and mechanical properties of linepipe steels.

In the investigations of steel HAZ's, it has been noted that certain subregions are associated with significantly lower toughness. These areas of low toughness are most often associated with either the CGHAZ or ICCGHAZ [62–65, 68, 128–131], and it is seen in the majority of HAZ studies that the presence of MA is associated with low toughness [62–65, 131–137]. Some studies have found

other sources of low toughness, such as that by Fairchild et al. [67] which showed TiN particles initiated brittle fracture in the CGHAZ, or that by Ohya et al. [128] which found cracks in the CGHAZ and ICCGHAZ to initiate at the intersections of bainite packets (though often near large particles).

The work by Lee et al. [61] showed a decrease in the d_{cr} and CVN values for the actual CGHAZ compared to the base plate. Their study also showed decreased CVN energy values in the laboratory simulated CGHAZ and ICCGHAZ in comparison to all regions of the HAZ and they correlated the decrease in toughness values to the increase in volume fraction of MA constituent.

Shi and Han [132] investigated a 800 MPa HSLA steel using laboratory thermal simulations with a single peak temperature and cooling rates from 6 seconds to 240 seconds to generate CVN specimens. They found a decrease in toughness with increasing austenite grain size and MA content. While mentioned only briefly, they noted that as MA content increases the morphology changes from elongated to blocky in shape. They also found that peak temperatures in the ICHAZ produced a network of MA at grain boundaries and deteriorated the toughness severely.

The work by Davis and King [62] used CVN tests on laboratory simulated ICCGHAZ and showed that it is not simply the amount of MA, but also its distribution, morphology and hardness difference in comparison to the matrix phase which are important to brittle fracture initiation. The most detrimental situation is reported to be a near-connected grain boundary network of larger blocky shaped MA which is substantially harder than the matrix.

Li and Baker [136] investigated the effects of MA morphology on fracture toughness of ICCG-HAZ using laboratory thermally simulated CVN and CTOD tests. They found that both cracking and debonding of the MA phase occurred. Importantly, they found that in regions of high triaxial stress states that cracking of blocky MA phase is likely to occur whereas low triaxial stress states result in decohesion of the elongated stringer MA which leads to crack formation. They also found that carbides and inclusions did not significantly influence the toughness properties.

The thesis by Mohseni [138] investigated the DBTT in the CGHAZ, and ICCGHAZ of a X80 steel using SE(B) for CTOD measurements and CVN on laboratory simulated specimens. In his work, the ICCGHAZ showed lower fracture toughness values than the CGHAZ at each temperature tested. Close examination of the fracture surface revealed that MA was observed at the initiation points of cleavage cracks, and that these initiation sites were either due to MA debonding or from

a region between two closely-spaced blocky MA constituents with the ICCGHAZ showing more severe structures.

In the work by Goodall [139] laboratory thermal simulations were used extensively in the examination of HAZ transformation of X80 and X100 steels. In one part of his work, a X80 steel was subjected to two thermal cycles that simulate a dual torch weld where the torch spacing is so close that the second thermal cycle starts partway through the austenite decomposition of the first thermal cycle. The peak of the second thermal cycle for these tests did not reach full austenitization temperatures. That is, the heating of the second thermal cycle occurs between A_{r1} and A_{r3} of the first cycle and reaches a peak between A_{c1} and A_{c3} in the second thermal cycle. Thermal cycles were based on a Rykalin 3D models reaching an initial peak of 1350 °C giving an average cooling rate of 50 °C/s for the first peak and average cooling rate of 25 °C/s for the second peak. This was compared with samples simulating CGHAZ and ICCGHAZ with the same cooling profiles. From CVN testing in terms of the DBTT the CGHAZ gave the best toughness, ICCGHAZ gave lower toughness, and the interrupted ICCGHAZ gave the lowest toughness. The ICCGHAZ did show slightly greater upper shelf energy values compared to the interrupted ICCGHAZ samples. This difference was explained in terms of the lack of a hard MA phase along with acicular ferrite becoming a constituent in the interrupted ICCGHAZ giving rise to a slightly higher upper shelf energy for the ICCGHAZ, while the coarseness of the interrupted ICCGHAZ led to the higher DBTT.

The study by Hamad, Collins and Volkers [36] used relevant steel and welding conditions to this study. They tested the real CGHAZ of single, tandem and dual torch girth joints using CVN and CTOD from C(T) tests and showed δ_c and CVN values for upper shelf energy and DBTT were poorest for the dual torch process. The δ_c values were subject to scatter which they attributed to difficulties in crack placement or testing near the DBTT in the case of dual torch samples. They reported no significant variation from sample to sample in amounts of MA, segregation and large particles such as TiN which otherwise could explain the scatter. The study suggests that the larger prior austenite grain sizes helps shift the DBTT to higher temperatures, but does not provide a mechanism for why this occurs.

So far discussion has centered on toughness measurements of the HAZ. Mechanical property investigations of the various subregions of the HAZ are typically limited to hardness measurements. Recently only works by Zhao et al. [140] and Qiao et al. [141] used laboratory thermal simulations

to generate tensile specimens for investigation. The work of Zhao et al. [140] on a X90 steel provides engineering stress-strain curves for their specimens. Typical properties of yield stress, tensile strength and total elongation are plotted against the heat input used to calculate the thermal cycle, and a decrease in tensile strength with heat input is observed. Despite having full tensile test data on X100 thermally simulated samples, Qiao et al. [141] simply report tensile strength values compared to peak temperature for the different simulated process parameters. They show that a minimum of strength is observed at a peak temperature of 950 °C for each heat input case which is related to the FGHAZ. The lack of detailed investigation of the mechanical properties in the HAZ gives opportunity for novel work to be introduced.

CHAPTER 3

Scope and Objectives

3.1 Scope

This study investigates the mechanical behaviour of a X80 linepipe steel with microstructures produced that are relevant to a typical girth weld HAZ. The study uses a commercially produced pipe, specifically a Mackenzie Valley prototype strain based design X80 (650 MPa yield stress) steel. The welds of interest are GMAW produced girth welds with industrially relevant welding conditions (e.g. similar torch speed, heat input, number of passes). Furthermore, there is interest in comparing single torch welds to high productivity dual torch welds with different torch spacings. The mechanical properties of the HAZ microstructures that are of interest include the yield strength, work hardening behaviour, and tear resistance. These properties are to be investigated within the range of potential operating temperatures (20°C to -60°C).

3.2 Objectives

The objective of this work is to investigate the mechanical behaviour of microstructures that may be found in the HAZ adjacent to industrially produced GMAW girth welds. To achieve this objective, a number of related subobjectives were defined, summarized below.

- Characterize the time-temperature profile in the HAZ of typical girth welds for both single torch and for dual torch with different spacing.

- Develop the thermal cycle profiles for Gleeble heat treatments to reproduce relevant HAZ microstructures.
- Produce these microstructures in bulk specimens suitable for mechanical testing.
- Characterize the microstructure of the Gleeble heat treated specimens.
- Measure the tensile properties and tear resistance (using the Kahn tear test) of the thermally treated specimens at ambient temperature, -20 °C, and -60 °C.
- Characterize the fracture surfaces of both tensile and Kahn specimens
- Develop a model for the work hardening behaviour that relates to the characteristics of the microstructures observed and is applicable to all temperatures tested

In the achievement of these objectives, there is an impact to the current state of scientific and technical knowledge. Measurements of the HAZ thermal cycle profile, particularly with respect to dual torch welds represent a novel data set. The tensile and tear property measurements of specific microstructures found to be relevant to the HAZ furthers understanding. The development of a work hardening model represents an extension to the current state of work hardening models. On the technical side, HAZ temperature measurements as done in this study are a technical achievement in terms of their accuracy. The creation of bulk specimens suitable for testing required the refinement of Gleeble heat treatment techniques. This also produced a new set of data regarding tensile mechanical properties relevant to HAZ microstructures. The use of the Kahn tear test for HAZ steel specimens is a novel approach.

CHAPTER 4

Methodology

4.1 Material

The material used in this work is an X80 grade linepipe steel supplied by Evraz Inc NA. The chemical composition of this steel is given in Table 4.1. Using Nital and Le Pera etchings on this material, Tafteh [142] revealed the as-received microstructure of this steel, shown to be 97.5 % ferrite and 2.5 % martensite and/or retained austenite. In the work by Banerjee et al. [143] on this steel it was seen that there are three main types of precipitates in the as-received condition. There are large cuboidal TiN particles (with radii of approximately 61 nm) which remain stable through the high temperatures [143]. Nb(C,N) particles are seen in both large (approximately 69 nm) and small (approximately 2 nm) sizes [143]. Mo_2C particles are also observed with an average diameter of approximately 53 nm [143].

Table 4.1: Steel chemistry (wt %)

C	Mn	Nb	Mo	Ti	N
0.06	1.65	0.034	0.24	0.012	0.005

4.2 Metallography

To investigate the microstructures of this steel, samples were ground, polished, then etched. Wet grinding was performed progressively on 60, 180, 300, 420, 600, 800, and 1200 grit paper. Polishing

was then carried out using 5 μm then 1 μm diamond polish and then rinsed with distilled water and denatured ethyl alcohol. Two types of etching were carried out after the grinding and polishing, Nital and Le Pera. Nital etching uses a solution made of 2% by volume of concentrated nitric acid in absolute ethyl alcohol, with concentrated nitric acid being comprised of approximately 70% HNO_3 by weight in water. The sample was then immersed for approximately 30 seconds and then rinsed with distilled water and denatured ethyl alcohol. Le Pera etching involves two solutions that are mixed immediately before etching the sample. The first solution was a 4% weight/volume of Picric acid in absolute ethyl alcohol, and was left to stir slowly while polishing the sample. The second solution was a 1% weight/volume metabisulphite in distilled water, also made prior to polishing the sample. After the polishing and rinsing was complete, the sample was heated using a hair dryer while mixing and gently swirling 5mL of each of the two solutions together. The sample was then immersed for approximately 45 seconds. If the sample's microstructure was not fully revealed for both Nital or Le Pera etches, immediate reimmersion for short intervals was sometimes performed. If that proved unsuccessful the sample was ground, polished and re-etched starting from 800 grit paper.

Nital etching reveals the complex mixture of ferrite, upper bainite and lower bainite found in the microstructures of these steels. For this study, Figure 4.1 exemplifies how these constituents are classified. Irregular ferrite appears to have grains with irregular shape and no internal structure visible. Upper bainite shows packets of grains with an internal structure of aligned but disconnected particles or carbides. Lower bainite shows packets of grains with an aligned and very fine structure. In order to quantize the amounts of these constituents, a point counting technique was used. From a sample, multiple images (five at the minimum) taken at 500X magnification have a grid overlayed of them, and then the type of microstructures at the intersections are counted.

Le Pera etching reveals the martensite and retained austenite (MA) as bright islands against a darker matrix. The difference between martensite and retained austenite is not revealed using this technique. To measure the amount of MA, multiple images (again, five at the minimum) taken at 500X magnification are image-processed then measured. A brightness threshold was applied using the GNU Image Manipulation Program (GIMP) using the linear scale, which gives a black background with the MA phase that passes the threshold in white. The image was cropped to remove portions of the image that are darker in the outer regions due to vignetting. In the case

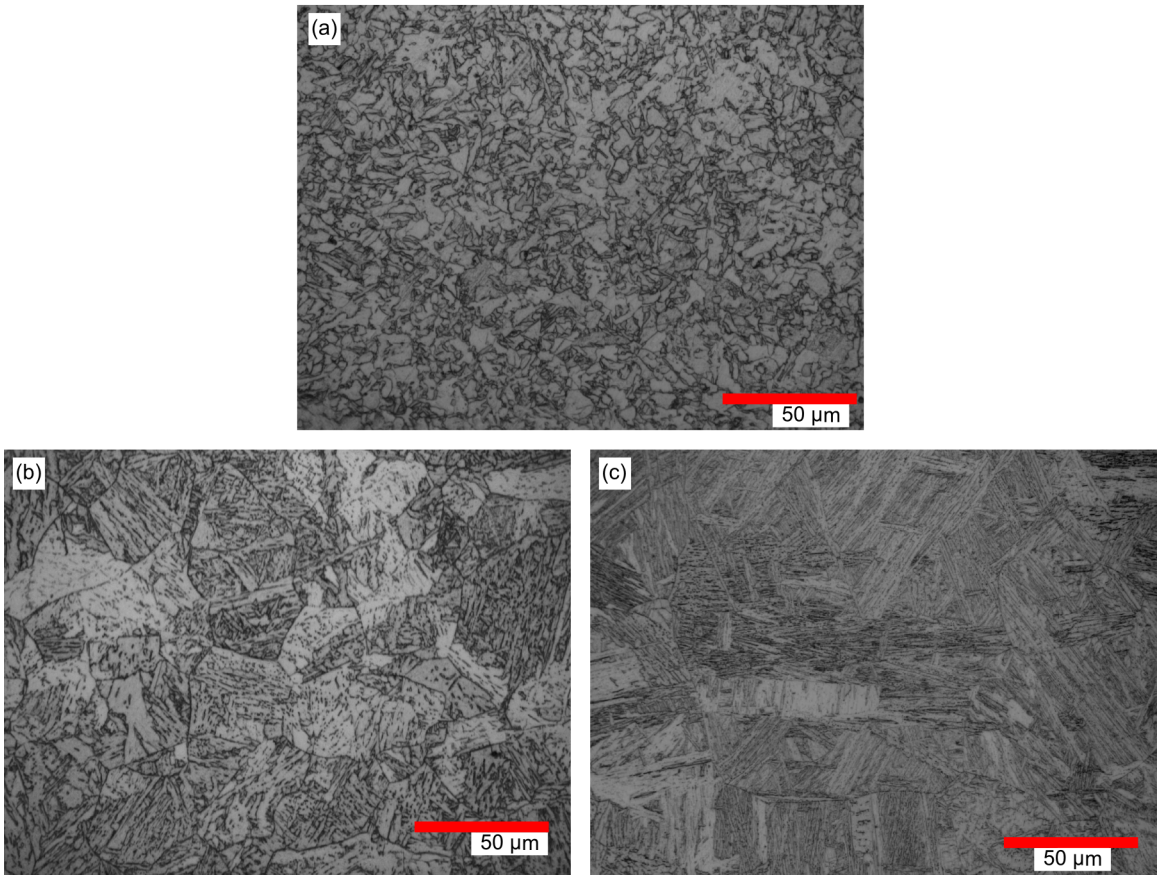

Figure 4.1: Classification of observed microstructures:(a) Irregular ferrite microstructure (b) Upper bainitic microstructure (c) Lower bainitic microstructure [144]

where it was difficult to identify a singular best threshold, two thresholding images are made to set the upper and lower bounds and analysis on both proceeds as follows and was then averaged at the end to determine a singular value. The thresholded image was loaded into ImageJ, set to 8-bit, then a threshold setting of (129,255) was applied, and then was converted to a mask. After this preprocessing, the ”Analyze Particles” command was used for particles with sizes from 0 to infinity and circularity from 0 to 1. This gives an area fraction of MA. The MA fraction was then subtracted from the fraction of the most appropriate phase as measured from the Nital quantization. Figure 4.2 shows the thresholding process and match up for a typical Le Pera image.

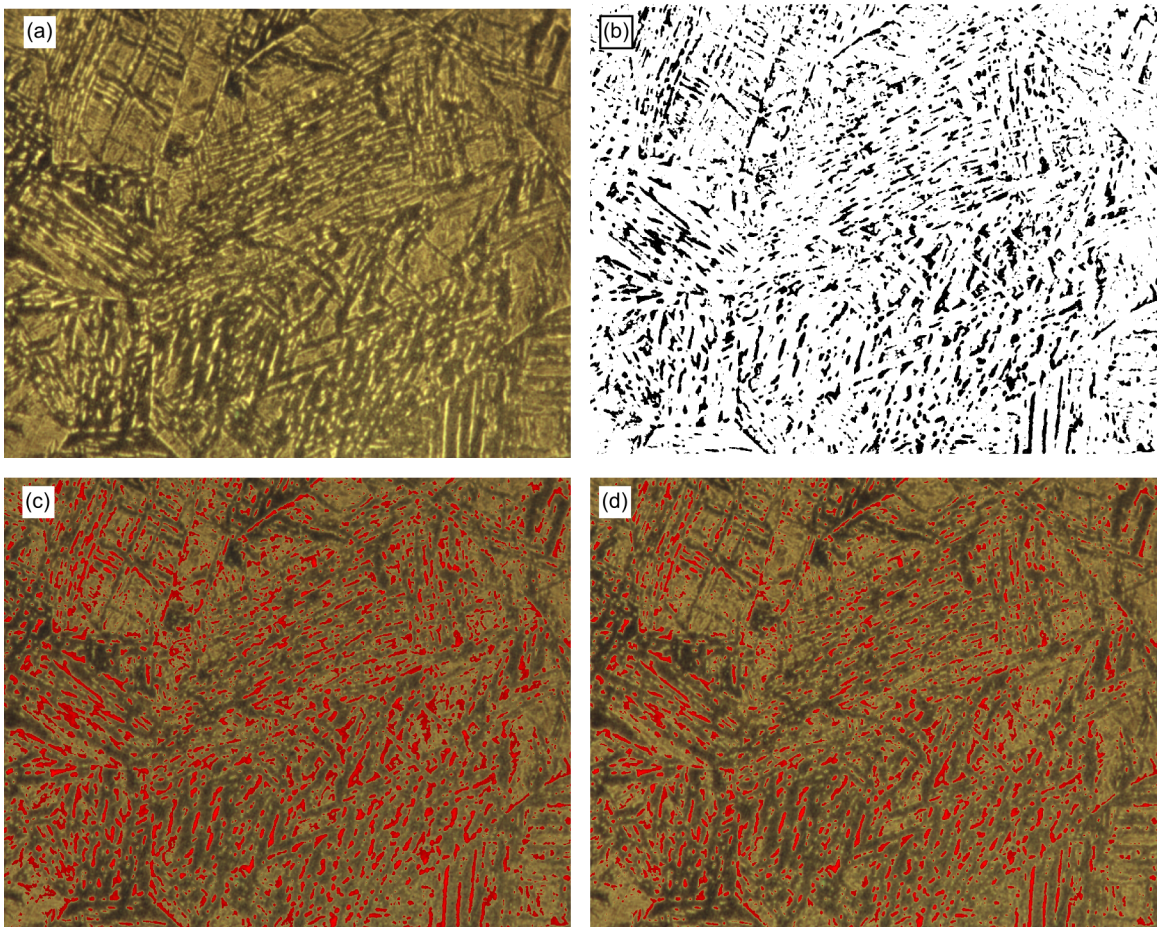

Figure 4.2: Le Pera thresholding method: (a) Initially cropped Le Pera image (b) Thresholded image display MA as black (c) Lower threshold overlayed as red on initial image gives MA content of 16.7% (d) Higher threshold overlayed as red on initial image gives MA content of 11.2%.

4.3 Weld Trials

Weld trials to measure the thermal cycles in the HAZ of a typical girth weld were performed with the assistance of Evraz Inc NA. Initially, Evraz supplied a cross-section of the a typical weld which was then Nital etched to reveal the HAZ and weld microstructure. This guided experimental design for the weld trial. The welds were done to join 16 mm thick flat plates of X80 steel with a length of approximately 610 mm along the welding line, and a width of approximately 305 mm. Six holes were drilled into the plates, spaced 50 mm from the end of the plate, 25 mm away from each other along the weld line, and at an angle close to the bevel so that the end of the hole was placed into the expected HAZ at different distances to the fusion line and at different depths. During the welding trial, type S for their high temperature measurement range, or N thermocouples for their high temperature stability but lower cost, were spot welded to the end of the drilled holes and were protected by a ceramic sheath. A schematic of the weld trial setup is shown in Figure 4.3, with details of the setup given in Table 4.2.

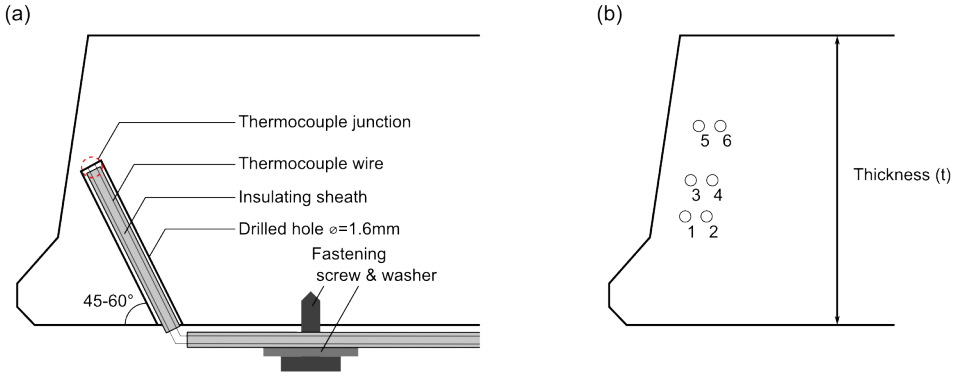

Figure 4.3: Schematics of (a) an embedded thermocouple in a plate ready for welding and (b) approximate placement and labelling of thermocouples.

Welding trials were performed at Evraz's Regina research and development facility using their robotic welding setup. Single torch welds as well as dual torch welds with inter-torch spacings of 2.75", 4", and 7" were performed to simulate the girth welding procedures for pipe as specified by TransCanada Pipelines Ltd. During the welding passes thermocouple data was recorded at a sampling rate of 244 Hz. As placement of the thermocouples were done to fit the wide range of HAZ

Table 4.2: Weld trial thermocouple placement

Weld Type	Thermocouple #	Relative depth from bottom	Distance from bevel (mm)	Thermocouple type
Single Torch	1	3/8	1.75	S
	2	3/8	2.25	N
	3	1/2	1.75	S
	4	1/2	2.25	N
	5	11/16	1.40	S
	6	11/16	1.90	N
Dual Torch	1	3/8	1.25	S
	2	3/8	1.75	N
	3	1/2	1.15	S
	4	1/2	1.65	N
	5	11/16	1.50	S
	6	11/16	2.00	N

for different torch spacings, and considering there is variation from test to test, multiple tests for each torch spacing was performed to improve chances of obtaining useful thermal cycle data. Welding procedures used in the trial, guided by those used in actual procedures by TransCanada Pipelines Ltd., follow the pass schedule schematically shown in Figure 4.4 and the details are reported in Table 4.3. Note the different heat inputs for the single and dual torch procedures.

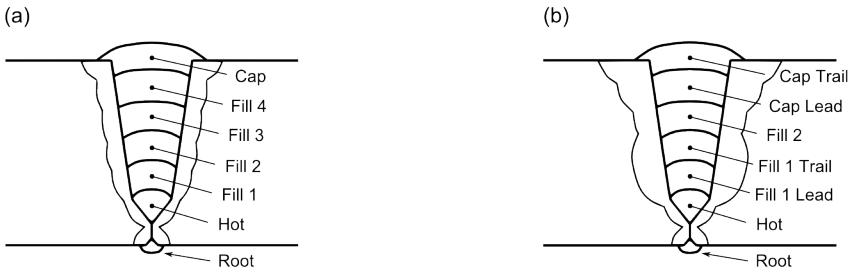

Figure 4.4: Weld pass definition for (a) single torch and (b) dual torch welds used in this study.

Table 4.3: Welding trial procedures

	Pass	Root	Hot	Fill 1	Fill 2	Fill 3	Fill 4	Cap
Single torch	Heat Input (kJ/mm)	0.23	0.15	0.26	0.26	0.26	0.26	0.26
	Travel Speed (mm/s)	12.5	23	17	17	17	17	17
	Preheat/Interpass (°C)	Room	-	100	100	100	100	100
	Pass	Root	Hot	Fill 1 lead	Fill 1 trail	Fill 3	Cap lead	Cap trail
Dual torch	Heat Input (kJ/mm)	0.2	0.17	0.57	0.57	0.56	0.36	0.36
	Travel Speed (mm/s)	12.5	23	8	8	7	8.5	8.5
	Preheat/Interpass (°C)	Room	-	100	-	100	100	-

Signal processing was conducted on the temperature-time data from the weld trials. First, a

Parks-McClellan filter was applied to remove noise from the raw signal, passing signals with frequencies under 12.2 Hz and completely attenuating noise with a frequency of 24.4 Hz and above (which represent 5% and 10% of the sampling frequency respectively). It was seen that there was a voltage shift of the measured data due to the activation of the welding equipment which was corrected for simply by addition of the shift to data for the duration of the welding equipment activation.

4.4 Gleeble Heat Treatments

Heat treatments were carried out using the Gleeble 3500 thermomechanical simulator at UBC. This allowed for the design of complex thermal cycles to create microstructures relevant to the HAZ. The design of the large strip testing sample used is shown in Figure 4.5. Samples were machined from the supplied X80 plate to a size of 200 mm X 50 mm X 1.20 mm with the length of the Gleeble specimen aligned in the rolling direction of the plate. Thermocouples were spot welded to the top surface to measure and control the temperature during the heat treatments. The center S-type thermocouple were to control the Gleeble's system to meet the programmed thermal cycles with the other, K-type thermocouples providing data on temperature gradients in the sample. The thermal cycles used are shown schematically in Figure 4.6. The experimental design was chosen to produce microstructures consisting of primarily one constituent relevant to the microstructures observed in the HAZ. This was accomplished by varying between two grain sizes of austenite prior to cooling, between the precipitate-solid solution conditions of Nb, and between two cooling rates.

The austenite grain sizes produced in the final thermal cycle were 5 μm and 42 μm as determined in the work of Tafteh [145] for the same thermal cycles. The conditions of Nb were to be primarily in solid solution or primarily in precipitates. In the case of Nb in solution, this required two thermal cycles, the first being to dissolve the Nb(C,N) particles and put Nb into the solution. In the case of a prior austenite grain size of 42 μm with Nb in precipitates, solutionizing was required in order to achieve the prior austenite grain size. For this condition, the final thermal cycle includes a 20 minute hold at an elevated temperature (900 °C) in the fully austenitic regime but below the Nb(C,N) formation temperature in order to precipitate an amount of Nb out of solution. While initially it was thought that this time would be enough to nearly fully precipitate, recent work by Reichert [144] has shown that this precipitation cycle results in approximately 50% of the Nb being precipitated.

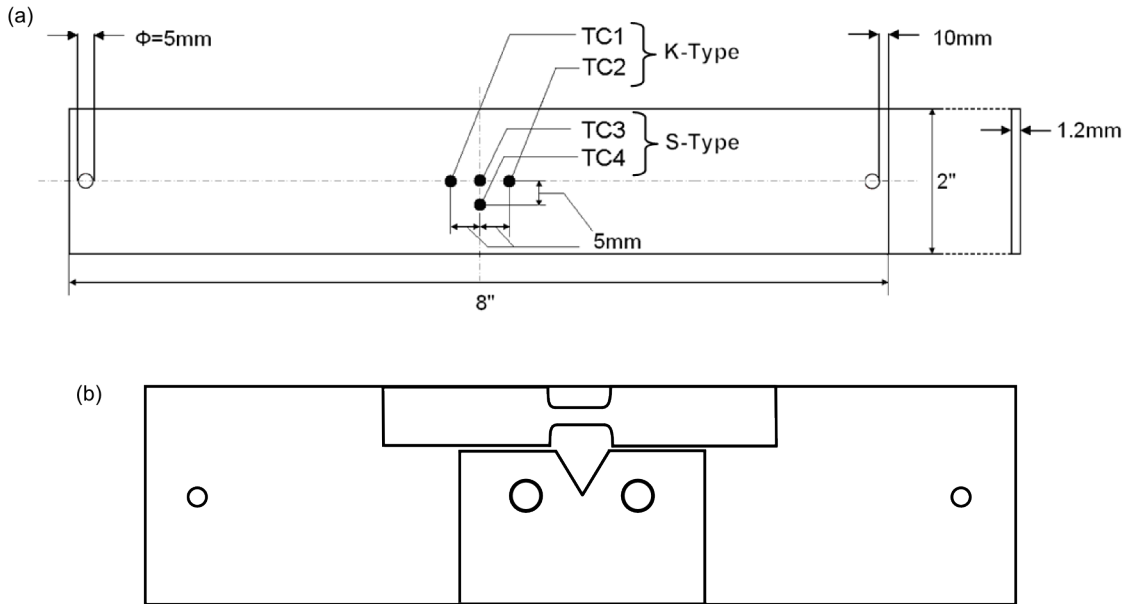

Figure 4.5: (a) Schematic of a Gleeble large strip design and (b) schematic of where mechanical testing specimens are removed from the strips.

While this condition will be referred to as Nb being in precipitates, it is important to keep in mind that the Nb will only partially be in precipitate form. The cooling rates selected were 10 °C/s and 50 °C/s. In order to cool the strip at these rates, the sample is quenched along the bottom of the sample using compressed helium set at a valve pressure of 12 psi and applied using a three-nozzle system. In order to prevent the strip from buckling during the testing, the Gleeble's air ram was set at 1.0kN in tension.

After Gleeble heat treatments, electrical discharge machining (EDM) was used to produce a tensile and Kahn specimen from the original sample as in Figure 4.5 (b). Samples for metallography (Nital and Le Pera etching) were taken from the material between the root of the Kahn notch and the middle of the tensile specimen.

4.5 Tensile Testing

Tensile tests were carried out on subsized specimens as shown in Figure 4.7. Ambient temperature tests were carried out using an Instron 8872 testing machine with an applied crosshead speed of 1.5 mm/min which gives an approximate strain rate of 2 x 10^{-3} s^{-1}. Testing at -20 °C and -60 °C were carried by immersing the samples in an ethanol-glycol mixture cooled to the point of freezing by dry ice. The exact mixture of ethanol-glycol for a given testing temperature was determined by

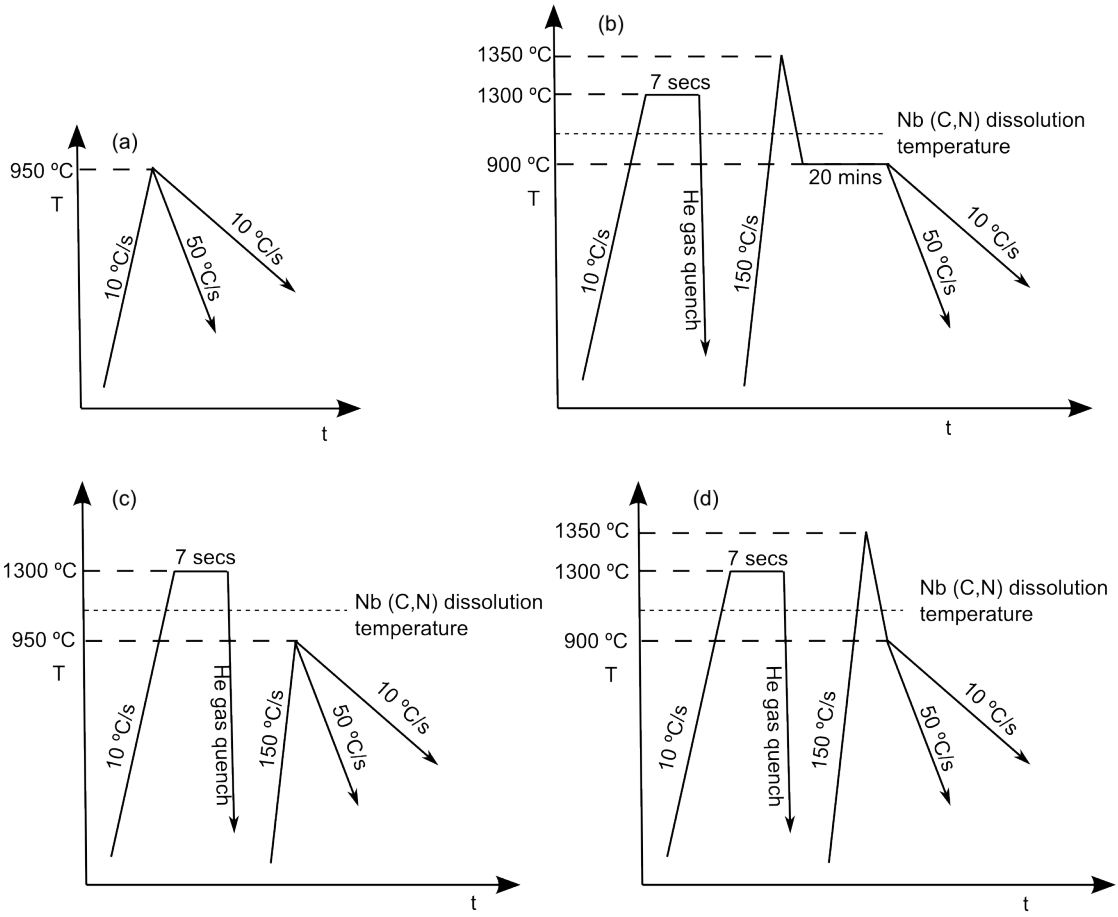

Figure 4.6: Thermal cycles for (a) Nb in precipitates with 5 μm austenite grain size, (b) Nb in precipitates with 42 μm austenite grain size, (c) Nb in solution with 5 μm austenite grain size, and (d) Nb in solution with 42 μm austenite grain size.

trial and error. The solution temperature was monitored throughout the testing process and found to be very stable, keeping within 2 °C of the aim temperature. Cold temperature tests were carried out on a Instron TM-L load frame with screw driven crosshead speed of 0.51 mm/min resulting in an approximate strain rate of 1 x 10^{-3} s^{-1}. An extensometer was used in all cases to measure the displacement in the gage of the specimen, including being immersed when needed.

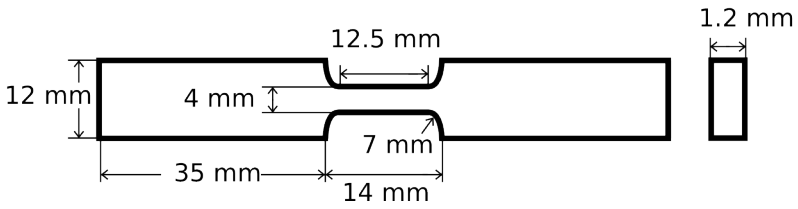

Figure 4.7: Schematic of the subsized tensile specimen.

In this study, the yield strength that will be used differs from the regular definition. Whereas the normally used definition of yield strength is based on the 0.2% offset method, this study will use the same offset method but with a 0.5% offset instead. As it will be shown, the initial portions of the stress-strain curves are very rounded. During the course of this investigation it was found that the 0.2% offset yield strength did not provide consistent measurements for these rounded stress-strain curves while the 0.5% offset yield strength did. The use of 0.5% yield strength results in a higher reported yield strength compared to the normal 0.2% and the reader should be aware of this when making comparisons of the yield strength in this study to those from other studies.

After testing, the fracture surface was examined using secondary electron imaging on a Hitachi S-2300 scanning electron microscope. From low magnifications images, an area measurement of the final fracture surface is made. This is used to determine the final fracture stress and the final fracture strain, computed from:

$$\sigma_{frac} = \frac{F_{frac}}{A_{frac}} \tag{4.1}$$

$$\varepsilon_{frac} = \ln \frac{A_0}{A_{frac}} \tag{4.2}$$

where σ_{frac} is the stress at fracture, F_{frac} is the load at fracture, A_{frac} is the fracture surface area, and A_0 is the initial cross-sectional area.

In the determination of fracture stress using this equation, the triaxial stress state in the neck is not taken into consideration. To do so requires a correction. To correct for the effect of triaxiality in the neck of these specimens at fracture, a finite element analysis of the tensile specimen was made by Puydt [146]. This model used the true stress-strain curve from the as-received condition. Using this data, he used the point of necking to the point of observed fracture to linearly extrapolate the true stress-strain data from the point of necking. The original stress-strain data with this extrapolation was used as an input for the model to be fit. The output of the model is a true stress-strain curve corrected for triaxiality. Note that this curve is the same up until the point of necking, then diverges

from this point. Figure 4.8 shows the true stress-strain curve from the input and the modeled true stress-strain curve in the neck. It is seen that the model true stress in the neck is higher than the input true stress, as expected. The difference between the model corrected true stress and the input true stress can be represented as a ratio. Figure 4.9 is the ratio of the computed true stress to the model true stress versus true strain. It can be seen in this figure that after a strain of about 0.9 a plateau of this ratio is reached at a value of 1.14. This factor, 1.14, then is used in the correction from the measured values of true fracture stress to account for the effect of triaxiality in the neck. An example of the effect of this correction of the fracture stress on the true stress-strain curve is shown in Figure 4.10.

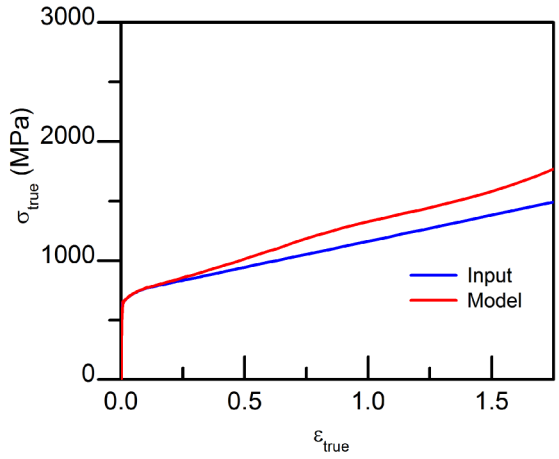

Figure 4.8: True stress-strain of model input based on the measured as-received condition compared to model output.

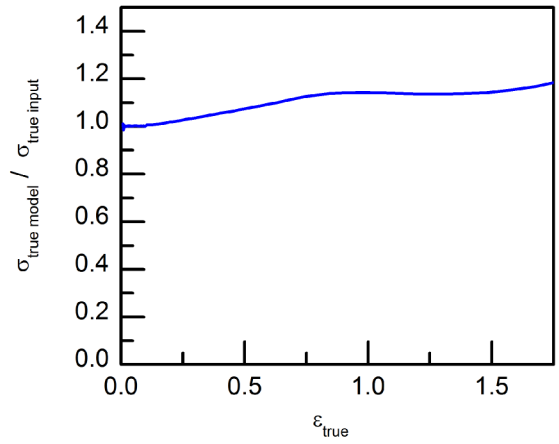

Figure 4.9: Ratio of model output to the input based on the measured as-received condition.

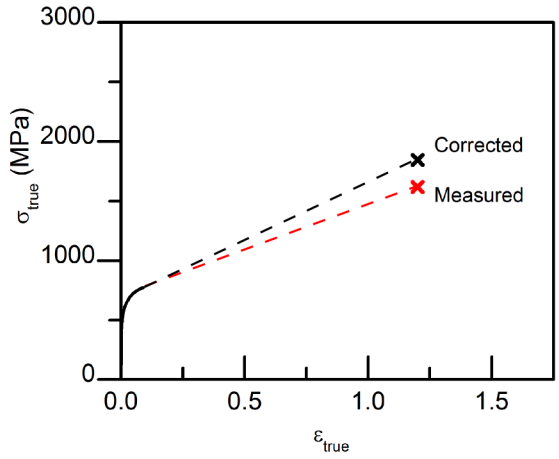

Figure 4.10: Example of resulting true stress-strain data without and with correction to the final fracture point.

4.6 Kahn Testing

To assess fracture properties, Kahn tests were used. The Kahn specimen, shown in Figure 4.11, was pulled in tension at a continuous rate of 0.4 mm/min which results in the initiation and propagation of a crack. Kahn tests were performed on a MTS 312.21 servohydraulic testing machine. Load line displacement was measured by attaching an extensometer to the pins passing through the specimen.

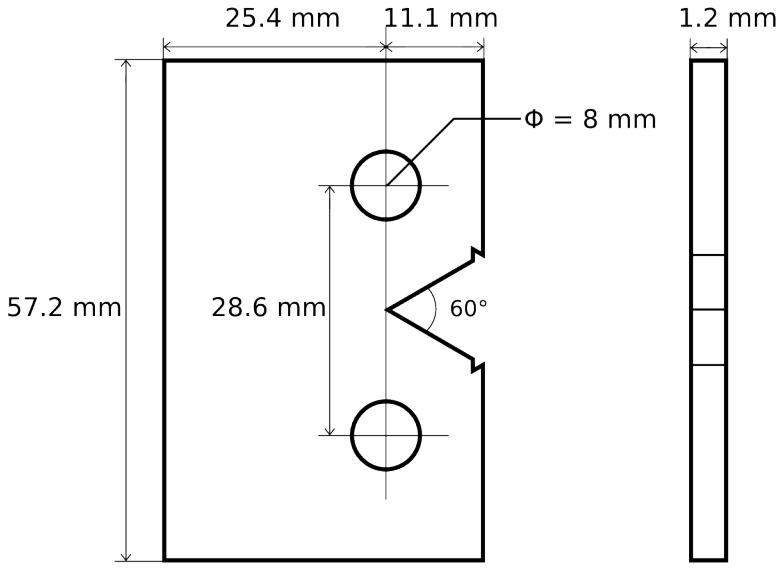

Figure 4.11: Schematic of the Kahn tear test specimen.

In order to investigate the effect of thickness on the properties measured, tests were carried out on the as-received material with additional thicknesses of 1.5 mm, 2.0 mm, and 2.5 mm. Low temperature testing were carried out using the same immersion solution of ethanol-glycol cooled by dry ice. As with the tensile tests, the fracture surface was examined using secondary electron imaging on a Hitachi S-2300 scanning electron microscope.

Analysis of the Kahn specimens uses the load-displacement data. A schematic of typical Kahn measurement data is shown in Figure 4.12. Tear strength (σ_{tear}) for this loading geometry is calculated according to the equation:

$$\sigma_{tear} = \frac{4\,P_{max}}{B_0\,t} \tag{4.3}$$

where P_{max} is the maximum load, B_0 is the uncracked ligament length, and t is the specimen thickness.

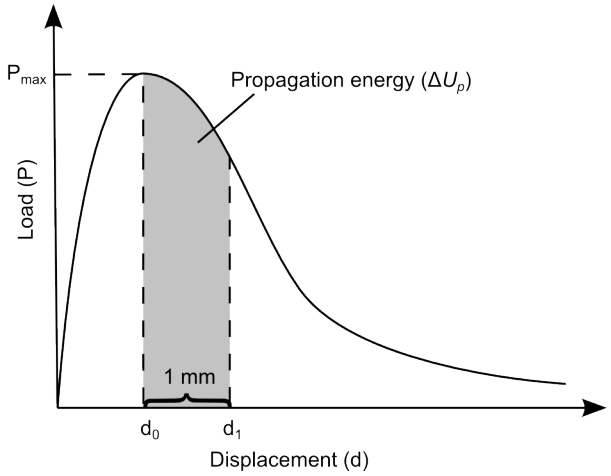

Figure 4.12: Schematic of data measured during the Kahn tear test.

Also using the load-displacement, the unit propagation energy from the load-displacement curve for a displacement of 1 mm from the maximum load (UPE_{d0-1}) is calculated according to:

$$UPE_{d0-1} = \frac{\Delta U_p}{B_0\,t} \tag{4.4}$$

where the ΔU_p is the propagation energy as determined by the load-displacement energy calculated by numerical integration using the trapezoidal rule from the displacement at maximum load to 1 mm from that displacement. The use of 1 mm for this measurement comes from the fact that buckling of the specimen was observed to occur in specimens sometime after this displacement.

While UPE_{d0-1} values represent a quick method to investigate crack propagation energies, a more rigorous method was determined to be desirable in order to validate the usage of UPE_{d0-1}. To that end, crack length measurements were used in the calculation of the tearing energy, E_{tear} which is calculated by:

$$E_{tear} = \frac{1}{t}\frac{\Delta U_p}{\Delta a} \tag{4.5}$$

where t is the specimen thickness, ΔU_p is the load-displacement energy calculated over the range of the crack length measurement, and Δa is the change of the crack length at two measured lengths. ΔU_p is the propagation energy calculated as discussed previously. The crack length measurements were done for samples at ambient temperatures. To measure the crack length for these tests, tests were interrupted intermittently past peak load by holding crosshead displacement constant. With the crosshead displacement held constant, the crack length is measured by observing the distance between position notch root and tip as observed by a travelling optical microscope. For each set of thicknesses, a polynomial fit to the crack length-displacement data from the point of maximum load and 1 mm of displacement is made. Using this polynomial fit, E_{tear} is calculated from $a = 0$ to $a = 3$ mm. For cold temperature tests, crack measurements were not possible. It is assumed that the crack growth-displacement relations measured at ambient temperatures will be valid throughout all the temperatures tested in this work so that the E_{tear} values can be calculated for all tests.

CHAPTER 5

Results

5.1 Welding Trials

In the welding trial, a total of nine welds were performed with successful temperature measurements. These consisted of at least two repeats of single torch, 2.75", 4", and 7" dual torch spacings. Cross-sections at the thermocouples were made, polished and then etched in 2% Nital to reveal the microstructures and to determine the position of the thermocouple relative to the fusion line. Figure 5.1 shows example macrographs and micrographs of a single torch and a 2.75" dual torch weld section. These two conditions show the smallest and largest HAZs with widths from the fusion line of approximately 1.2 mm and 2.6 mm respectively. The micrograph also shows that in these cases the thermocouples were placed within the HAZ, close to the fusion line. This is not true of all thermocouples, however, as in a number of cases where thermocouple measurements were lost due to molten weld metal penetrating the thermocouple hole. For surviving thermocouples it is seen that not every welding pass results in a HAZ measurement, which is expected as the initial placement was planned to measure the weld passes in the middle of the plate. For single torch welds, thermal cycle measurements in the HAZ are associated with the second and third fill pass. For the dual torch welds, it is primarily the first fill pass, which is a dual torch pass, that results in thermal cycle measurements within the HAZ.

Examples of measured temperature-time data and its associated filtered and corrected thermal cycle data from the weld trial for a single torch and a 2.75" dual torch case are shown in Figure 5.2.

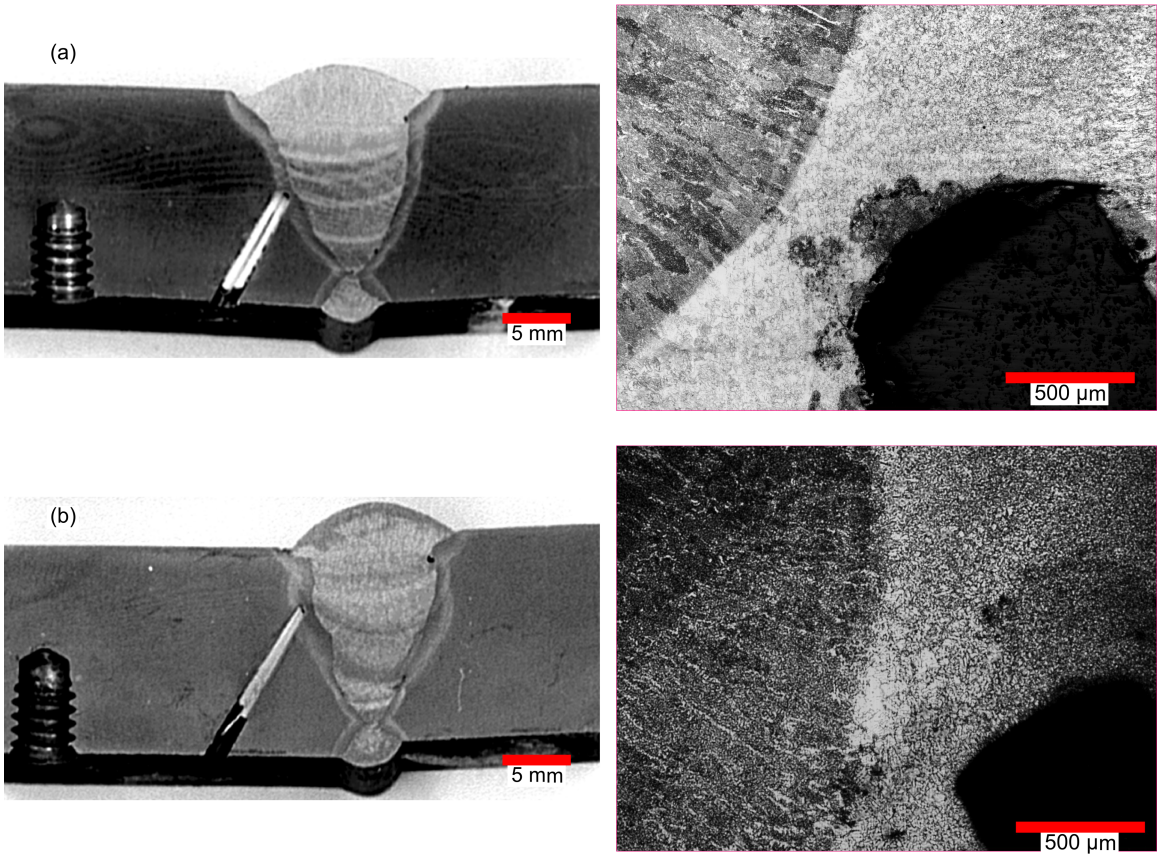

Figure 5.1: (a) Single torch weld macro picture and micrograph, (b) 2.75” dual torch weld macro picture and micrograph.

The correction applied to the raw data is two fold, as discussed previously in Section 5.1. First, filtering for noise from the welding process is applied, where Figure 5.2 clearly shows the weld on-off times by the appearance of this noise in the raw signal. Once the noise is removed a clear drop in the thermocouple signal is observed while the welding is occurring, which is then corrected for by adding the difference between the initial average signal temperature before welding begins and the initial average signal temperature after welding begins. The filtered and corrected peak temperature provides a more accurate value since it removes the noise that would at certain data points give higher peak temperatures than what is actually existing at the measurement location. The resulting filtered and corrected thermal cycle data is then used in further analysis.

To investigate the differences between single torch and dual torch, as well as the effect of torch spacing, Figure 5.3 summarizes the most pertinent thermal cycle data measured during the tests. This figure displays peak temperatures observed in the fully austenitic region and the associated

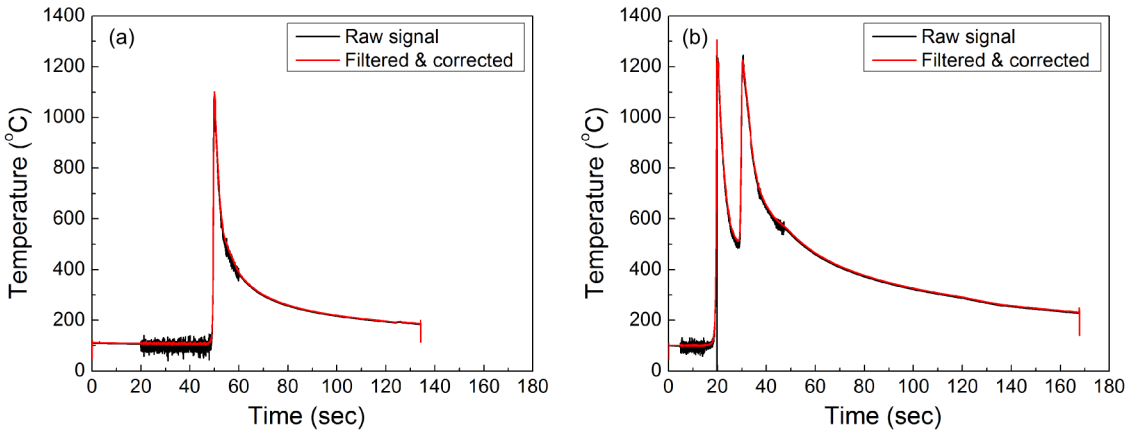

Figure 5.2: (a) Single torch and (b) 2.75" spaced dual torch weld thermal cycle measurements.

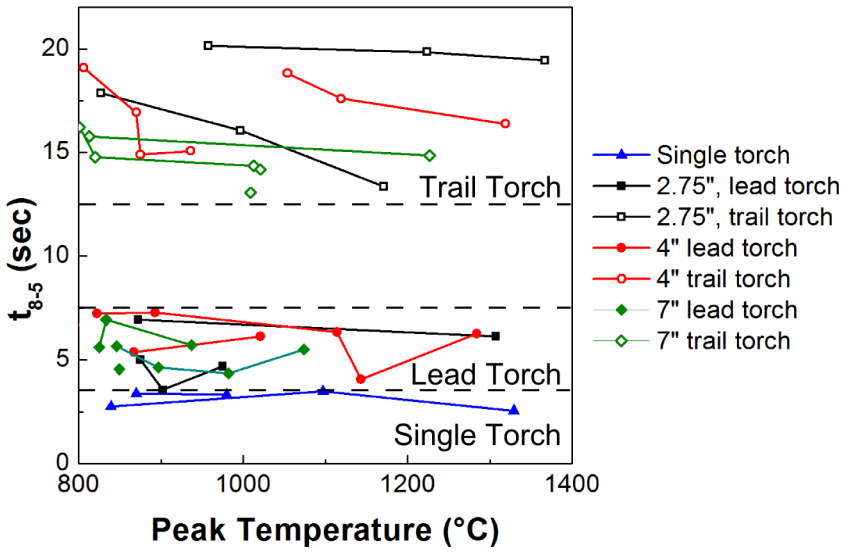

Figure 5.3: Measured peak temperature versus t_{8-5} from weld trials.

time to cool between 800 °C and 500 °C (t_{8-5}). Note that t_{8-5} is effectively an inverse measure of average cooling rate over this temperature range. It is seen that the t_{8-5} decreases slightly with peak temperature, which is to say average cooling rates increase with peak temperatures. It also shows that t_{8-5} times can be placed into three categories. The shortest t_{8-5} times are seen in single torch cases, which have an average of 3 seconds, giving an average cooling rate of 100 °C/sec. The lead torch of dual torch passes also have low t_{8-5} times, showing an average time of 5.6 second, which is equivalent to an average cooling rate of 54 °C/sec. The longest t_{8-5} times, with an average of 17

seconds, were seen in the trailing torch of dual torch passes, which gives an average cooling rate of 18 °C/sec. It is seen that the highest t_{8-5} time for trail torches is from a 2.75" torch spacing, while the lowest is seen to be from a 7" torch spacing. While the weld parameters are the same for each of these cases, the difference in t_{8-5} times makes sense as the lower torch spacings mean less time for heat from the lead torch to dissipate away from the weld line and thus act as an effective preheat for the the trailing torch.

For a more detailed look at cooling data, numerical differentiation was done on the temperature time data. This gives an instantaneous cooling rate with respect to temperature. Figure 5.4 shows an example of this data for each condition. In addition this figure also displays the region of transformation start temperatures as determined from the data of Reichert [147]. This shows that the cooling rate can significantly change with temperature in the temperature region that transformation is occurring. For instance, for the single torch case cooling rates over the transformation start temperature range begin at a high cooling rate of 135 °C/s and drops to a low value of 65 °C/s. Interestingly, it is seen in the trailing torch cases that a minimum value around 10 °C/s is reached and then maintained at temperatures above the end of the transformation start temperature range. Similar to the discussion

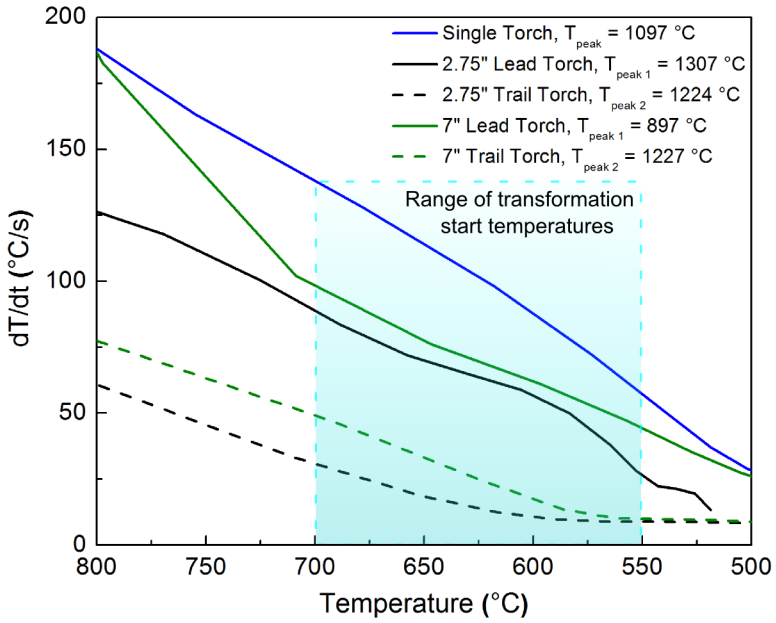

Figure 5.4: Instantaneous cooling rates through austenite decomposition temperatures.

of Figure 5.3 it is seen that the trailing torches give the lowest cooling rates, with a difference of about 60 °C/s at the start of the range of transformation start temperatures. This change in cooling rate with temperature over the range of transformation start temperatures is important as it will influence the final transformation products.

5.2 Gleeble Heat Treatments

In order to investigate the mechanical properties of microstructures in the HAZ, bulk specimens are required. Using the large testing strips with the Gleeble 3500 thermal-mechanical physical simulator, bulk microstructures that can be used for mechanical and fracture testing may be produced. Early in this work, a number of issues were addressed in using the large strips such as heating rate control, overshooting or undershooting peak temperatures, control over dwell times at peak temperatures, cooling rate consistency, temperature gradients along the length of the specimen, strip flatness, strip buckling and strip thinning. The 100 °C heating rate was selected because it was seen to be reproducible for the large strip specimen used. While this rate is significantly lower than measured heating rates of 1000 to 3000 °C/s during the weld trials in the actual HAZ, the work of Banerjee et al. [143] showed that heating rates of 100 °C/s and 1000 °C/s produced similar austenitic grain sizes. This data suggests that the use of 100 °C/s heating rate for Gleeble heat treatments would have little impact on the results of this study, which makes the use of large strips in this study feasible. Improvements were made to the temperature control programming in order to ensure peak temperatures even at the highest temperatures were consistent and dwell times kept to a minimum. A modification was made to the helium quenching system which provided improvement to gradient cooling effects as well as helping to maintain a consistent cooling rate. The thermal gradient across the width of the specimen was investigated but was found to be negligible. The change in the cooling system also helped with strip flatness issues by distributing the quenching gas over a wider area and with less pressure. Strip buckling or thinning at high temperatures was minimized with proper selection of piston air ram tension pressure to allow the thermal expansion without causing excessive strain.

Thermal cycle data measured during a typical heat treatment is shown in Figure 5.5 (a) and (b). These graphs show the first and second thermal cycles used in the creation of one of the most extreme conditions, the condition with Nb in solution with a prior austenite grain size of 42 μm and

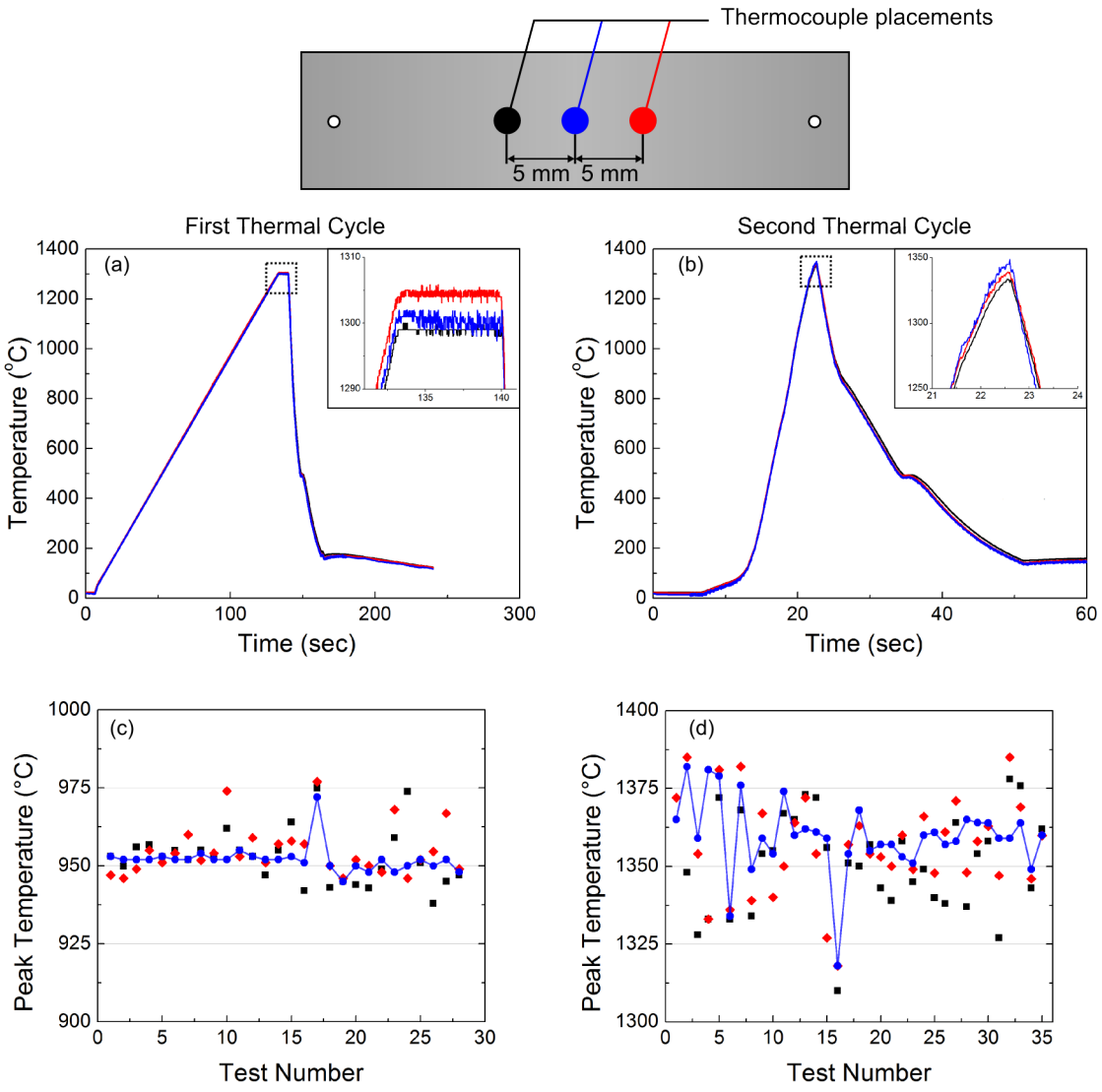

Figure 5.5: Thermal cycle data from a Gleeble heat treatment showing (a) stage one (b) stage two. Peak temperature recorded from all Gleeble heat treatments for centerline and 5 mm on either side off centerline for (c) 5 µm and (d) 42 µm thermal cycles.

a 50 °C/s cooling rate. This was also the most difficult condition to produce, due to the high temperatures for two thermal cycles in combination with the high heating and cooling rates observed. In both thermal cycles it is seen that the thermal gradient along the specimen is relatively minor, varying by about ±10 °C in the peak temperature region, while the time at maximum temperature is consistent at measured locations along the length of the specimen. The data also shows a kink in the cooling curve in both graphs at approximately 500 °C. This delay in the cooling is due to the re-

calescence due to the heat of the phase transformation occurring as the austenite phase decomposes. Earlier in the project, an effort was made to maintain a constant measured cooling rate in spite of the recalescence by increasing the gas quenching rate. While it proved possible to do so if prior information on the transformation temperature was known, it was determined that maintaining a constant quenching rate is more reliable and consistent. Figure 5.5 (c) and (d) shows the consistency in peak temperatures and thermal gradients for all tests. It is seen in Figure 5.5 (c) that for tests with a goal of 5 μm austenite grain size the peak temperature of 950 °C is consistently reached with ±10 °C for the middle thermocouple with the gradient also typically being less then 10 °C along the length. For tests with the goal of 42 μm austenite grain size, shown in Figure 5.5 (d), less consistency in obtaining the desired peak temperature of 1350 °C is seen. The deviation reaches as much as 34 °C for the center thermal measurement from the aimed peak temperature. The gradient is also seen to be larger for these heat treatments, typically showing a gradient within ± 15 °C of the centre thermocouple measurement. The issues as discussed previously, such as peak temperature control, dwell time control, strip flatness, thinning or buckling caused these tests with the aim of 42 μm to be extremely difficult to produce consistently. Furthermore, the use of K-type thermocouples for the outer measurements through both thermal cycles needed to produce 42 μm austenite grain sizes could result in a greater error in temperature measurement at these positions due to the high temperatures leading to diffusion at the thermocouple tips leading. The S-type thermocouples proved difficult to ensure a good connection suitable to control the Gleeble 3500 throughout the entire thermal cycle, particularly once the quenching system is turned on and the chamber fills suddenly with helium. Considering that the temperature is very high, (1350 °C), and the difficulties in producing these samples as discussed, and the fact that material was limited, the deviation from aimed peak temperature and the thermal are deemed acceptable for the purposes of this study.

5.3 Microstructures

The Gleeble heat treatments produced samples in eight different conditions in order to create microstructures for mechanical and fracture testing. To investigate what microstructures were produced, the main microstructural constituents were observed with samples etched with a 2% Nital solution in an optical microscope. Figures 5.6 and 5.7 show the Nital etched microstructure of the con-

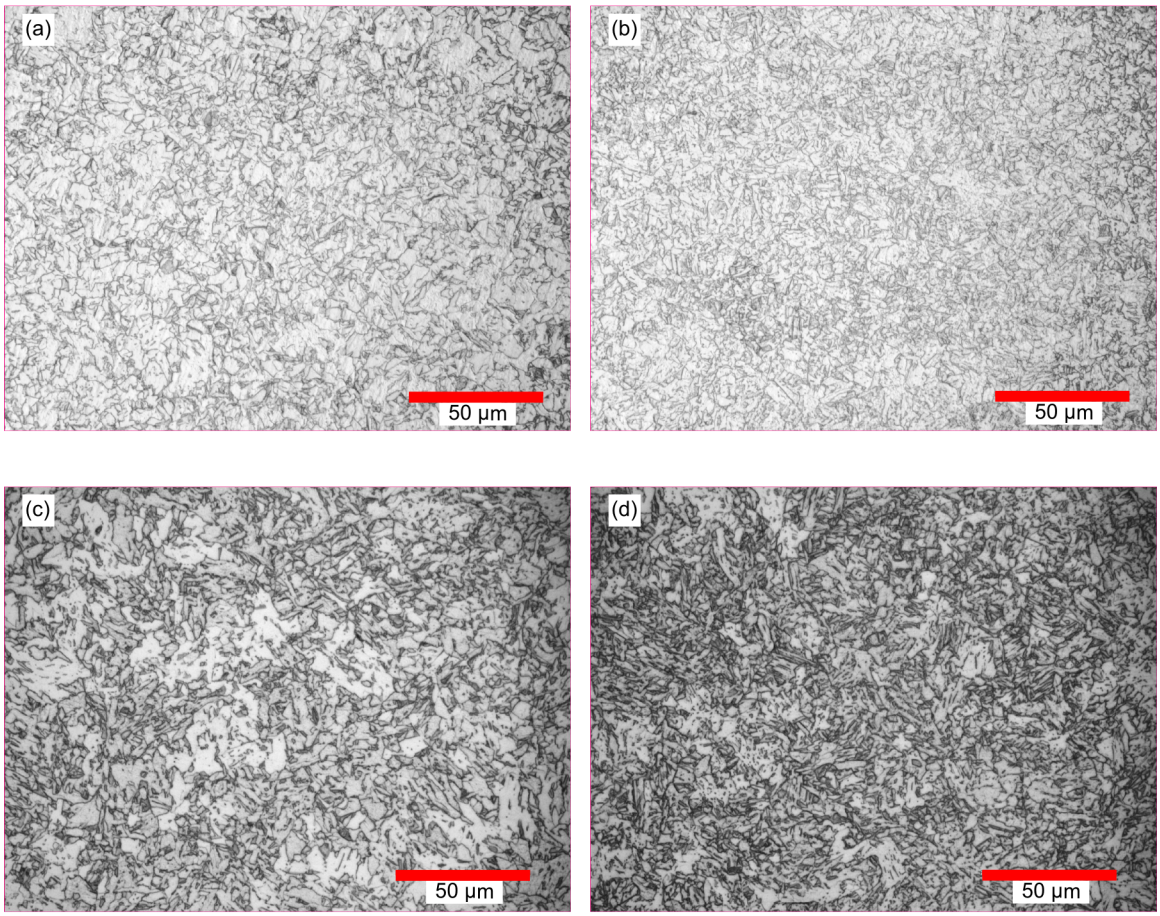

Figure 5.6: 2% Nital etchings of 5 µm prior austenite grain size with Nb in precipitates with cooling rates of (a) 10 °C/s and (b) 50 °C/s, and Nb in solution with cooling rates of (c) 10 °C/s and (d) 50 °C/s.

ditions with austenite grain sizes of 5 µm, and conditions 42 µm, respectively. The conditions with a prior austenite grain size of 5 µm and with Nb in precipitates show a mainly irregular ferritic microstructure. The effect of increasing cooling rate from 10 °C/s to 50 °C/s results in a refinement in the size of the microstructure. The refinement of microstructure with increased cooling rate is seen throughout all comparable conditions. The conditions with a prior austenite grain size of 5 µm and Nb solution present a very difficult microstructure to characterize. While there is a mix of ferrite and of upper bainite in these specimens, the refined microstructure in these samples in combination with similarities between the two phases made differentiation using the method used here not possible. The upper bainite phase, noted by irregularly shaped grains with internal structures is clearly seen throughout Figures 5.7 (a) and (b), which are specimens with Nb in precipitates with a prior

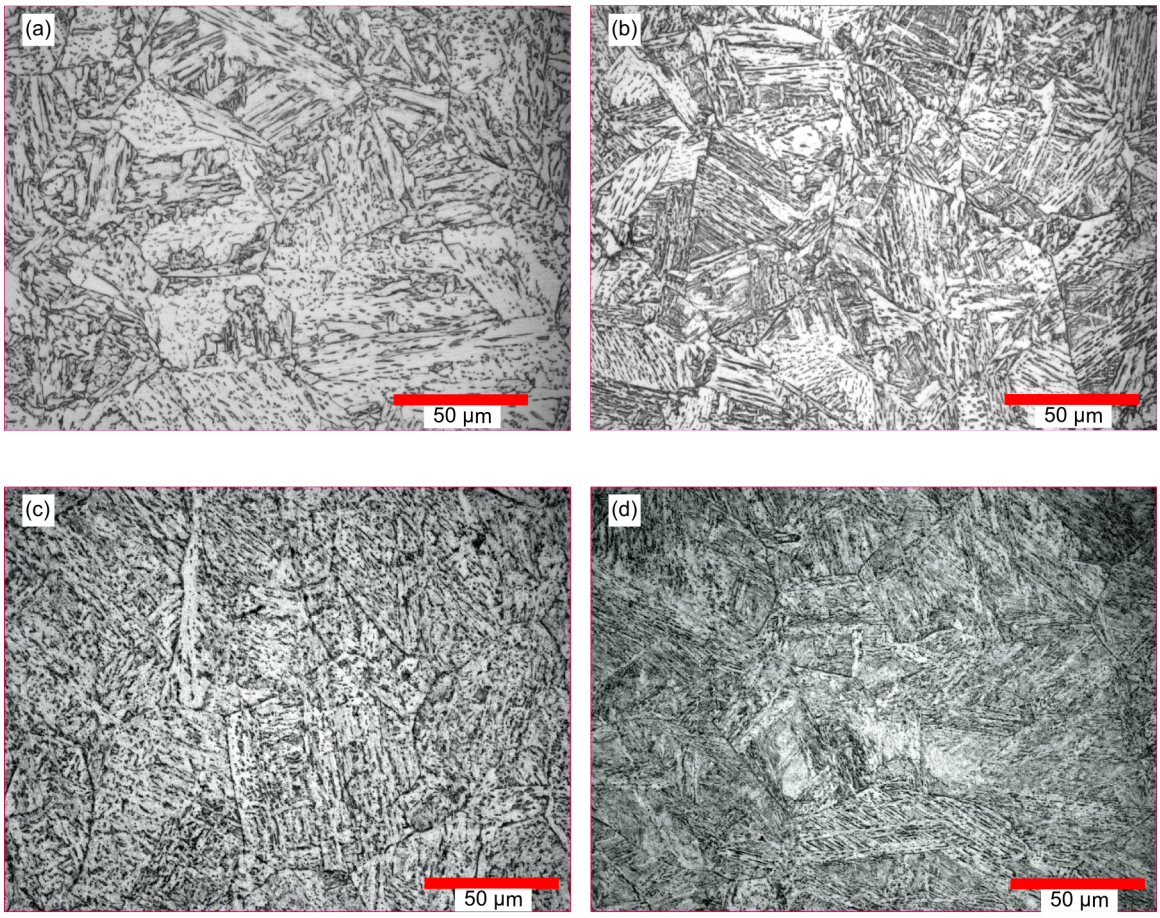

Figure 5.7: 2% Nital etchings of 42 µm prior austenite grain size with Nb in precipitates with cooling rates of (a) 10 °C/s and (b) 50 °C/s, and Nb in solution with cooling rates of (c) 10 °C/s and (d) 50 °C/s.

austenite grain size of 42 µm. In these micrographs lower bainite is also seen, which is observed by grain packets with lath-like structures and has a more continuous substructure compared to upper bainite. Lower bainite is seen more clearly in Figures 5.7 (c) and (d) as it makes up the main constituent of the microstructures with prior austenite grain size of 42 µm and Nb in solution. It is also of note that in the cases that bainite forms the primary microstructure, as in all images in Figure 5.7, remnants of the prior austenite grain boundary can be seen as the bainite packets do not completely remove the prior structure. Prior structures are not seen in the ferritic specimens.

Le Pera etching reveals the MA constituent of the microstructure. Le Pera etched microstructures are shown in Figures 5.8, and 5.9 for conditions with an austenite grain size of 5 µm, and

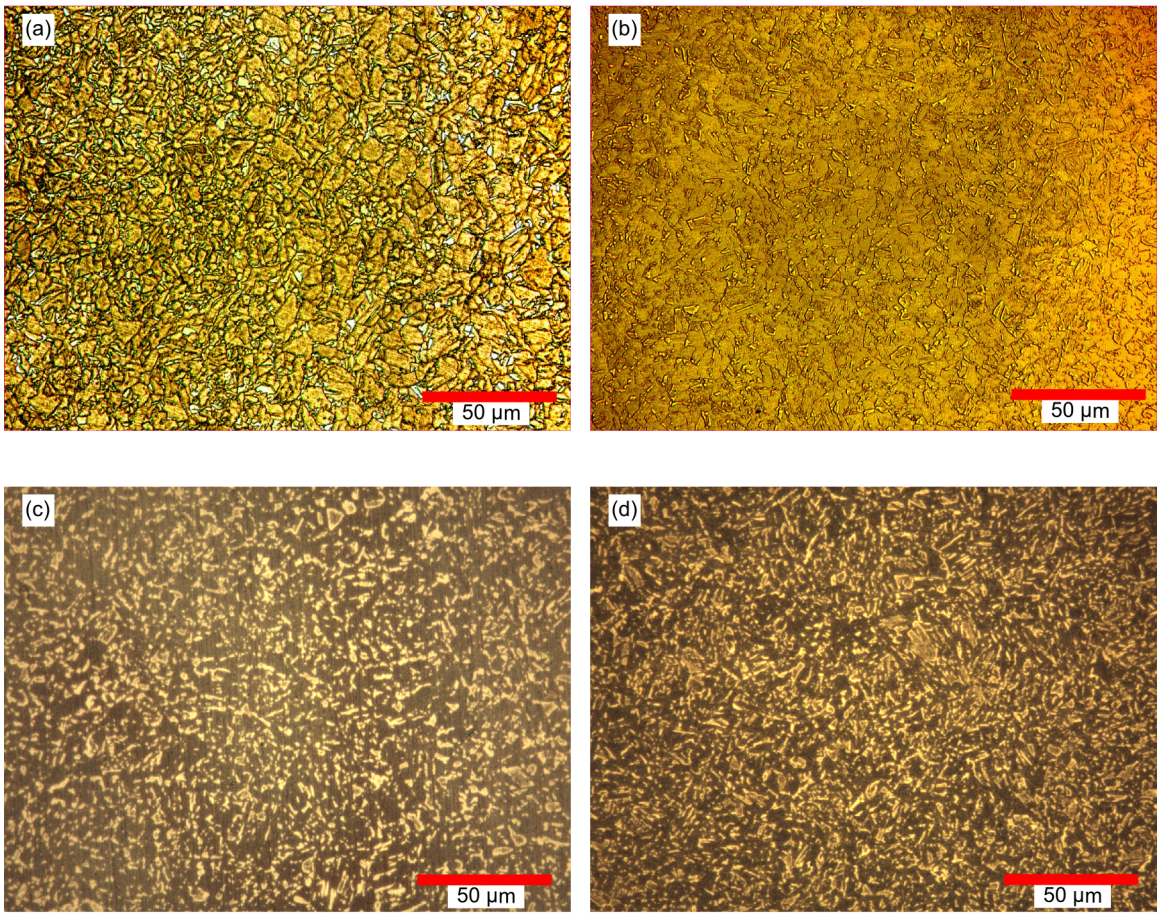

Figure 5.8: Le Pera etchings of 5 µm prior austenite grain size with Nb in precipitates with cooling rates of (a) 10 °C/s and (b) 50 °C/s, and Nb in solution with cooling rates of (c) 10 °C/s and (d) 50 °C/s.

conditions with an austenite grains of 42 µm respectively. MA is observed in these images by being brighter or white compared to the darker matrix. Little MA is seen in the conditions with Nb in precipitates and 5 µm prior austenite grain sizes. The MA in these ferritic specimens is disconnected, and dispersed fairly evenly throughout the microstructures. The amount of MA is noticeably greater for the mixed ferrite/upper bainite cases with Nb in solution and prior austenite grain size of 5 µm as seen in Figures 5.8 (c) and (d). The MA in these conditions is also more connected and less equiaxed. Some similarity in the MA appearance is seen between these conditions with austenite grain size of 5 µm and Nb in solution and the conditions with a prior austenite grain size of 42 µm and Nb in precipitates shown in Figure 5.9 (a) and (b). The MA phase in these specimens, as well as the conditions with prior austenite grain size of 42 µm and Nb in solution are at times difficult to de-

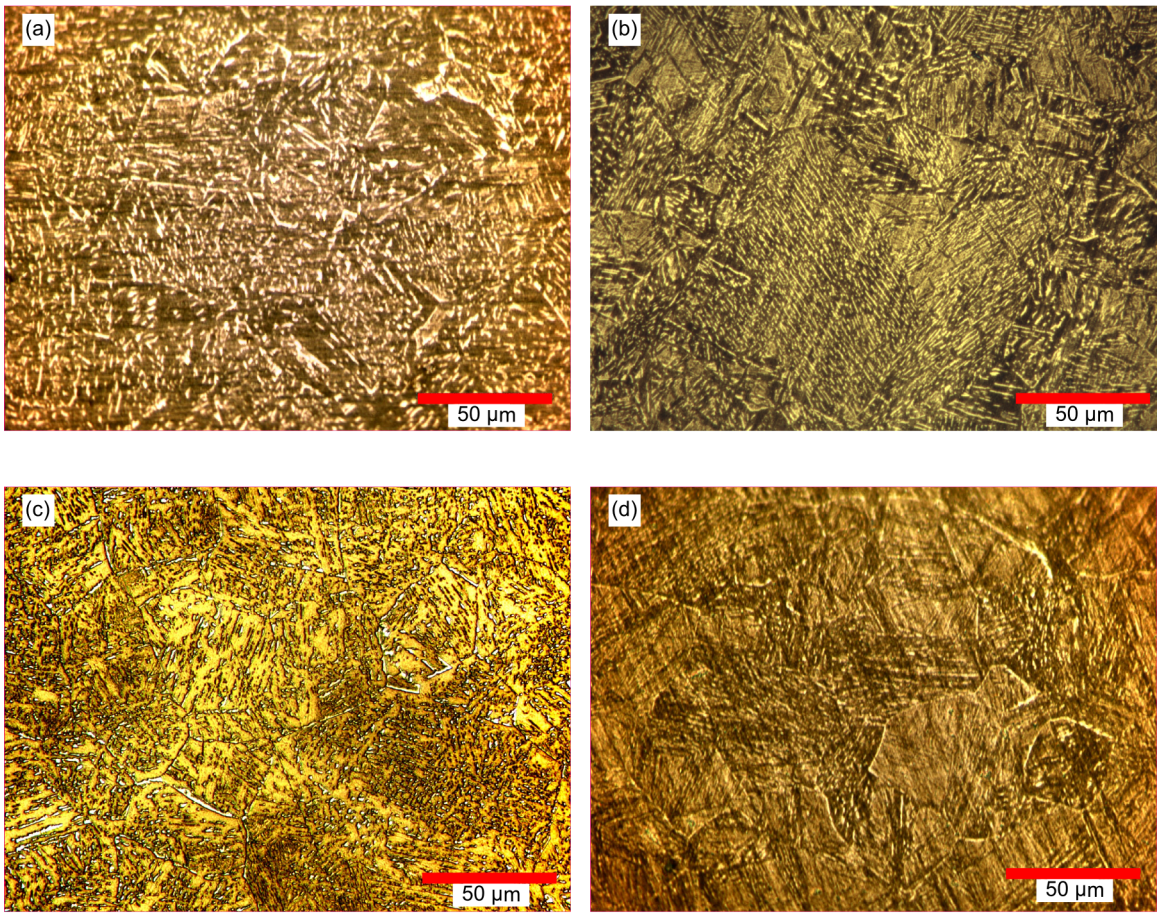

Figure 5.9: Le Pera etchings of 42 µm prior austenite grain size with Nb in precipitates with cooling rates of (a) 10 °C/s and (b) 50 °C/s, and Nb in solution with cooling rates of (c) 10 °C/s and (d) 50 °C/s.

termine due to a lack of contrast between the MA phase and the matrix. Notable though, conditions with prior austenite grain sizes of 42 µm and Nb in solution show less MA that is more elongated and appears to follow prior austenite grain boundaries.

Quantification of the microstructures according to the method outlined in Section 4.2 summarizes the previous discussion of observed microstructures. Figure 5.10 shows that the Gleeble heat treatments have produced microstructures with one of four primary constituents. The primary constituents are found to be either ferrite, upper bainite, lower bainite, or a complex mix of ferrite and bainite. Interestingly, it is seen that the highest MA fractions correspond with the primary constituent being of mixed ferrite-bainite or of upper bainite.

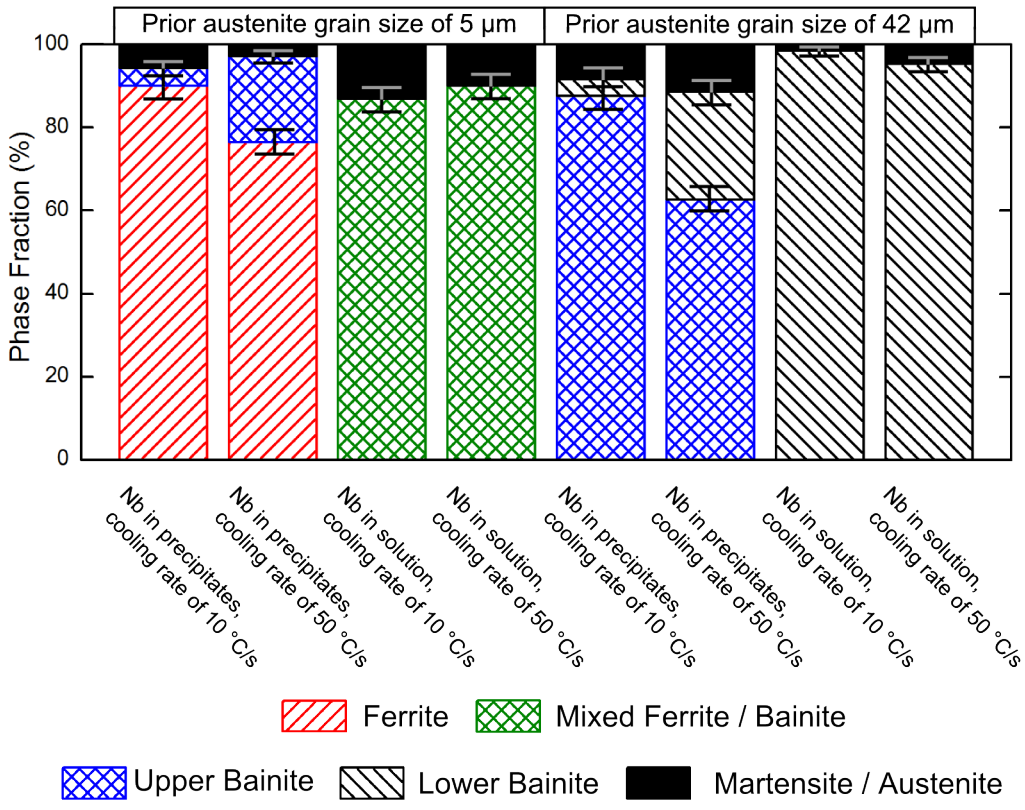

Figure 5.10: Measured microstructural constituents of the Gleeble heat treated samples.

5.4 Tensile Results

In the previous section it was seen that the Gleeble heat treatments produced a diverse range of microstructures. Tensile testing was carried out on these at three temperatures (ambient, -20 °C, -60 °C) on subsized tensile specimens for each condition. The engineering stress-strain curves for each condition at each testing temperature conditions with an austenite grain size of 5 µm and conditions with an austenite grains of 42 µm are shown respectively in Figures 5.11 and 5.12. Table 5.1 summarizes the important tensile testing data. All conditions show a ductile stress-strain response for each testing temperature. In some tests at the lower two temperatures, the immersible extensometer used reached its operating limit prior to failure. In these tests, the extensometer arms were moved during the test as this limit was being approached, and the strain past this point is not usable. In all tests where this movement was required, it occurred after necking has occured. This means that the true stress-strain data using the extensometer is valid since it can only be calculated up to the point of necking where the localization of strain causes thinning which cannot be measured

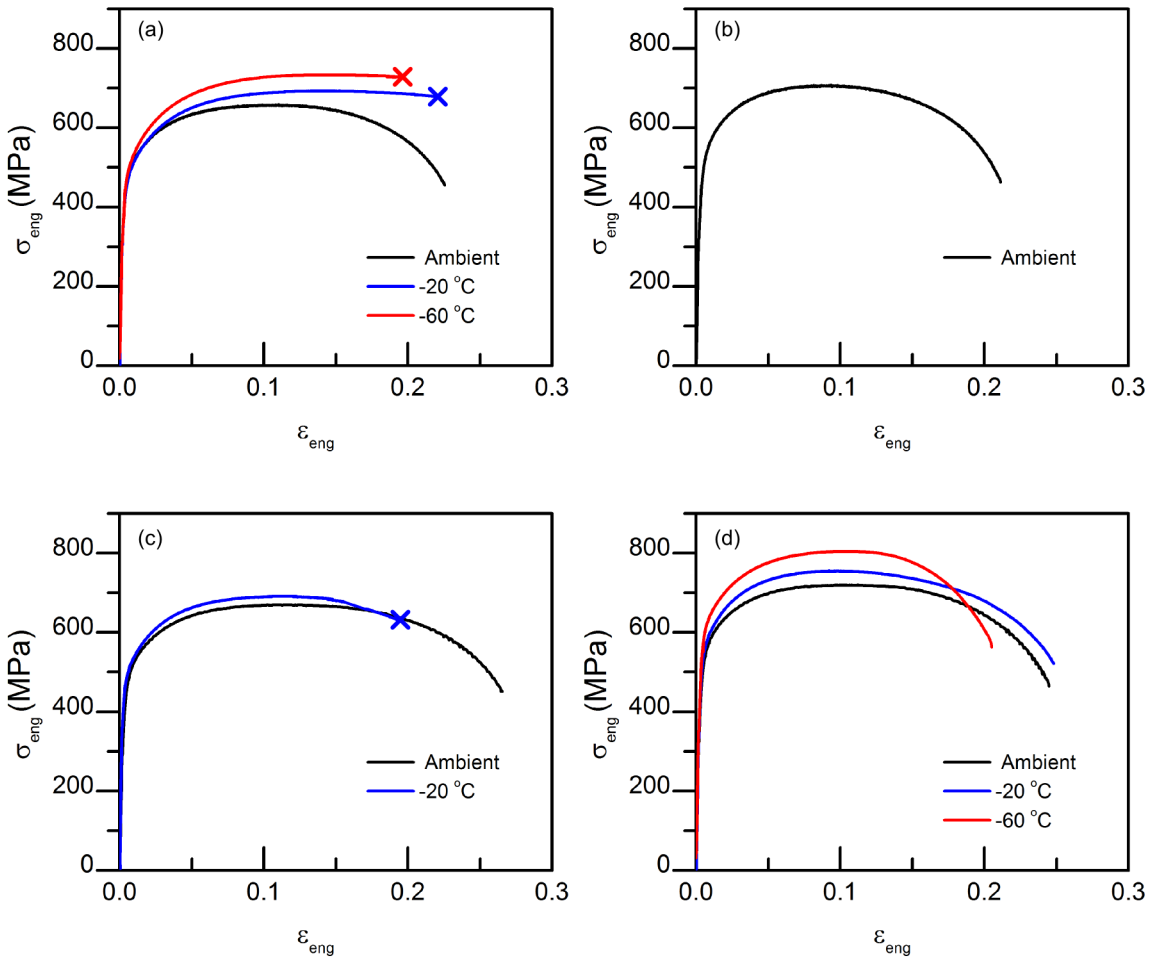

Figure 5.11: Engineering stress-strain of 5 μm prior austenite grain size with Nb in precipitates with cooling rates of (a) 10 °C/s and (b) 50 °C/s, and Nb in solution with cooling rates of (c) 10 °C/s and (d) 50 °C/s. Note that the 'X' marks the last usable extensometer data during the test (load measurements continued).

by the extensometer. It is also noted that there is a difference in the extensometer gauge length used between tests at ambient temperatures and the tests at -20 °C and -60 °C tests. The ambient temperature tests used a gauge length of 12.5 mm while the colder temperatures used a gauge length of 9 mm. The difference in gauge length does not influence measured strains during the uniform deformation prior to necking, but after the localization of strain in the neck the shorter gauge lengths will result in greater engineering strains compared to using larger gauge length.

From the engineering stress-strain plots (Figures 5.11 and 5.12) it can be seen that the ultimate tensile strength for every condition increases with decreasing testing temperature. Samples from all

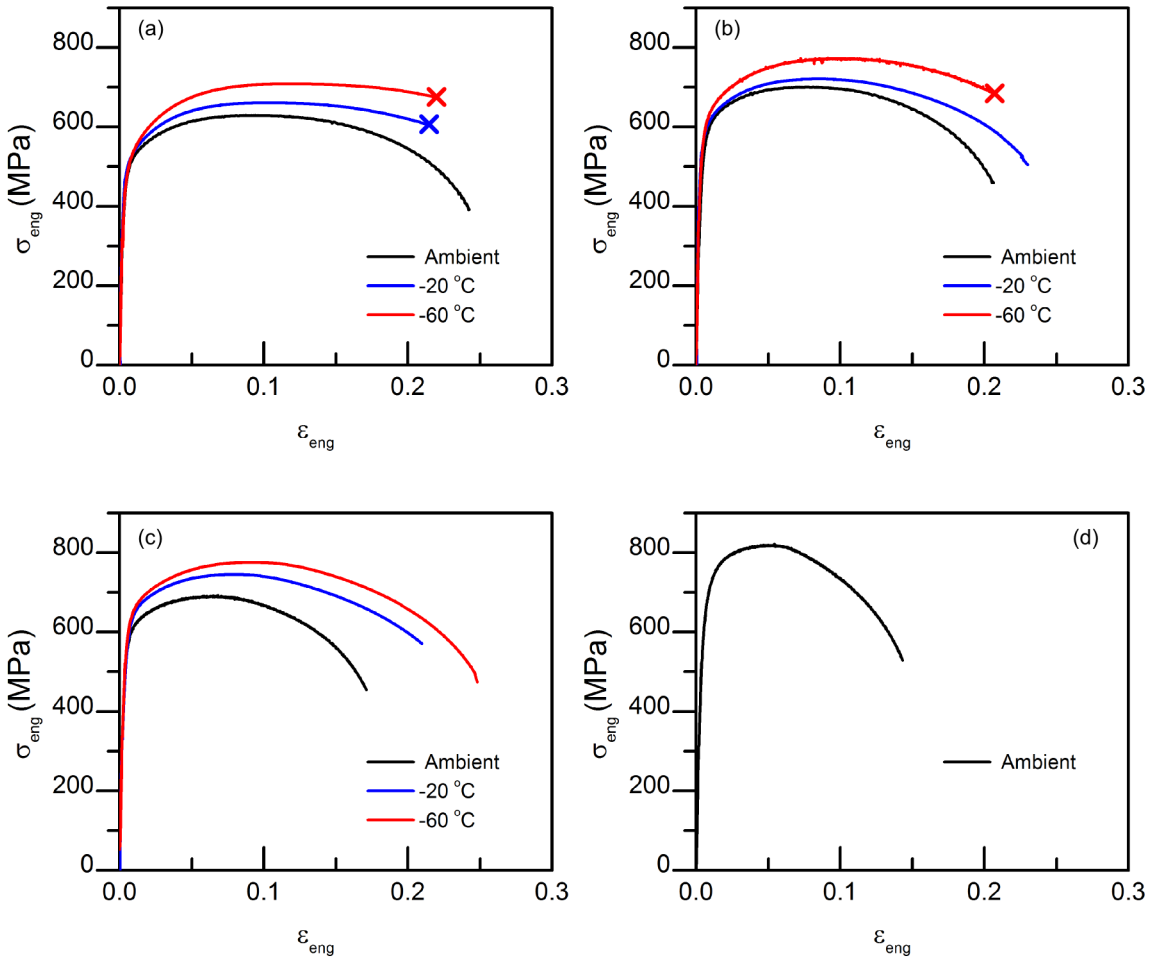

Figure 5.12: Engineering stress-strain of 42 µm prior austenite grain size with Nb in precipitates with cooling rates of (a) 10 °C/s and (b) 50 °C/s, and Nb in solution with cooling rates of (c) 10 °C/s and (d) 50 °C/s. Note that the 'X' marks the last usable extensometer data during the test (load measurements continued).

the heat treatments show a rounded curve throughout. In determining the yield stress with the typical 0.2% offset method, significant variation between samples were observed due to the sensitivity of this method to these rounded stress strain curves. This was resolved by using a 0.5% strain offset, which provided consistent results. Table 5.1 summarizes all measured tensile properties.

To further investigate the mechanical behaviour up until necking, the strain hardening rate was determined for each test and plotted with the true stress-strain data. This is shown in Figures 5.13 and 5.14 for conditions with an austenite grain size of 5 µm and conditions with an austenite grains of 42 µm respectively. All conditions show that necking occurs, which is defined by the point of plastic instability where the increase in strength due to strain hardening cannot keep in balance with

Table 5.1: Measured tensile properties

Type	Temperature	$\sigma_{ys\ 0.5\%\ offset}$ (MPa)	σ_{UTS} (MPa)	ε_{UEL}	ε_{frac}	σ_{frac} (MPa)	Number of tests
Nb in precipitates, 5 μm @ 10 °C/s Ferrite	Ambient	497	660	0.108	1.00	1443	5
	-20 °C	495	693	0.142	1.36	2157	1
	-60 °C	522	732	0.122	0.87	1245	2
Nb in precipitates, 5 μm @ 50 °C/s Ferrite	Ambient	547	707	0.092	1.20	1846	6
	-20 °C						
	-60 °C						
Nb in solution, 5 μm @ 10 °C/s Mixed Ferrite/Bainite	Ambient	511	669	0.113	1.14	1604	3
	-20 °C	518	705	0.160	1.11	1685	1
	-60 °C						
Nb in solution, 5 μm @ 50 °C/s Mixed Ferrite/Bainite	Ambient	563	715	0.097	1.10	1582	2
	-20 °C	590	756	0.092	1.14	1853	1
	-60 °C	628	805	0.102	0.97	1697	1
Nb in precipitates, 42 μm @ 10 °C/s Upper Bainite	Ambient	510	630	0.091	1.42	1853	2
	-20 °C	522	662	0.105	1.61	2397	1
	-60 °C	523	709	0.116	1.08	1466	1
Nb in precipitates, 42 μm @ 50 °C/s Upper Bainite	Ambient	589	697	0.075	1.39	2110	3
	-20 °C	602	722	0.084	1.56	2729	1
	-60 °C	633	770	0.082	1.02	1596	2
Nb in solution, 42 μm @ 10 °C/s Lower Bainite	Ambient	602	692	0.061	1.30	1835	3
	-20 °C	625	746	0.078	1.46	2814	1
	-60 °C	640	776	0.090	1.16	1796	2
Nb in solution, 42 μm @ 50 °C/s Lower Bainite	Ambient	716	806	0.046	1.50	2633	4
	-20 °C						
	-60 °C						

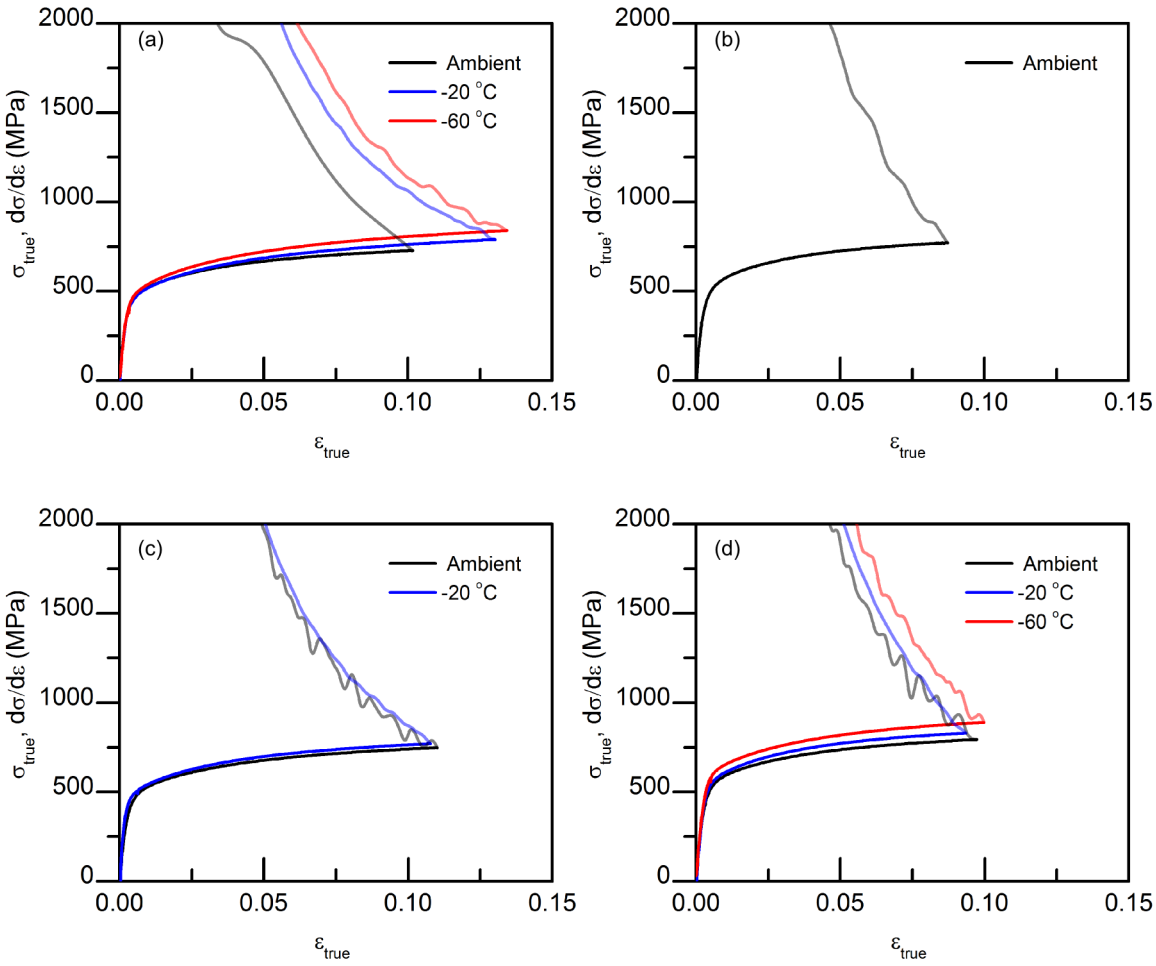

Figure 5.13: True stress-strain and strain hardening rate of 5 µm prior austenite grain size with Nb in precipitates with cooling rates of (a) 10 °C/s and (b) 50 °C/s, and Nb in solution with cooling rates of (c) 10 °C/s and (d) 50 °C/s.

the increased stress from a thinning section, referred to as the Considère condition. As there is no measurement of the cross-sectional area in the necked region, no true stress data is usable after this point with exception of the final point at fracture which will be discussed later. From these figures it is seen that at a given amount of strain the strain hardening rate is higher as testing temperature decreases. Exceptionally, for the two mixed ferrite/bainite microstructure conditions with Nb in solution and an austenite grain size of 5 µm there is not much strain hardening rate difference with decreasing temperature (i.e. Figure 5.13 (c) and (d)), whereas all other conditions did show significant differences.

The true stress-strain data from tests has so far provided information on the tensile behaviour up until the point of necking. Post-test examinations were used to investigate post necking behaviour

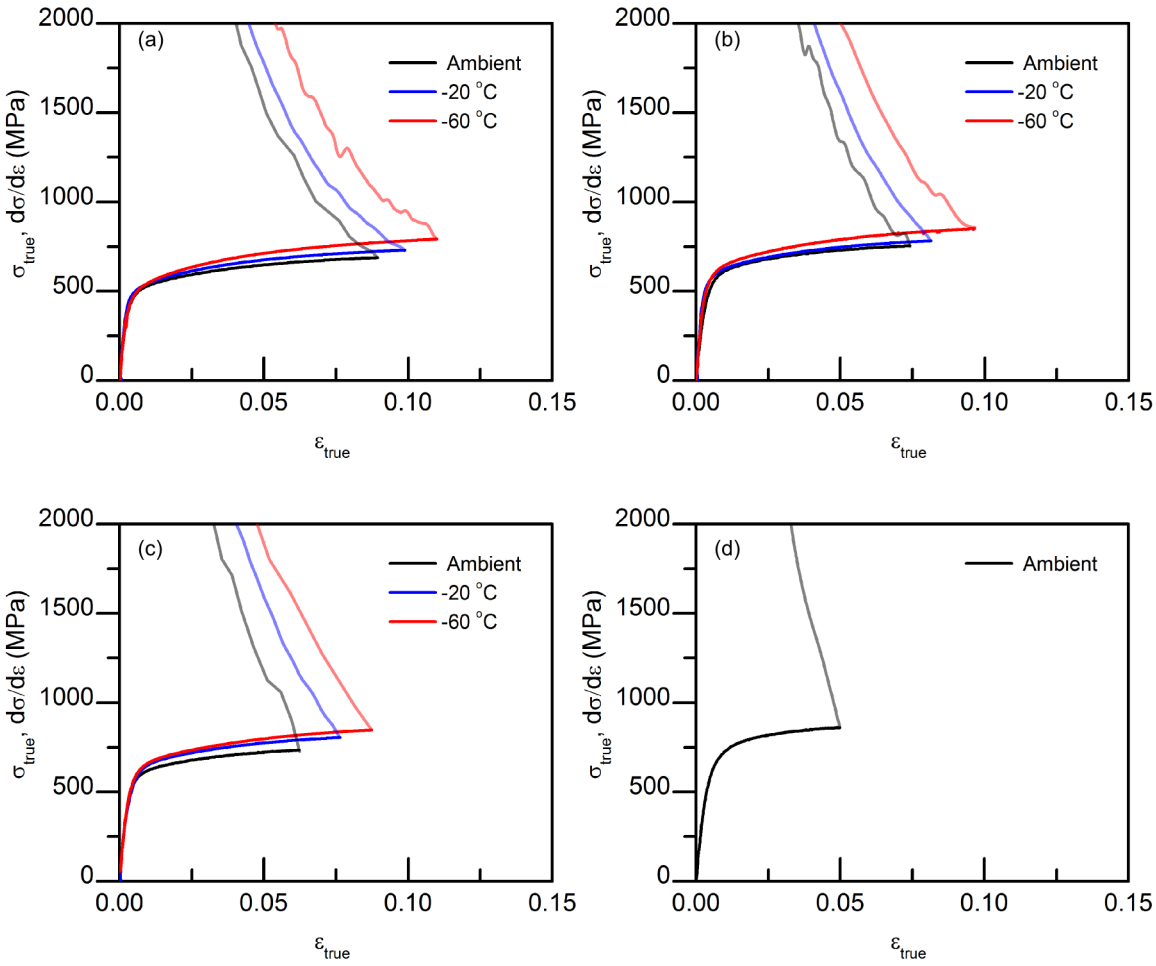

Figure 5.14: True stress-strain and strain hardening rate of 42 µm prior austenite grain size with Nb in precipitates with cooling rates of (a) 10 °C/s and (b) 50 °C/s, and Nb in solution with cooling rates of (c) 10 °C/s and (d) 50 °C/s.

at a single point, the point of failure. This was accomplished by measuring the final fracture area using SEM images. Figure 5.15 (a) and (b) show examples of typical SEM images of a tensile fracture surface used in the measurement of the final fracture measurement. As part of the post-test investigation, observations of the failure surface were also made and tests that showed significant deviation from a flat fracture surface at failure were not used to calculate true fracture strain and stress. Macrographs in Figure 5.15 (c) and (d) show typical flat and invalid slant failure respectively. With the final fracture surface area measured for the cases of flat failure, calculation of the true stress and true strain is determined, and corrected according to the method discussed in Section 4.5.

With the true fracture stress corrected, Figures 5.16 and 5.17 plot true stress-strain until fracture at each testing temperature for conditions with an austenite grain size of 5 µm and conditions with

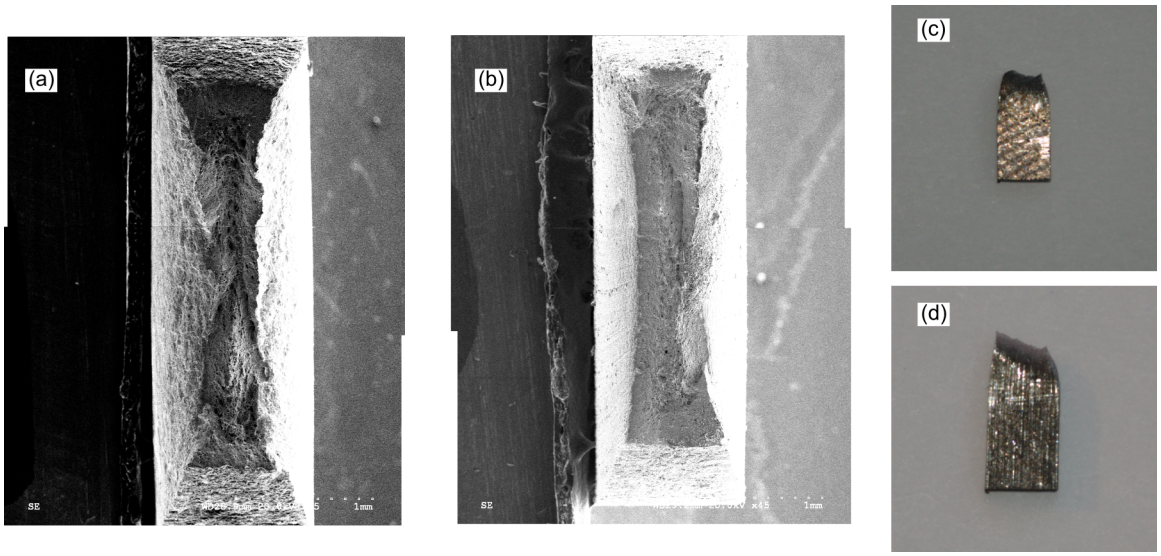

Figure 5.15: SEM images of tensile fracture surface of (a) Nb in solution with cooling rate of 50 °C/s and (b) Nb in precipitates with cooling rate of 50 °C/s. (c) Typical flat fracture surface and (d) unacceptable slant failure.

an austenite grains of 42 μm respectively. These graphs show that microstructures formed with a prior austenite grain size of 42 μm generally have higher values of true stress and true strain at fracture than microstructures formed with a prior austenite grain size of 5 μm. In Figure 5.16 (c) and (d) it is seen that the conditions with a prior austenite grain size of 5 μm with Nb in solution, microstructures that are composed of a mix of ferrite/bainite, have similar values for true stress and true strain at fracture across all testing temperatures.

The effect of temperature on tensile properties is summarized in Figure 5.18. It is seen that the tensile strength and yield strength both increase with decreasing temperature, with an average of 76 MPa and 37 MPa respectively across all conditions when going from ambient to -60 °C. However, there are some interesting deviations from this trend. The case with Nb in solution with prior austenite of grain size of 42 μm, which is a lower bainite microstructure, shows a large increase in tensile strength (122 MPa) compared to the average. With respect to engineering strain at the point of necking (i.e. maximum engineering strain under uniform elongation), which is shown in Figure 5.18 (c), it is seen that this value generally increases with decreasing temperature. The largest exception to this is the case with Nb in precipitates with prior austenite of grain size of 5 μm which is a ferritic microstructure where uniform elongation engineering strain increases then

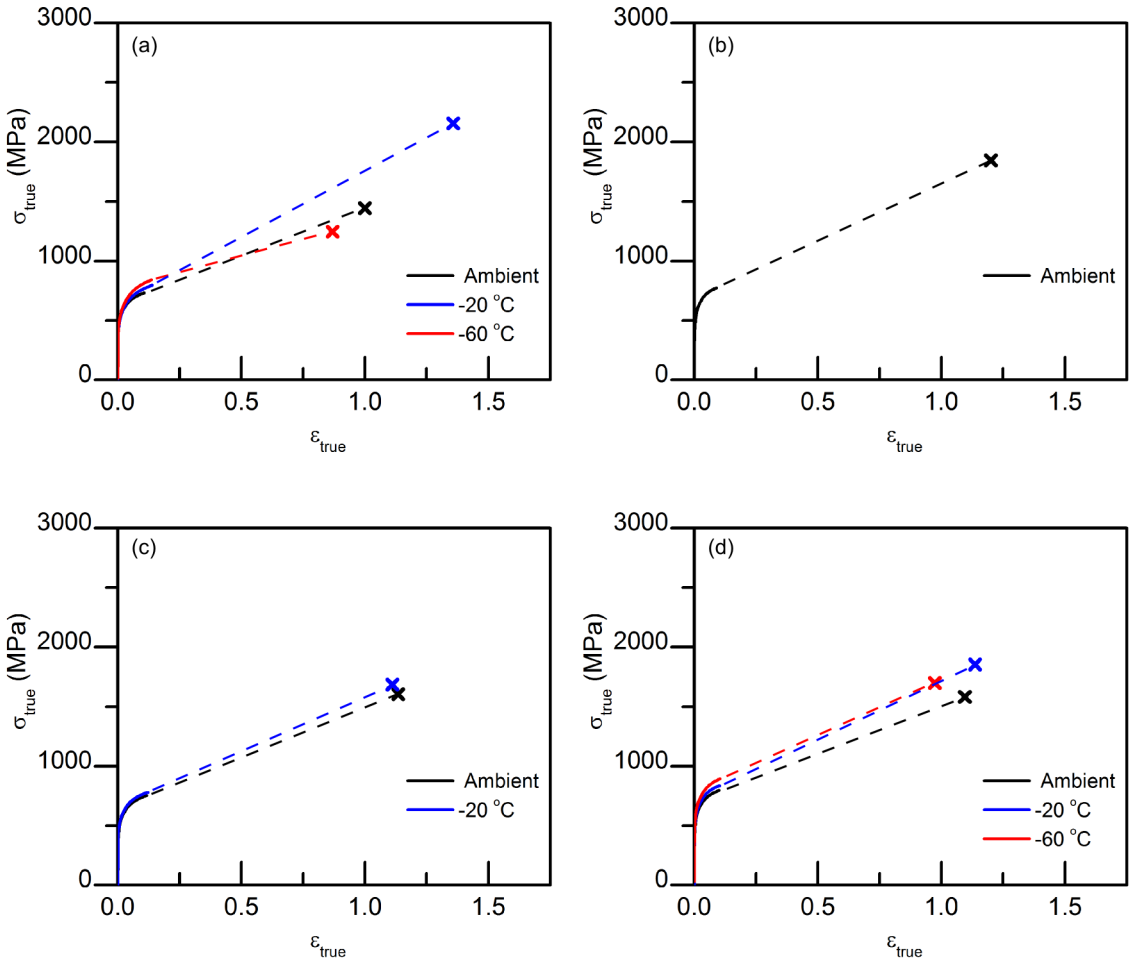

Figure 5.16: True stress-strain to failure of 5 µm prior austenite grain size with Nb in precipitates with cooling rates of (a) 10 °C/s and (b) 50 °C/s, and Nb in solution with cooling rates of (c) 10 °C/s and (d) 50 °C/s.

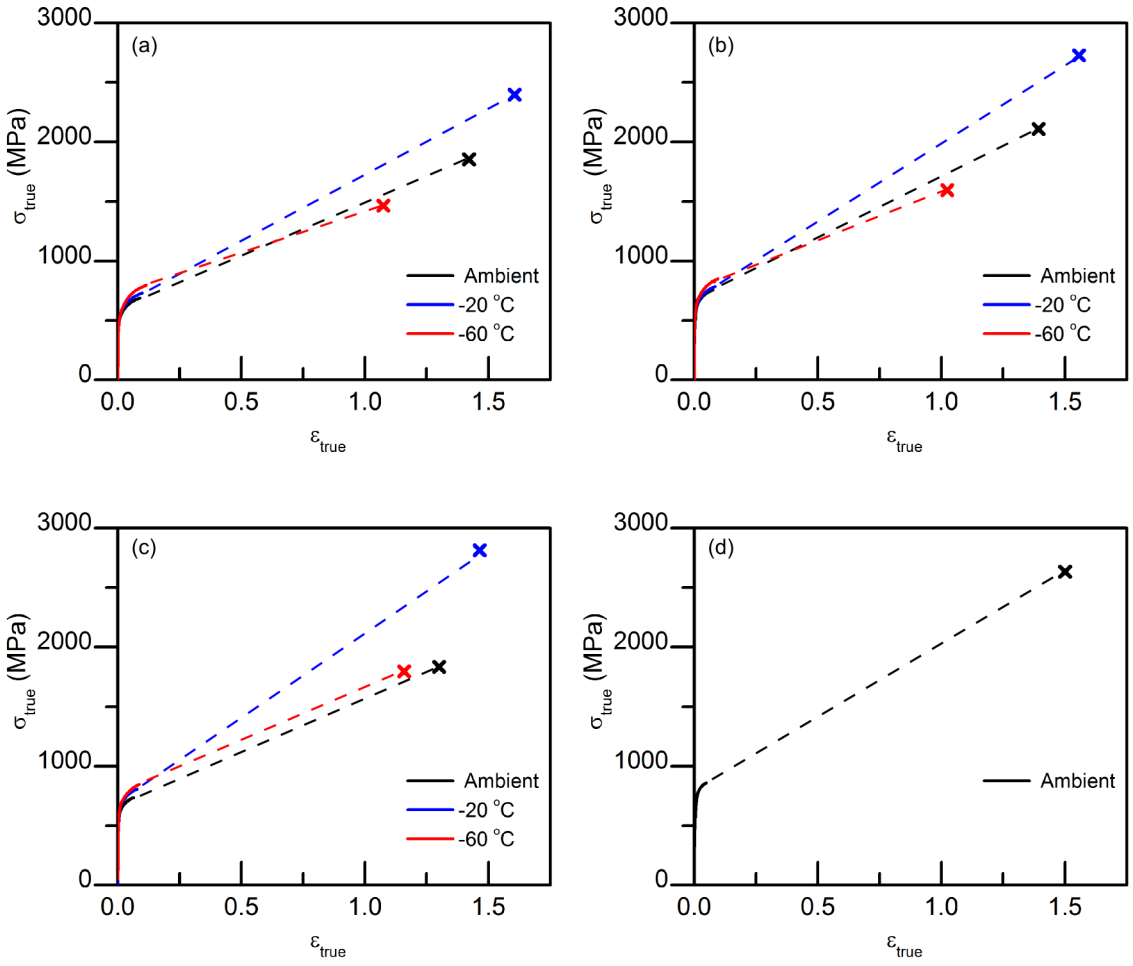

Figure 5.17: True stress-strain to failure of 42 µm prior austenite grain size with Nb in precipitates with cooling rates of (a) 10 °C/s and (b) 50 °C/s, and Nb in solution with cooling rates of (c) 10 °C/s and (d) 50 °C/s.

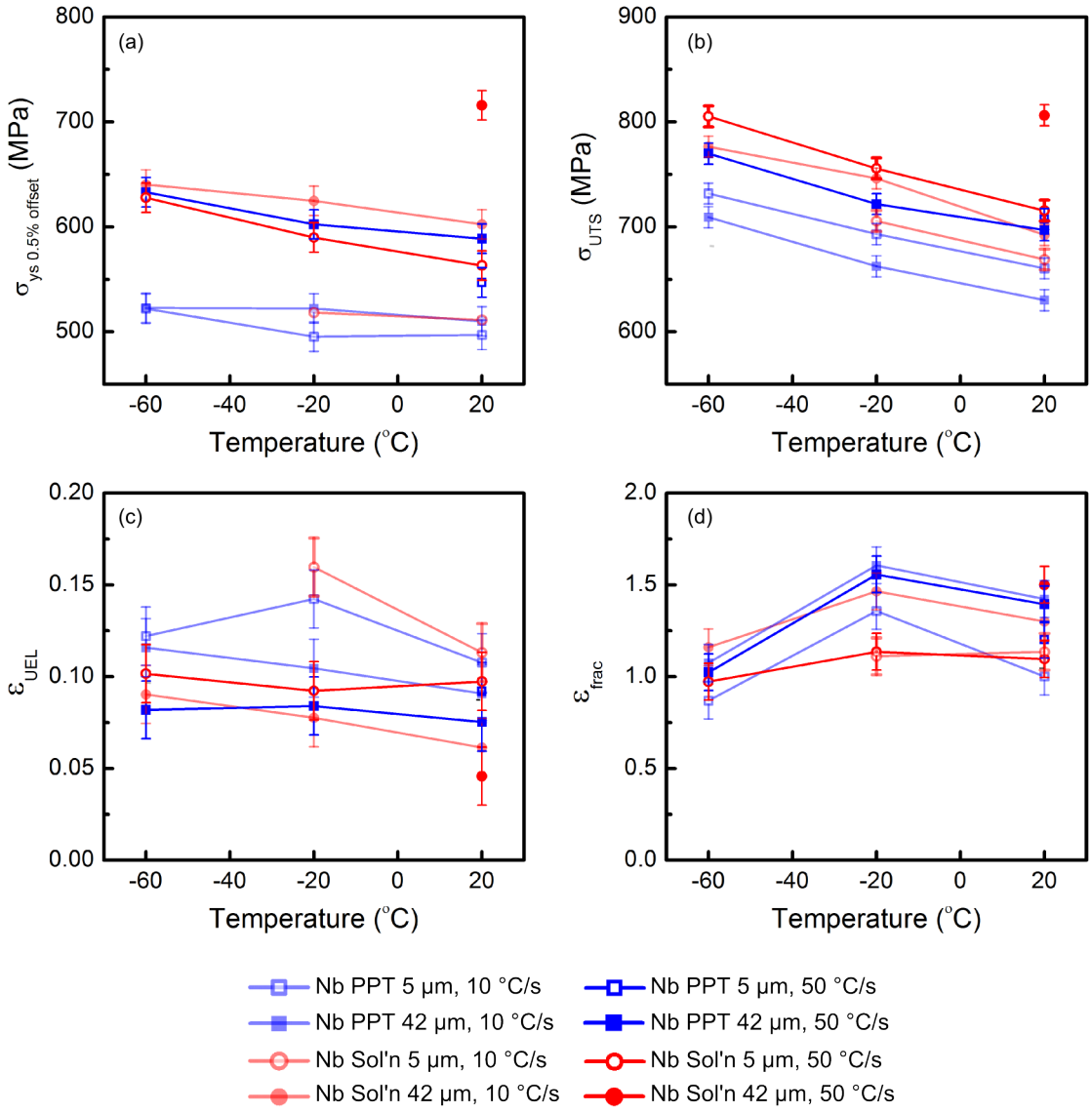

Figure 5.18: Temperature dependence of (a) yield strength, (b) ultimate tensile strength, (c) engineering uniform elongation, and (d) true strain at fracture.

decreases as temperature decreases. The two cases with upper bainite as the main constituent, that is the case with Nb in solution with a prior austenite grain size of 42 µm show a behaviour where the engineering strain at the point of necking only increases a small amount with decreasing temperature. The observation of final fracture strains in Figure 5.18 (d) show a different trend with temperature. From ambient temperature to -20 °C there is an increase in true strain at fracture for all samples except the condition with a prior austenite grain size of 5 µm and Nb in solution cooled at 10 °C/sec where the value decreases. From -20 °C to -60 °C it is seen that the true fracture strain

drops for every condition. The drop is most severe for the condition with a prior austenite grain size of 5 μm with Nb in precipitates and a cooling rate of 10 °C/sec which is a ferritic microstructure. Larger drops over this temperature range are also noted in the conditions with a prior austenite grain size of 42 μm and Nb in precipitates which are primarily upper bainitic microstructures.

5.5 Kahn Results

Kahn tests for each microstructural condition were carried out at different temperatures. For comparison, load divided by thickness is plotted against the displacement adjusted so that the peak load is reached at zero displacement. These plots are shown for the 5 μm prior austenite grain size and 42 μm austenite grain size conditions in Figures 5.19 and 5.20 respectively. Note that a number of the ambient temperature tests in these figures show small load drops; these are associated with holding displacement constant during optical crack length measurements. Results of the Kahn tests show similarities in trends to the tensile tests. Decreasing temperatures result in increased maximum normalized loads reached and thus tear strengths observed, trending similar to the effect seen with ultimate tensile strength in the tensile testing. The condition of 42 μm prior austenite grain size and 50 °C/s cooling rate, a microstructure with primarily lower bainite, shows the highest tear strength, similar to the tensile tests where it showed the highest ultimate tensile strength. The condition of a 5 μm prior austenite grain size with Nb in and 10 °C/s cooling rate shows the lowest tear strength, similarly in the tensile tests this condition showed the second lowest ultimate tensile strength. Crack length data during testing was limited by the travel length of the microscope. Within the crack measurements observed it is seen that crack lengths increase at approximately the same rate with displacement for each condition.

From the Kahn test's load and displacement data, UPE_{d0-1} and E_{tear}values were calculated according to the method discussed in Section 4.6. While UPE_{d0-1} values represent a quick method to investigate crack propagation energies, E_{tear} provides a more rigorous method which was used to validate the usage of UPE_{d0-1} and investigate thickness effects. In order to determine the values of a used in the calculation of E_{tear}, crack measurements of all specimens were categorized and combined by sample thickness into groupings close to 1.1 mm, 1.25 mm, 1.5 mm, 2.0 mm, and 2.5 mm in thickness. Then a polynomial fit to the crack displacement data was made between the point of maximum load and 1 mm of pin-to-pin displacement from that point. These fits to crack length

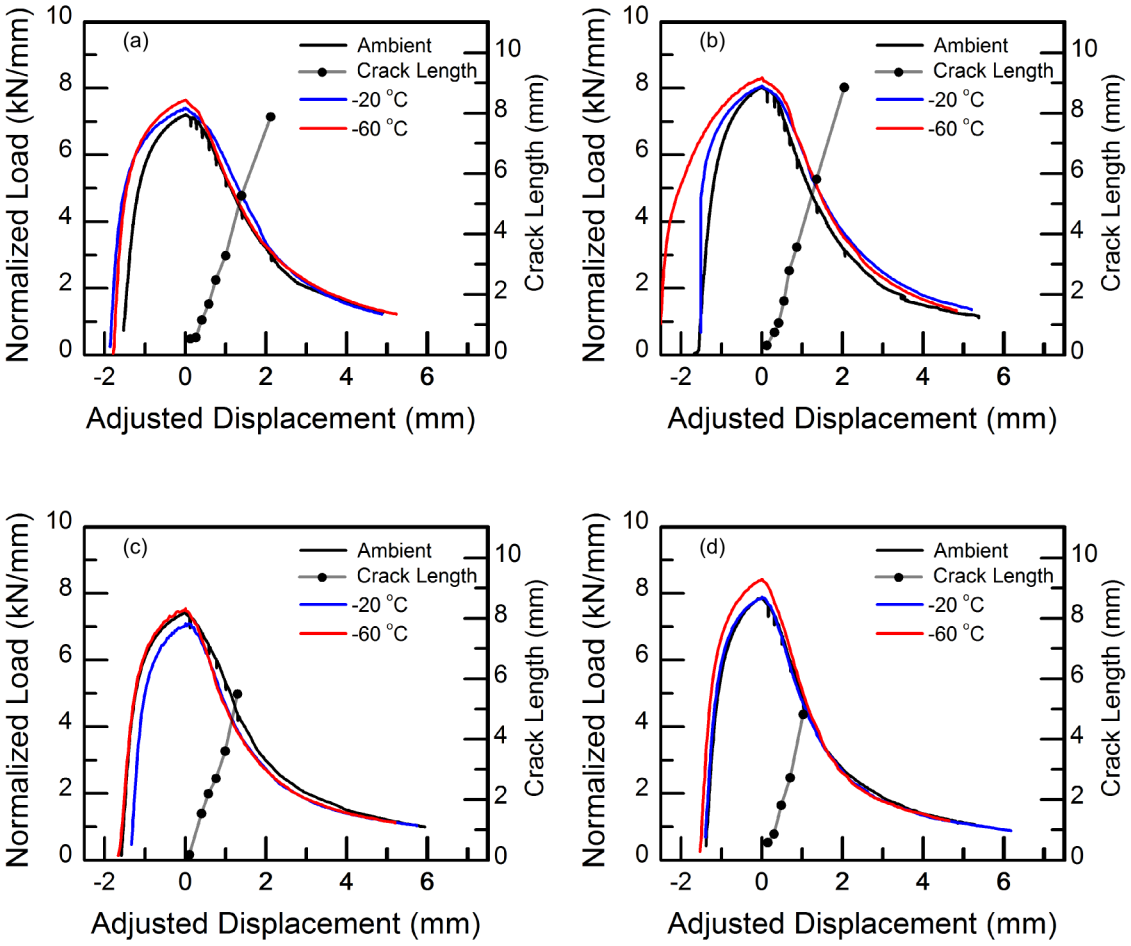

Figure 5.19: Kahn tear test results of 5 µm prior austenite grain size with Nb in precipitates with cooling rates of(a) 10 °C/s and (b) 50 °C/s, and Nb in solution with cooling rates of (c) 10 °C/s and (d) 50 °C/s

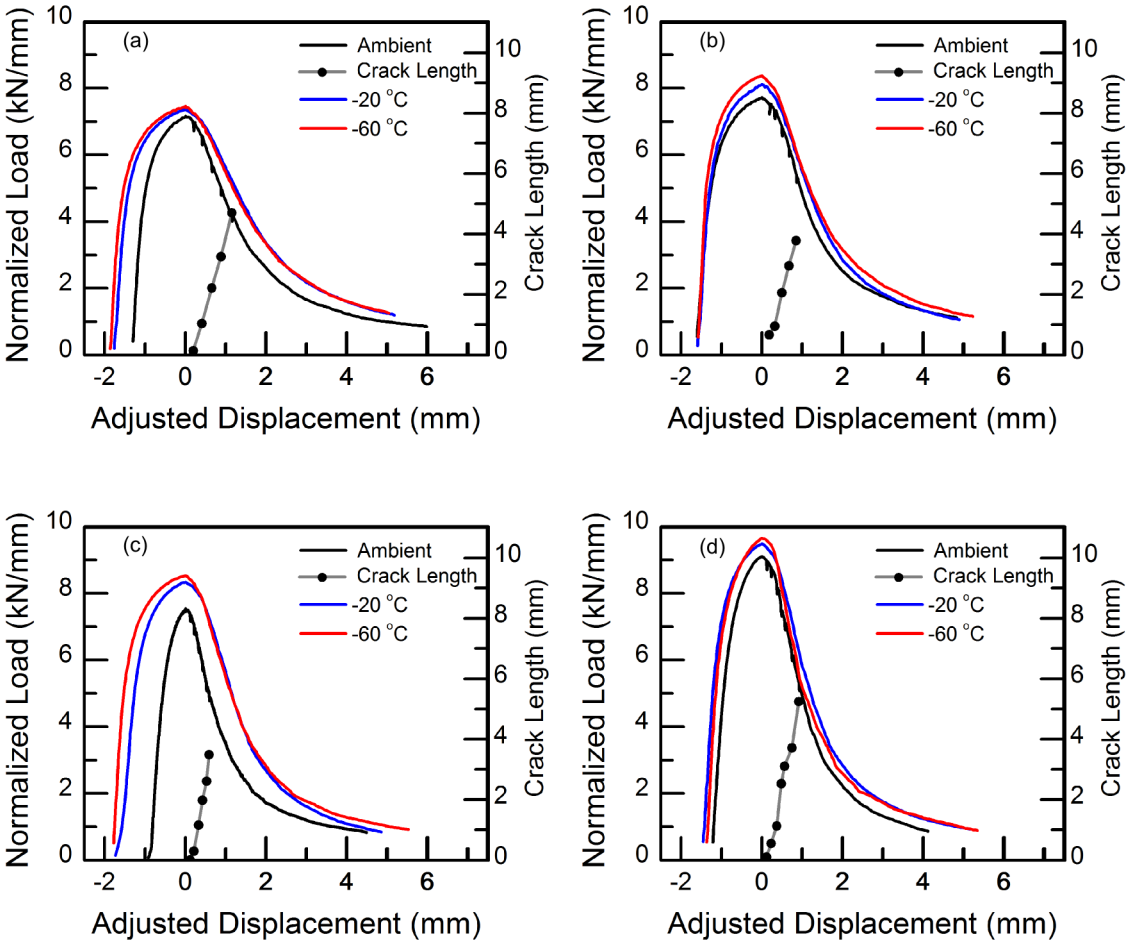

Figure 5.20: Kahn tear test results of 42 µm prior austenite grain size with Nb in precipitates with cooling rates of(a) 10 °C/s and (b) 50 °C/s, and Nb in solution with cooling rates of (c) 10 °C/s and (d) 50 °C/s

displacement data are shown in Figure 5.21. These figures show that with thicker specimens, crack length increases slightly less with pin displacement compared to thinner specimens. The thinner specimens also show a greater scatter in crack length measurements overall. It is assumed that the room temperature crack length measurements and fits to crack length will remain applicable to tests at colder temperatures. This assumption is made because crack measurements were not possible due to the nature of immersion testing. It is is believed that this assumption is reasonable since all tests remain ductile and that the crack growth should be geometrically driven.

The fit to crack length data was then used to determine the E_{tear} values. This was done over each data point for the first millimeter of adjusted displacement, which can be used to construct E_{tear} curves such as the two shown in Figure 5.22. Note in Figure 5.22 (a) that the appearance of load

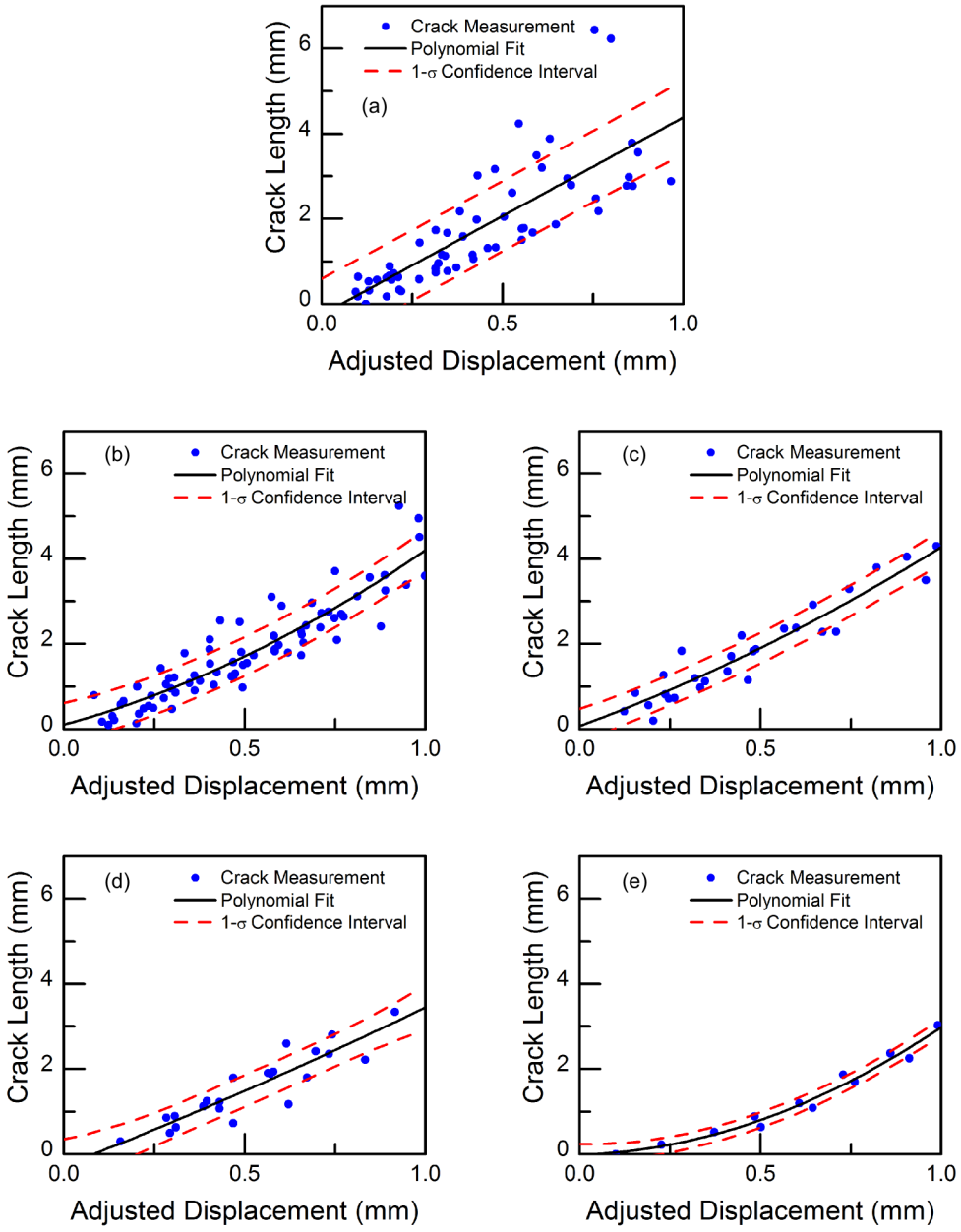

Figure 5.21: Curve fitting of crack length versus adjusted displacement for tests with thickness close to (a) 1.15 mm (b) 1.25 mm (c) 1.5 mm (d) 2.0 mm (e) 2.5 mm

drops in this figure clearly show that they represent a very small deviation from the otherwise regular curve and thus it is reasonable to assume that negligible crack growth occurred during the crack length measurements. The decrease in E_{tear} value with increasing crack length may be attributed to the fact that thinning of the specimen is not accounted for in the calculation. Figure 5.23 shows two examples of the Kahn surface after fracture. With the notch of the specimen on the right side of these images it is clear that the sample has thinned after the initial crack growth toward the left from the notch as part of the fracture process. If E_{tear} used the current thickness instead of the initially measured thickness, the E_{tear} may not show the decrease as seen in Figure 5.22. For comparison to UPE_{d0-1} values, the E_{tear} value was taken at 1 mm of adjusted displacement without any correction to thinning of the specimen.

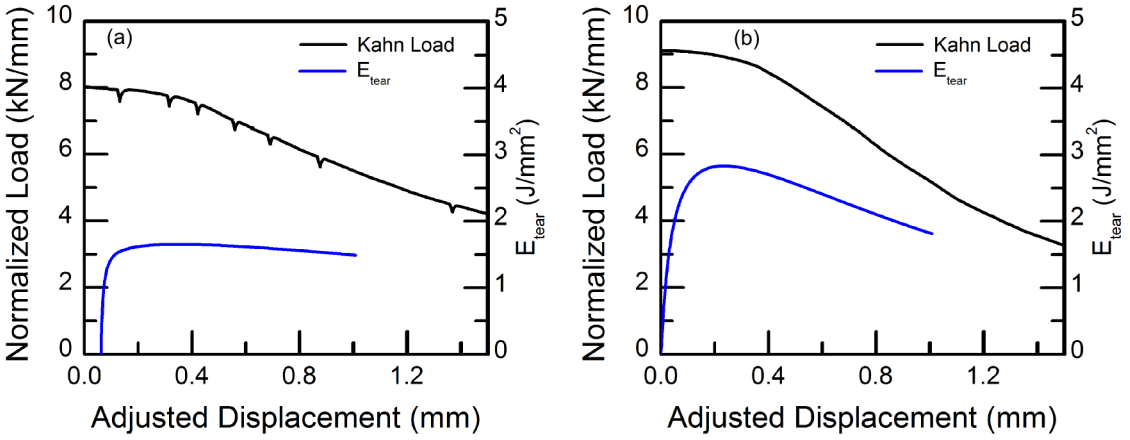

Figure 5.22: E_{tear} curves determined based on fitted fitted crack data for (a) Nb in precipitates, 42 µm prior austenite grain size with cooling rate of 10 °C/s and (b) Nb in solution, 42 µm prior austenite grain size with cooling rate of 50 °C/s.

The role of thickness on E_{tear} and UPE_{d0-1} values was investigated using the as-received condition. Figure 5.24 shows that E_{tear} and UPE_{d0-1} values for the as-received conditions increase with thickness. Thus, to use E_{tear} and $UPE_{d0-1}$to compare results, a correction for the thickness effect was needed. To do so required normalizing each test by a test of the same condition that was closest to a set thickness. The set thickness that the correction would be made to was decided to be 1.2 mm as this was close to the average thickness for most thermally treated specimens. With each test normalized, tests that were close in thickness (within 0.05 mm) had their values averaged. To this normalized E_{tear} and UPE_{d0-1} values we reduced to an average point for specimens close

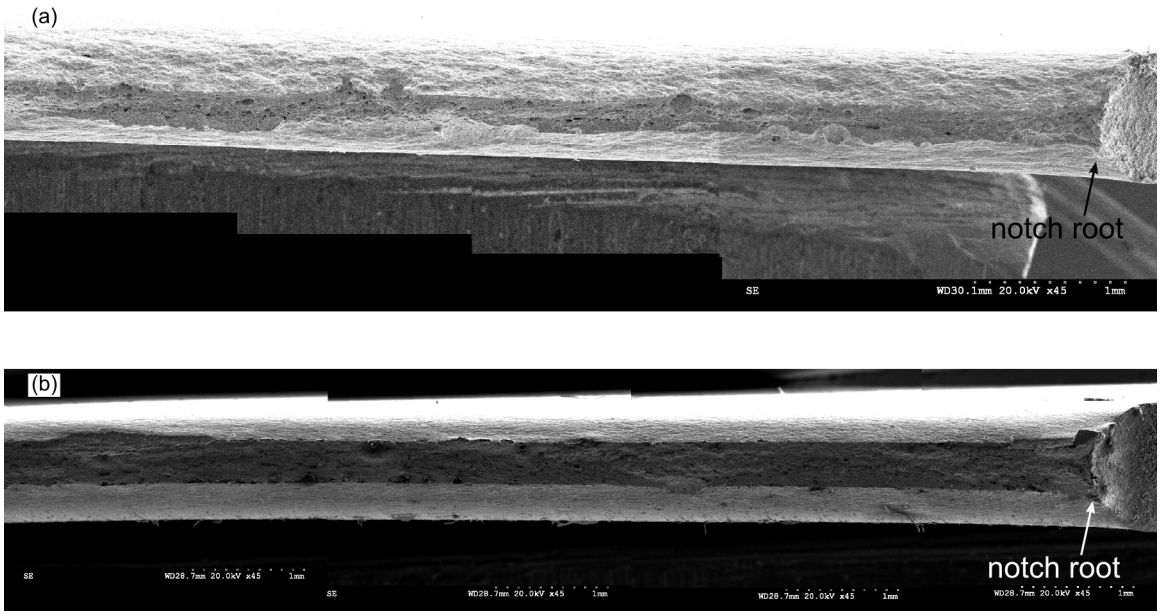

Figure 5.23: SEM images of Kahn fracture surface of (a) Nb in precipitates, 42 μm prior austenite grain size with cooling rate of 10 °C/s and (b) Nb in solution, 42 μm prior austenite grain size with cooling rate of 50 °C/s.

in thickness and a curve was empirically fitted to the data. Fitting of the E_{tear} and UPE_{d0-1} with respect to thickness is shown in Figure 5.25, and the fitting equation takes the form of:

$$\text{Normalized Energy Fit} \quad = \quad c_1(1-\exp(-c_2(t-c_3))) \tag{5.1}$$

where t is thickness, c_1, c_2, and c_3 are constants, and the normalized energy fit value is calculated separately for E_{tear} and UPE_{d0-1} with differing values of the constants. For E_{tear} fitting, c_1 is 1.11, c_2 is 2.6, and c_3 is 0.4. For UPE_{d0-1} fitting, c_1 is 1.135, c_2 is 2.5, and c_3 is 0.4.

With a curve fitting for E_{tear} and UPE_{d0-1} with respect to thickness, a correction for thickness to these values was applied. The effect of this correction is shown in Figure 5.26. In these graphs it can be seen, particularly when considering the as-received material which covers a wide range of thicknesses, that the trend of E_{tear} and UPE_{d0-1} to increase with thickness has been reduced. From these figures it is seen that there are differences in using E_{tear} and UPE_{d0-1}. For instance, the maximum E_{tear} values are seen to be from the condition with with a prior austenite grain size of 42 μm and Nb in solution with a cooling rate of 50 °C/s which is primarily lower bainite structure with

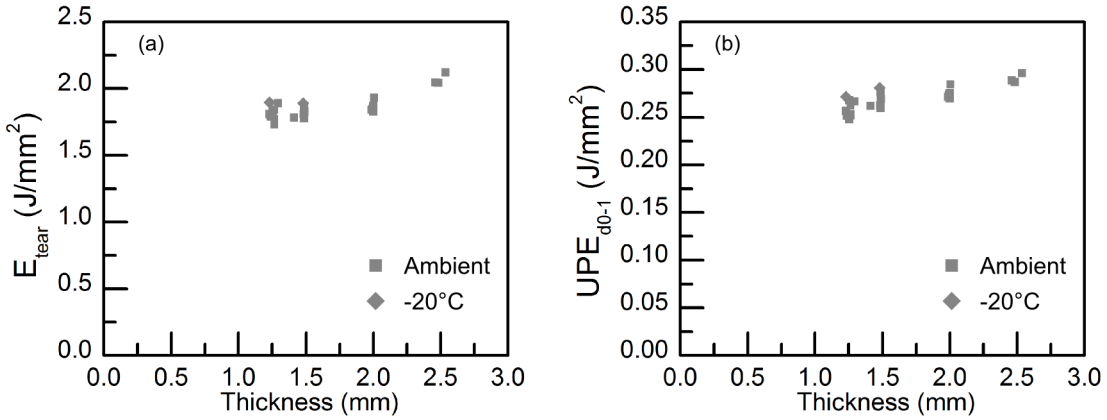

Figure 5.24: (a) E_{tear} and (b) UPE_{d0-1} as a function of thickness for the as-received material

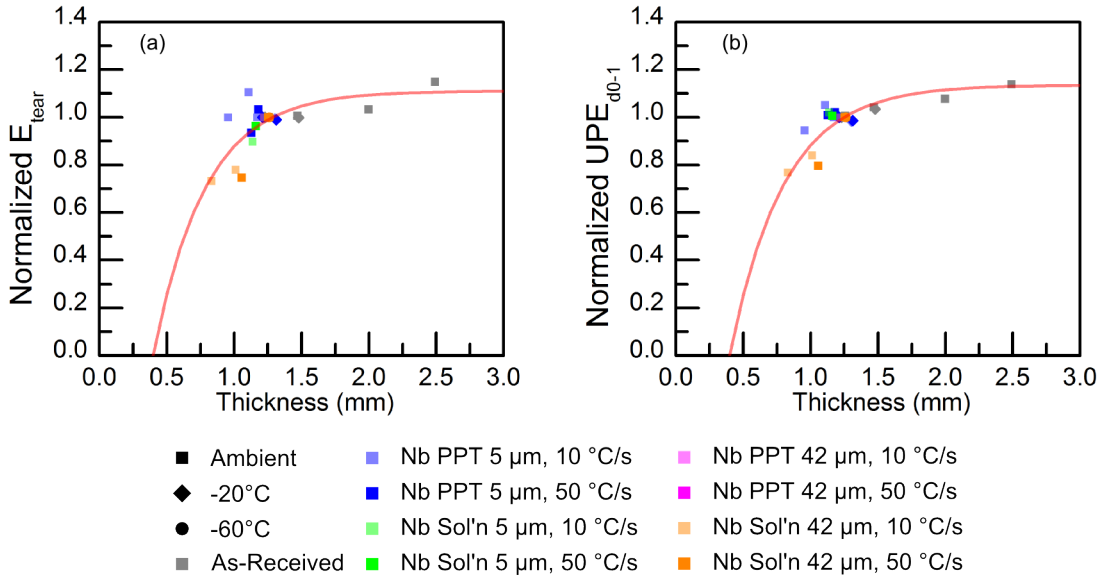

Figure 5.25: Fitting curve for (a) E_{tear} and (b) UPE_{d0-1} as a function of thickness.

no other conditions reaching similar values of E_{tear}. In the case of maximum UPE_{d0-1} values, it is seen this condition has still some of the highest values, but are now comparable to the conditions with prior austenite grain size of 5 µm cooled at 50 °C/s with Nb in precipitates and with Nb in solution which are ferritic and mixed ferrite/bainite microstructures respectively. The lowest value of E_{tear} are seen to be the condition with a prior austenite grain size of 5 µm with Nb in precipitates cooled at a rate of 10 °C/s which is a ferritic microstructure. The lowest value of UPE_{d0-1} the condition with a prior austenite grain size of 42 µm with Nb in precipitates cooled at 10 °C/s which

is a microstructure that is primarily upper bainite. Table 5.2 summarizes measured Kahn tear testing properties including the uncorrected and corrected E_{tear} and UPE_{d0-1} values.

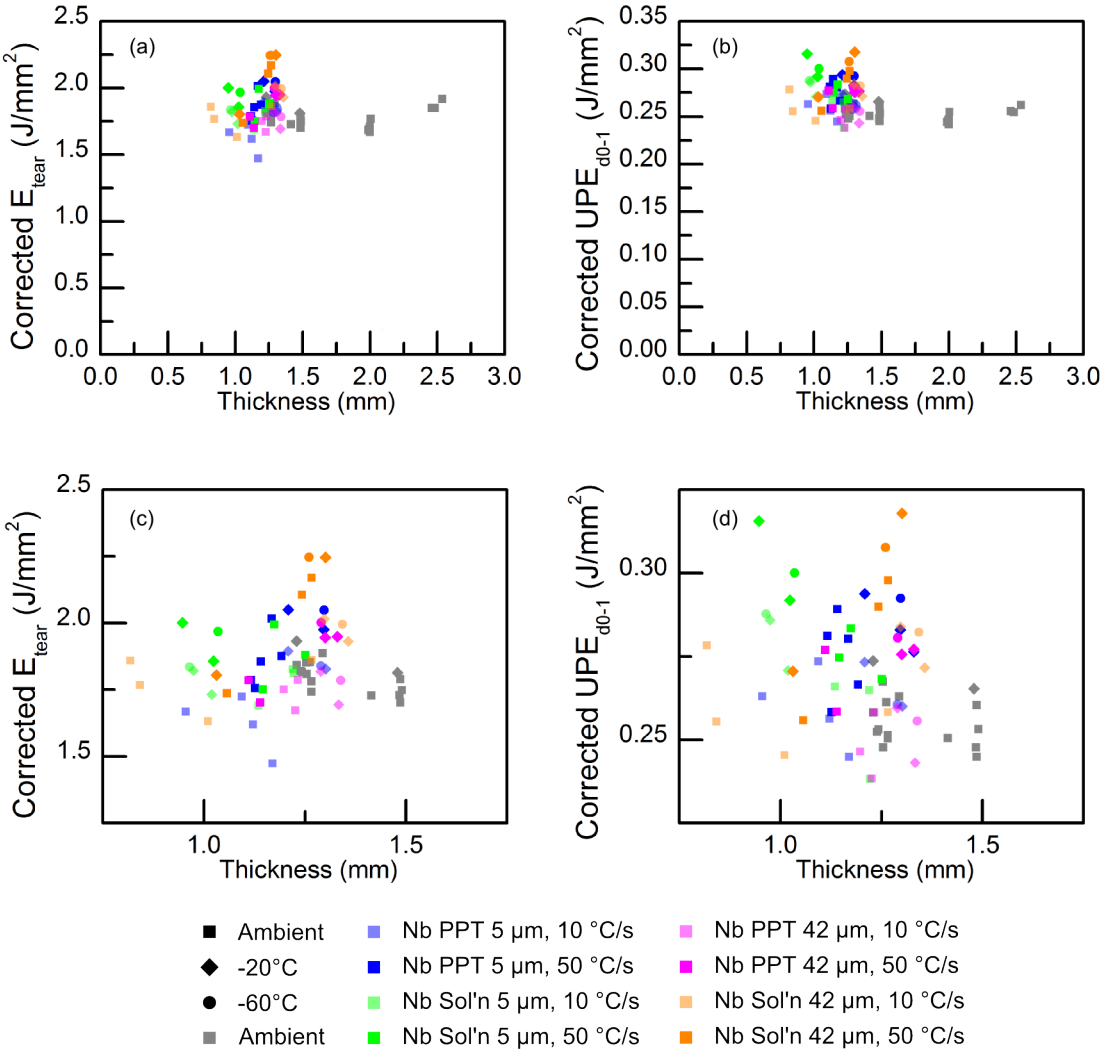

Figure 5.26: (a) Corrected E_{tear} and (b) corrected UPE_{d0-1} as a function of thickness, expanded to view the thermally treated conditions of both respectively in (c) and (d).

Table 5.2: Kahn tear test properties

Type	Temperature	σ_{Tear} (MPa)	UPE_{d0-1} (J/mm^2)	Corrected UPE_{d0-1} (J/mm^2)	E_{tear} (J/mm^2)	Corrected E_{tear} (J/mm^2)	Number of tests
As-Received	Ambient	1203	0.256	0.256	1.80	1.82	9
	-20 °C	1251	0.271	0.274	1.81	1.74	2
	-60 °C						
Nb in precipitates, 5 µm @ 10 °C/s Ferrite	Ambient	1080	0.241	0.259	1.49	1.62	3
	-20 °C	1156	0.267	0.267	1.84	1.86	2
	-60 °C	1203	0.264	0.261	1.84	1.84	1
Nb in precipitates, 5 µm @ 50 °C/s Ferrite	Ambient	1219	0.264	0.275	1.77	1.86	5
	-20 °C	1261	0.286	0.284	1.98	1.99	3
	-60 °C	1314	0.297	0.292	2.05	2.05	1
Nb in solution, 5 µm @ 10 °C/s Mixed Ferrite/Bainite	Ambient	1171	0.250	0.256	1.72	1.78	3
	-20 °C	1135	0.245	0.278	1.55	1.78	2
	-60 °C	1197	0.247	0.288	1.57	1.84	1
Nb in solution, 5 µm @ 50 °C/s Mixed Ferrite/Bainite	Ambient	1245	0.269	0.275	1.81	1.87	3
	-20 °C	1275	0.264	0.304	1.67	1.93	2
	-60 °C	1309	0.271	0.300	1.77	1.97	1
Nb in precipitates, 42 µm @ 10 °C/s Upper Bainite	Ambient	1115	0.245	0.248	1.70	1.74	3
	-20 °C	1151	0.256	0.251	1.77	1.76	2
	-60 °C	1181	0.262	0.256	1.81	1.78	1
Nb in precipitates, 42 µm @ 50 °C/s Upper Bainite	Ambient	1244	0.254	0.268	1.64	1.74	2
	-20 °C	1278	0.282	0.276	1.96	1.95	2
	-60 °C	1313	0.284	0.281	2.00	2.00	1
Nb in solution, 42 µm @ 10 °C/s Lower Bainite	Ambient	1189	0.219	0.259	1.50	1.78	4
	-20 °C	1311	0.288	0.278	1.99	1.97	2
	-60 °C	1354	0.290	0.282	2.02	2.00	1
Nb in solution, 42 µm @ 50 °C/s Lower Bainite	Ambient	1386	0.274	0.281	1.94	2.00	3
	-20 °C	1442	0.283	0.294	1.93	2.03	2
	-60 °C	1511	0.308	0.308	2.23	2.25	1

5.6 Fractography Results

Fracture surfaces of samples after tensile and Kahn testing were investigated using SEM. The fracture surface as examined at low magnifications for tensile and Kahn specimens were discussed in previous sections (i.e. see Figures 5.15 and 5.23). These figures were examples of the primarily ductile fracture surface seen at low magnification in all cases for both tensile and Kahn tests. Figure 5.27 and 5.28 show high magnification micrographs for several exemplary testing conditions and testing temperatures for the comparison of tensile to Kahn fracture surfaces. From these figures it can be seen that for a given microstructure and testing temperature the fracture surface between tensile tests and Kahn tests showed very similar fracture surfaces. For simplicity then, tensile fracture surfaces will be used here to compare fracture across conditions except where there is no valid tensile test for that condition wherein the Kahn fracture surface image is used instead.

At higher magnifications the void structure of the fracture surface is revealed. Figure 5.29 shows high magnification of the as-received material. What is seen in this figure is that the void size remains comparable at all temperatures tested. Figures 5.30 and 5.31 show the high magnification micrographs of the conditions with a prior austenite grain size of 5 μm with Nb precipitated and cooling rates of 10 °C/s and 50 °C/s respectively. These micrographs show that these conditions which are ferritic microstructure have comparable void sizes with only the occasional appearance moderately sized voids when compared to the as-received material which is also a ferritic microstructure. Fracture surfaces with the conditions with a prior austenite grain size of 42

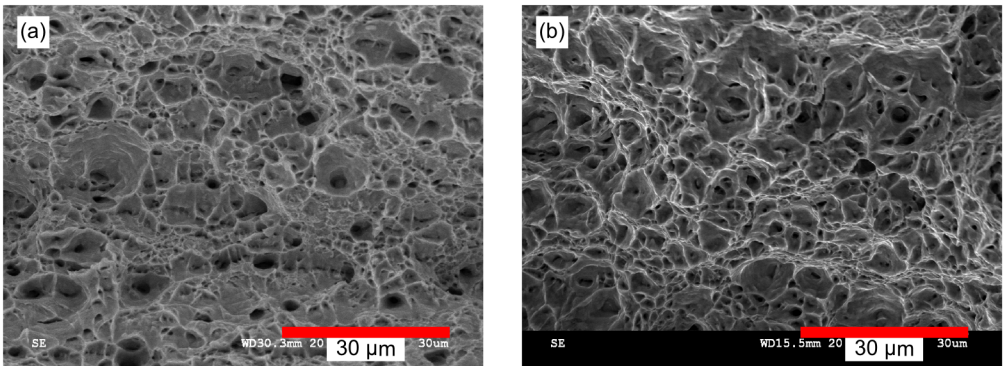

Figure 5.27: (a) Tensile and (b) Kahn fracture surfaces as examined by SEM for the condition with a prior austenite grain size of 5 μm with Nb in precipitates cooled at 10 °C/s tested at ambient temperatures.

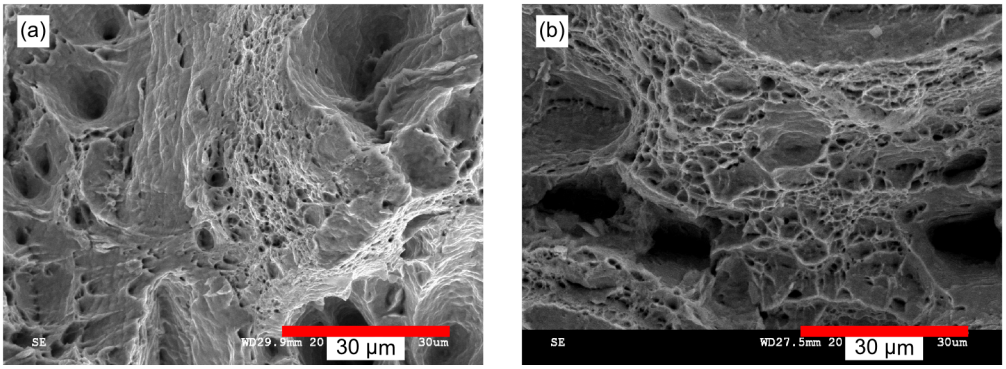

Figure 5.28: (a) Tensile and (b) Kahn fracture surfaces as examined by SEM for the condition with a prior austenite grain size of 42 µm with Nb in solution cooled at 50 °C/s tested at -20 °C.

µm and Nb in solution with cooling rates of 10 °C/s and 50 °C/s are shown in Figures 5.32 and 5.33 respectfully. What is seen from these images is that the void size remains fairly similar to the conditions with a prior austenite grain size of 5 µm with Nb in precipitates with mainly smaller voids and occasional moderately sized voids.

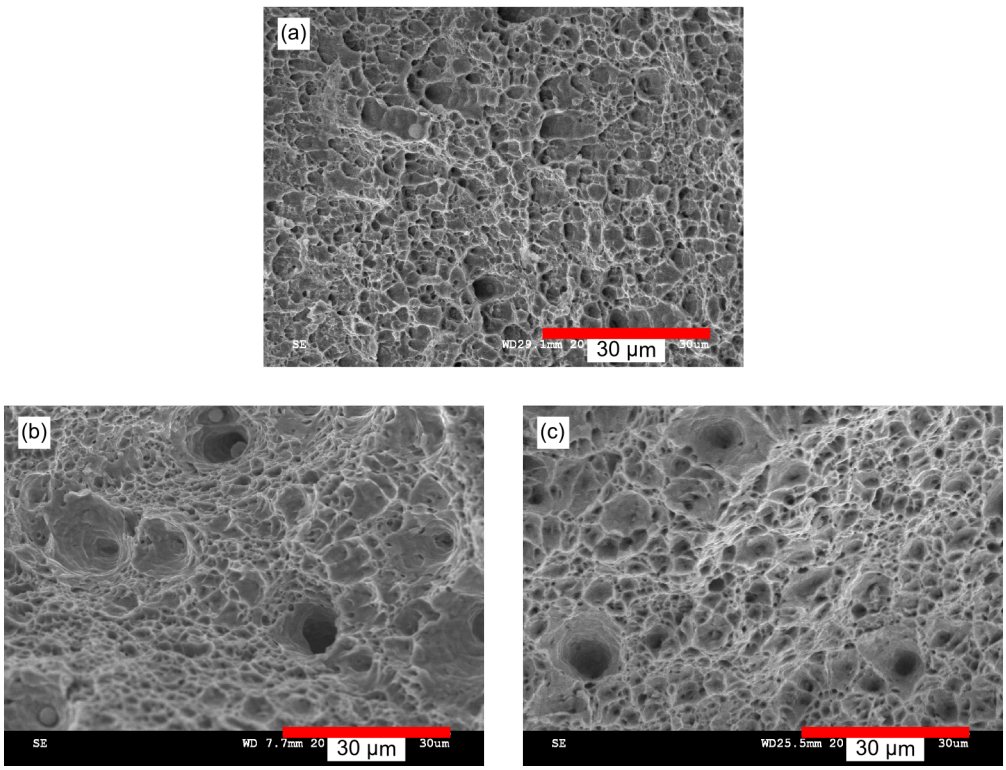

Figure 5.29: As-received fracture surfaces for (a) tensile test at ambient temperature (b) Kahn test at -20 °C (c) tensile test at -60 °C

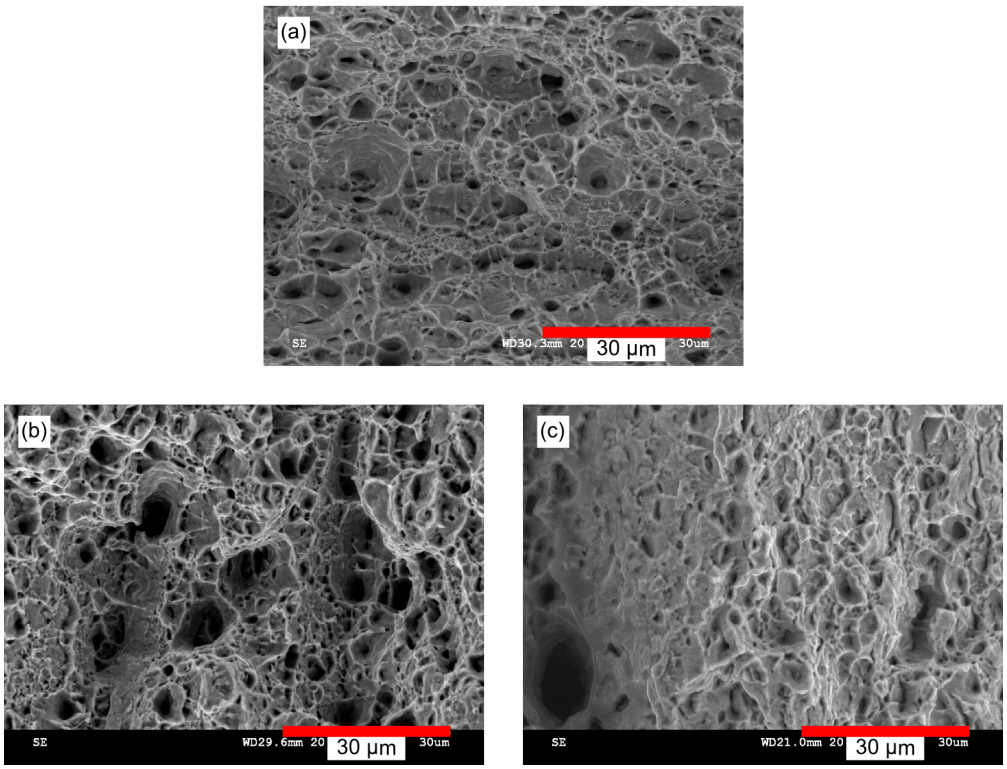

Figure 5.30: Condition with a prior austenite grain size of 5 µm, Nb in precipitates cooled at 10 °C/s fracture surfaces for (a) tensile test at ambient temperature (b) tensile test at -20 °C (c) tensile test at -60 °C

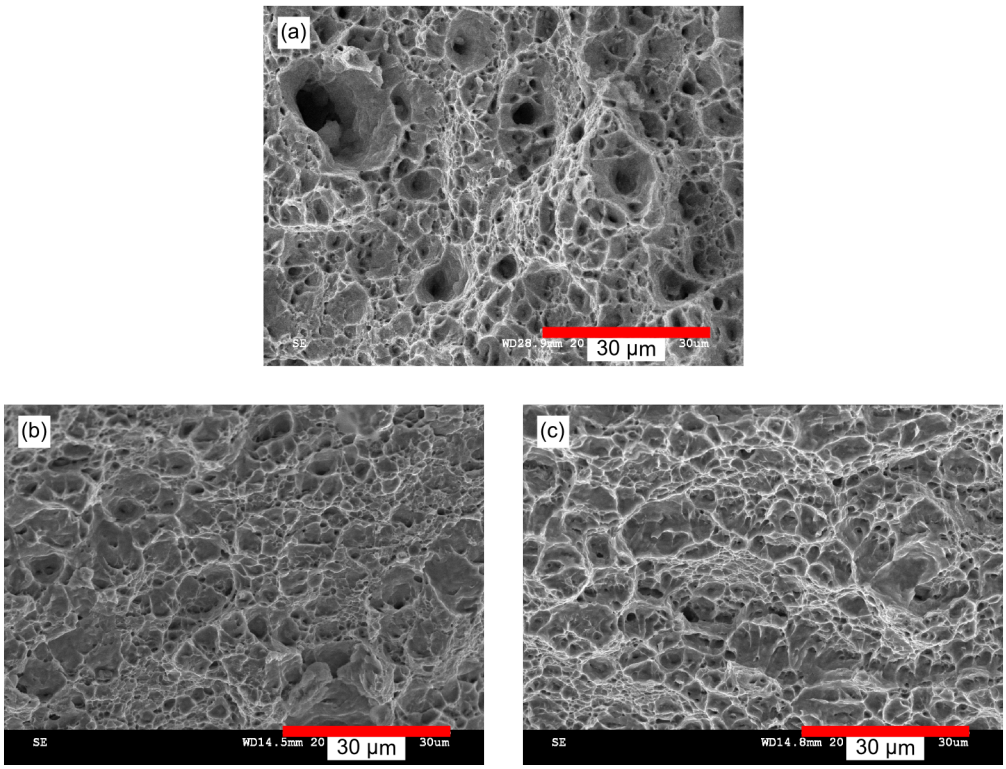

Figure 5.31: Condition with a prior austenite grain size of 5 µm, Nb in precipitates cooled at 50 °C/s fracture surfaces for (a) tensile test at ambient temperature (b) Kahn test at -20 °C (c) Kahn test at -60 °C

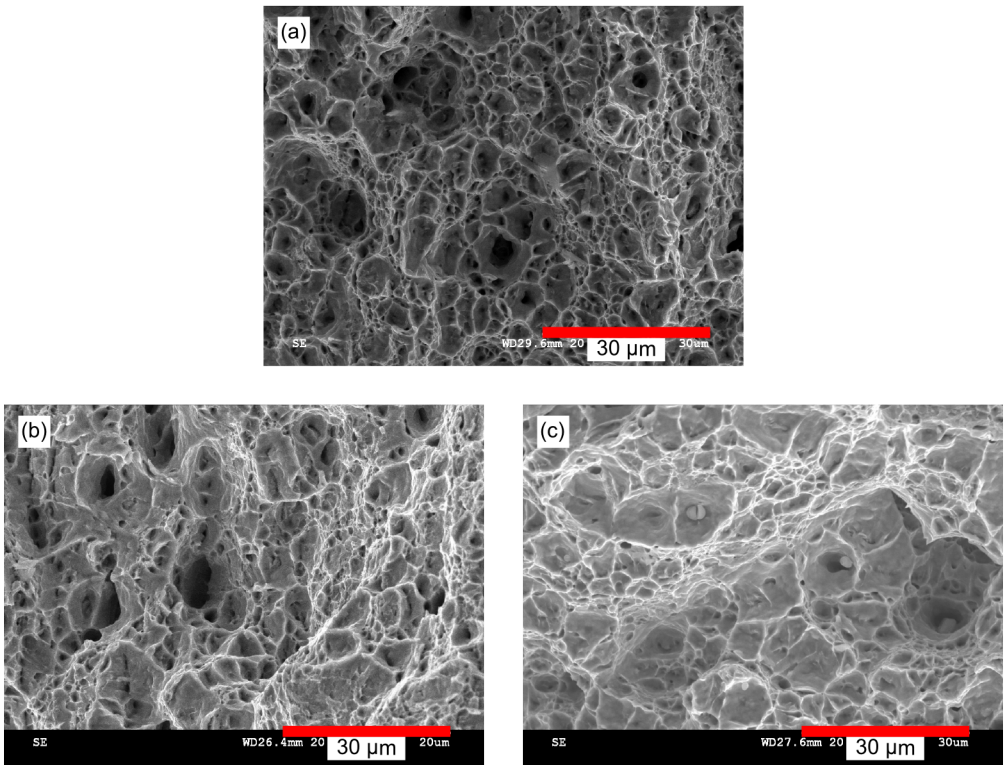

Figure 5.32: Condition with a prior austenite grain size of 5 µm, Nb in solution cooled at 10 °C/s fracture surfaces for (a) tensile test at ambient temperature (b) tensile test at -20 °C (c) Kahn test at -60 °C

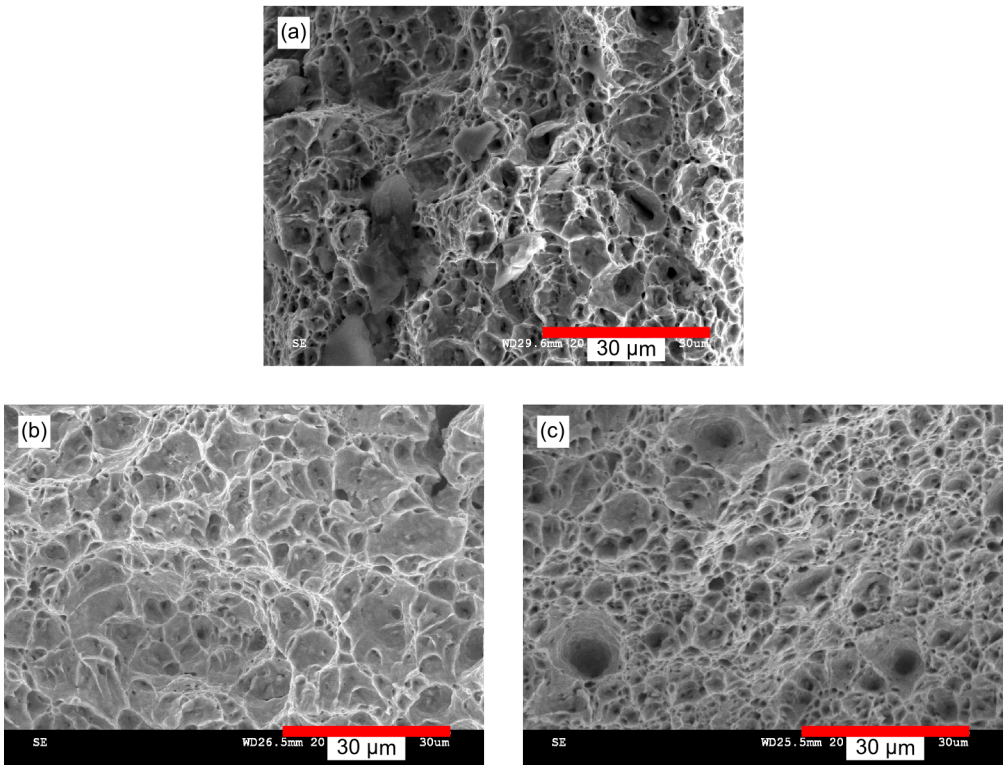

Figure 5.33: Condition with a prior austenite grain size of 5 µm, Nb in solution cooled at 50 °C/s fracture surfaces for (a) tensile test at ambient temperature (b) tensile test at -20 °C (c) tensile test at -60 °C

Figures 5.34 and 5.35 show high magnification micrographs of conditions with a prior grain size of 42 μm and Nb in precipitates with cooling rates of 10 °C/s and 50 °C/s respectively. These conditions, which are primarily upper bainitic microstructures, have both smaller voids like in the previous conditions, but now large void structures are seen often across the fracture surface. The high magnification examination of conditions with a prior austenite grain size of 42 μm and Nb in solution with cooling rates of 10 °C/s and 50 °C/s are shown in Figures 5.36 and 5.37 respectively. These figures show that these conditions which are primarily lower bainite microstructure give a fracture surface with some smaller voids and a number of large voids. These lower bainitic fracture surfaces show similarities to the fracture surfaces seen in the upper bainitic cases. The large voids in the condition with a prior austenite grain size of 42 μm with Nb in solution cooled at 50 °C/s are seen to be a little larger than those of the other conditions with a prior austenite grain size of 42 μm.

All samples showed an amount of small voids on their fracture surfaces. For the ferritic and ferrite/bainite mixture microstructures that were formed with a prior austenite grain size of 5 μm the small voids were seen to dominate the fracture surface. In the upper and lower bainite specimens, which are specimens formed with with a prior austenite grain size of 42 μm, large voids are seen often across the fracture surface. In all conditions, the testing temperature was seen to have little effect on the size of the voids. Table 5.3 summarizes all observations made of the fracture surfaces.

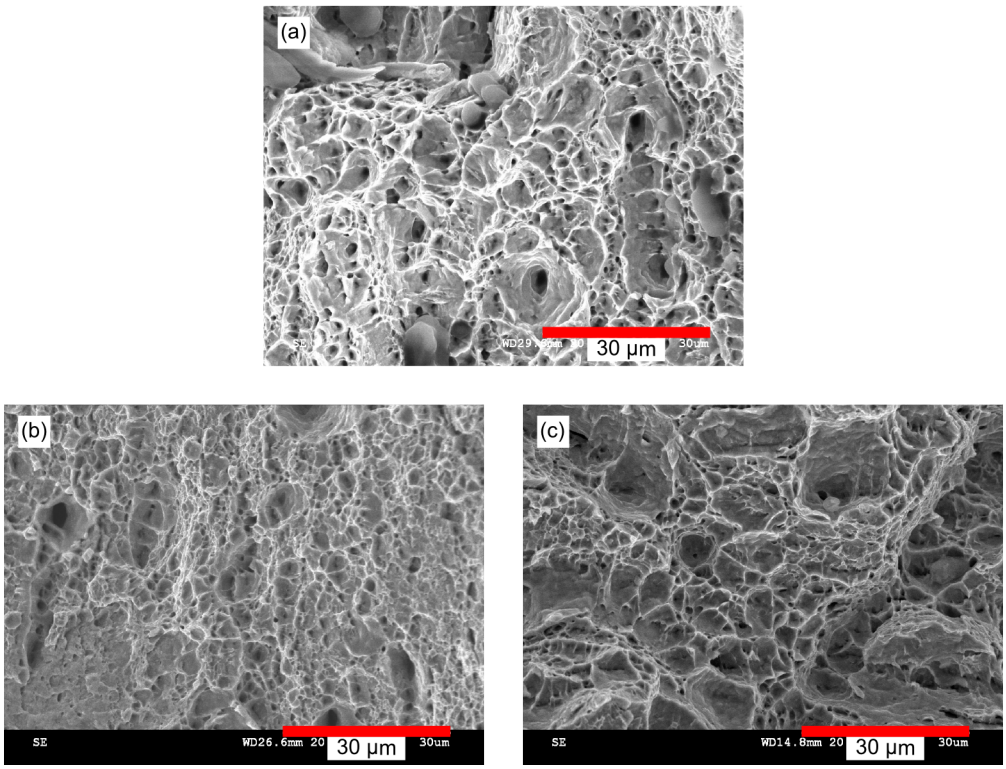

Figure 5.34: Condition with a prior austenite grain size of 42 µm, Nb in precipitates cooled at 10 °C/s fracture surfaces for (a) tensile test at ambient temperature (b) tensile test at -20 °C (c) tensile test at -60 °C

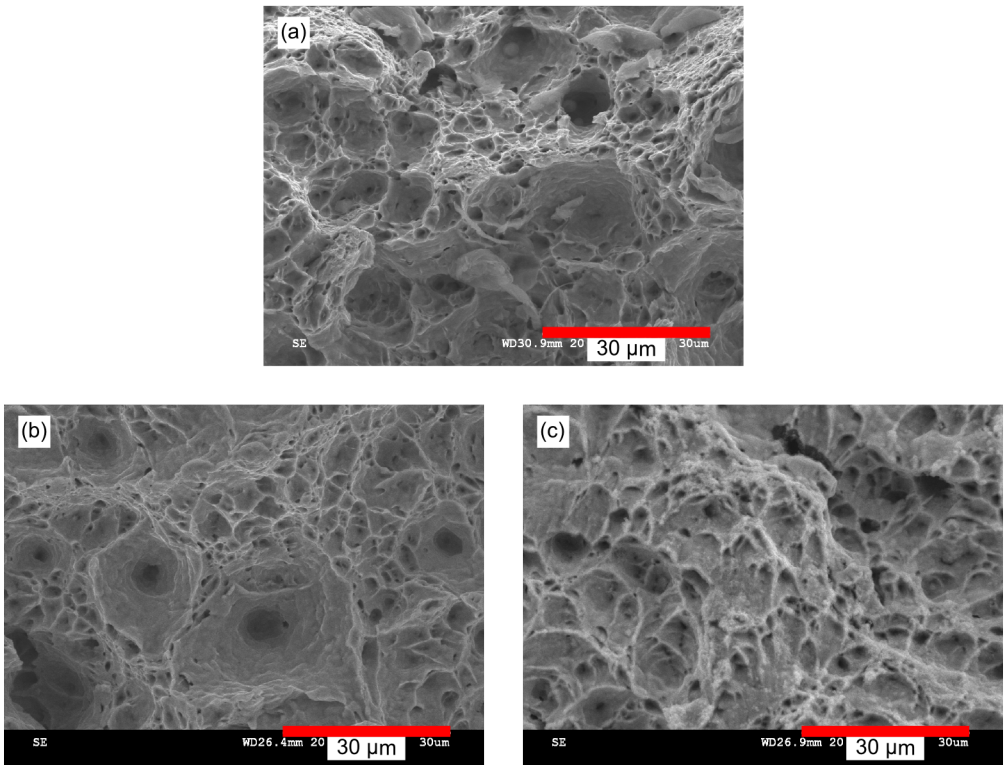

Figure 5.35: Condition with a prior austenite grain size of 42 µm, Nb in precipitates cooled at 50 °C/s fracture surfaces for (a) tensile test at ambient temperature (b) Kahn test at -20 °C (c) Kahn test at -60 °C

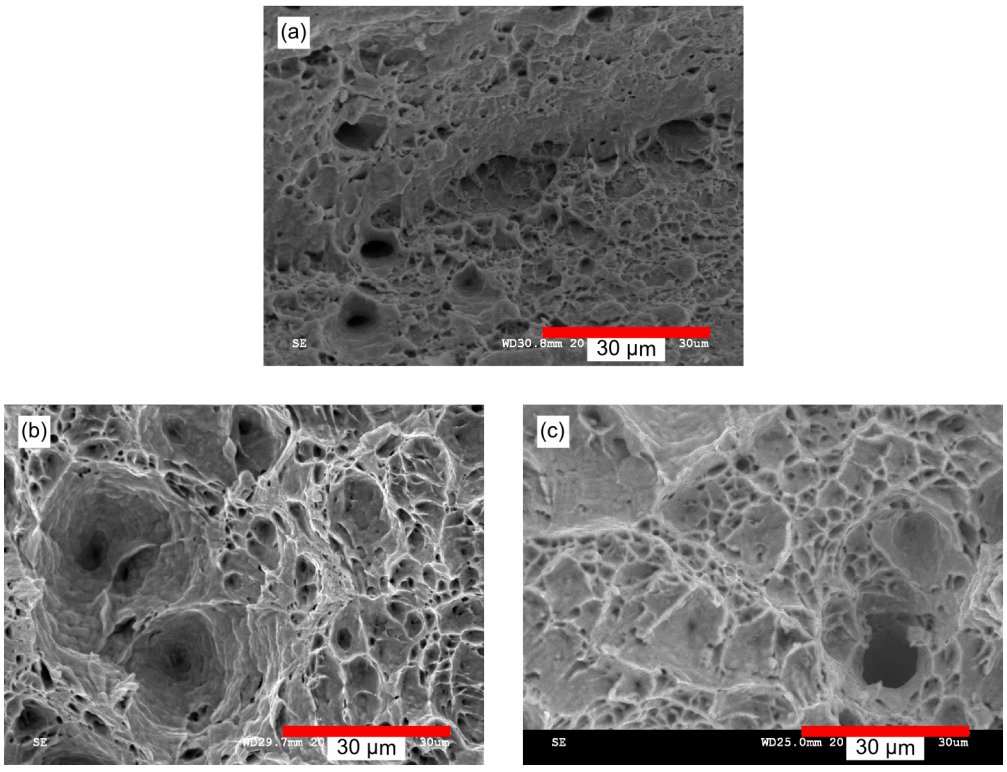

Figure 5.36: Condition with a prior austenite grain size of 42 µm, Nb in solution cooled at 10 °C/s fracture surfaces for (a) tensile test at ambient temperature (b) tensile test at -20 °C (c) Kahn test at -60 °C

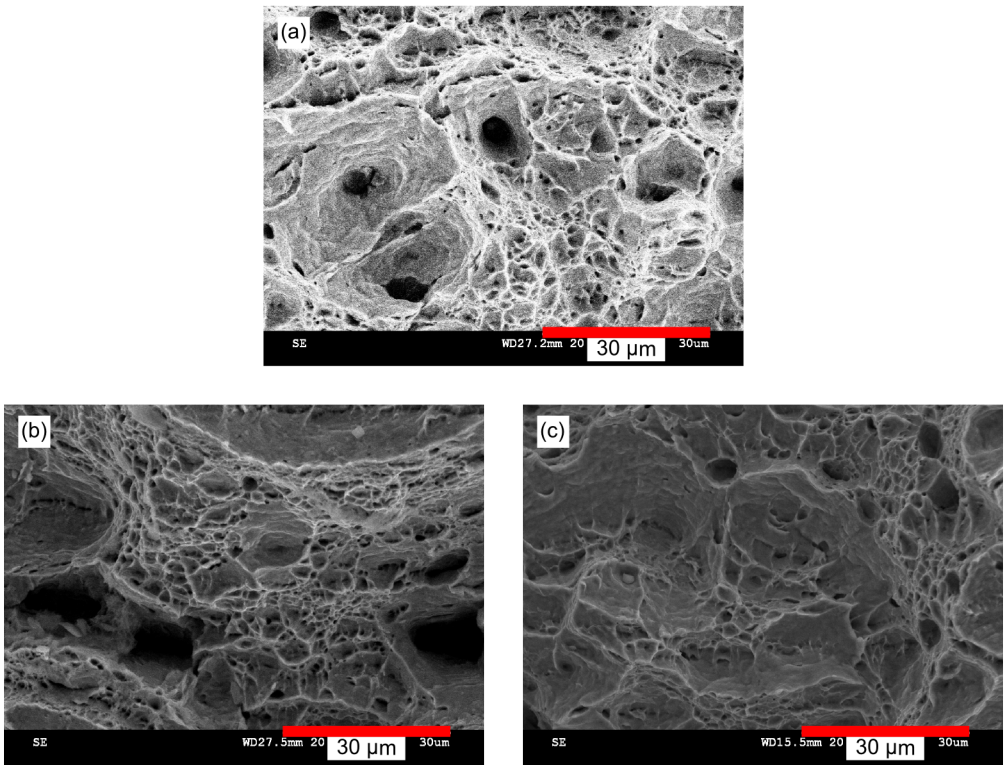

Figure 5.37: Condition with a prior austenite grain size of 42 µm, Nb in solution cooled at 50 °C/s fracture surfaces for (a) tensile test at ambient temperature (b) tensile test at -20 °C (c) tensile test at -60 °C

Table 5.3: Fracture surface observations

Type	Temperature	Tensile Fracture Surface	Kahn Fracture Surface
Nb in precipitates, 5 μm @ 10 °C/s	Ambient	Moderate sized voids (5-10 μm)	Small to moderate sized voids throughout (5-10 μm)
Ferrite	-20 °C	Smaller and moderate sized voids	Mainly small voids, some moderate voids
	-60 °C	Smaller and moderate sized voids	Small and moderate voids throughout
Nb in precipitates, 5 μm @ 50 °C/s	Ambient	Mainly small voids	Large voids near notch, small voids elsewhere
Ferrite	-20 °C		Mainly small voids, some moderate voids
	-60 °C		Small and moderate voids throughout
Nb in solution, 5 μm @ 10 °C/s	Ambient	Mainly small voids with some moderate and large voids	Small and moderate sized voids
Mixed Ferrite/Bainite	-20 °C	Mainly small voids and some moderate voids	Mainly small voids, some moderate voids
	-60 °C		Moderate size voids throughout
Nb in solution, 5 μm @ 50 °C/s	Ambient	Mainly small voids	Small and moderate sized voids
Mixed Ferrite/Bainite	-20 °C	Mainly small voids with some moderate voids	Mainly small voids, some moderate voids
	-60 °C	Smaller sized voids and deep cracks	Small voids and moderate voids, some small cracks or ridges parallel to crack propagation direction
Nb, in precipitates, 42 μm @ 10 °C/S	Ambient	Mainly smaller voids	Moderate sized voids and some large voids throughout
Upper Bainite	-20 °C	Mainly small voids with a few larger voids	Small and moderate to large voids throughout
	-60 °C	Smaller and moderate voids, and some deep cracks	Large voids throughout
Nb, in precipitates, 42 μm @ 50 °C/S	Ambient	Small voids with plenty of larger voids	Large voids near notch, moderate voids elsewhere
Upper Bainite	-20 °C	Small voids and some larger voids	Very large voids near notch, large voids further in
	-60 °C	Smaller voids and some cracks	Large voids throughout
Nb in solution, 42 μm @ 10 °C/s	Ambient	Mainly small voids with some large voids	Large voids throughout
Lower Bainite	-20 °C	Small voids with some large voids	Large voids and a few very large voids
	-60 °C	Small and large voids with numerous cracks	Large voids near notch, some small cracks further in
Nb in solution, 42 μm @ 50 °C/s	Ambient	Some small voids and numerous large voids	Very large voids throughout
Lower Bainite	-20 °C		Very large voids near notch, large voids further in
	-60 °C		Large and very large voids near notch, ridges and cracks parallel to crack propagation direction further in

Void diameter sizing is approximated as follows: small (1-5 μm), moderate (5-10 μm), large (10-15 μm), and very large (15-20 μm).

CHAPTER 6

Discussion

6.1 Introduction

From the test results, there were many interesting findings which will be discussed in this chapter with particular attention given to the relation between microstructure and observed properties. Where appropriate, analysis is extended further to provide insights. Also of importance to the discussion is examining the applicability of test and analysis methods used here so as to be clear about the potential and limitations. As such, the most crucial aspect of testing is first addressed, i.e. the ability to consistently create isolated bulk microstructures for testing that are of relevance to real observed HAZ microstructures.

6.2 Weld Trials and Gleeble Heat Treatments

Weld trials provided the heating and cooling rate data that guided Gleeble heat treatments. Considering this, the HAZ microstructures developed in weld trials can be compared to the microstructures generated through Gleeble heat treatments to determine if these heat treated microstructures are of relevance. Figures 6.1, 6.2, and 6.3 shows typical microstructures seen in the HAZ from the trials along with microstructures from Gleeble heat treatment that appear similar from metallographic comparison. It is seen that the HAZ microstructures in close proximity to the fusion line (i.e. microstructures in the CGHAZ and FGHAZ) largely show features (i.e. constituents, coarseness, and morphology) comparable to those produced by the Gleeble heat treatments. While the purpose of

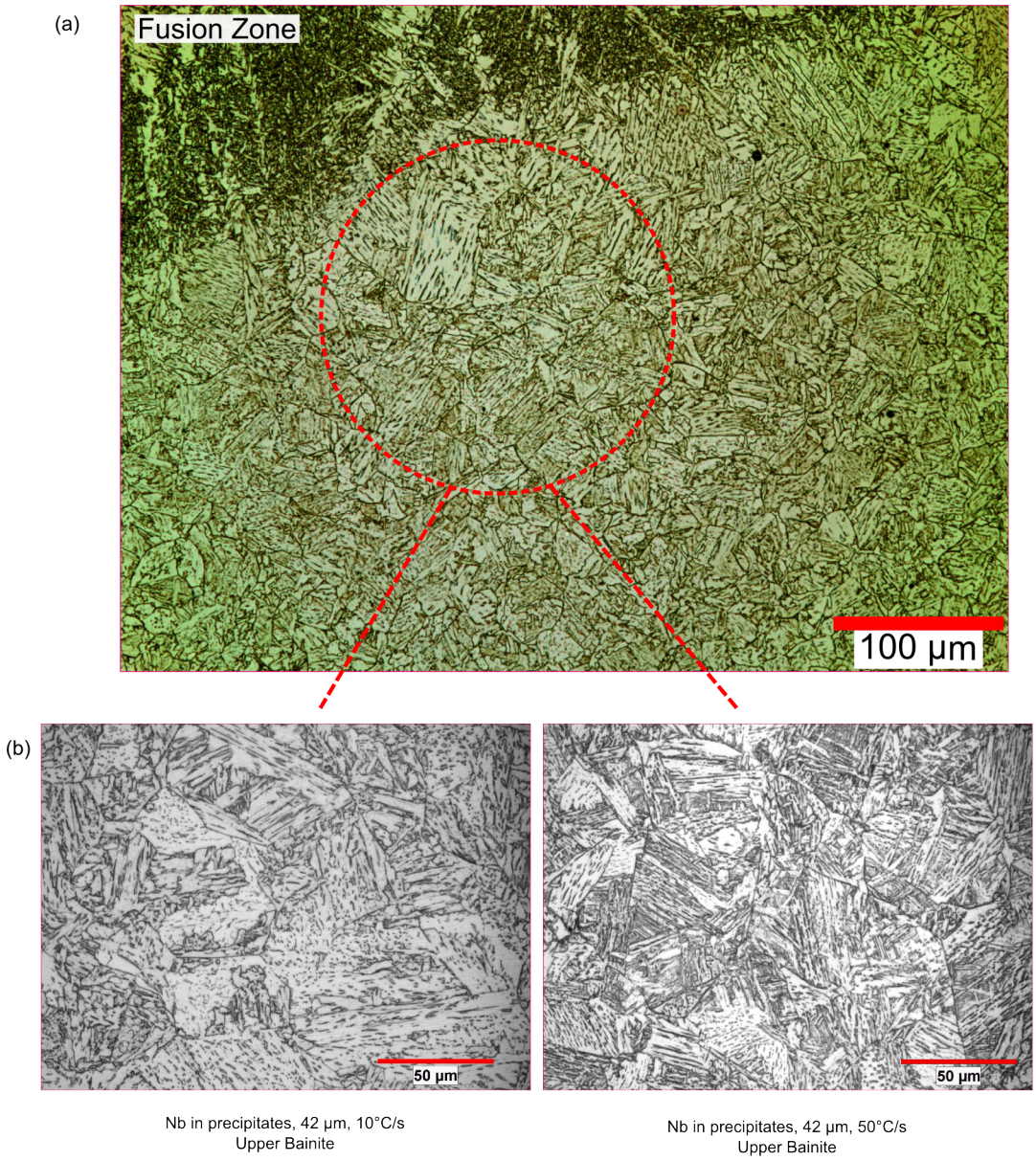

Figure 6.1: (a) Weld trial HAZ microstructure of a 70 mm (2.75”) torch spacing compared to (b) Gleeble heat treated microstructures.

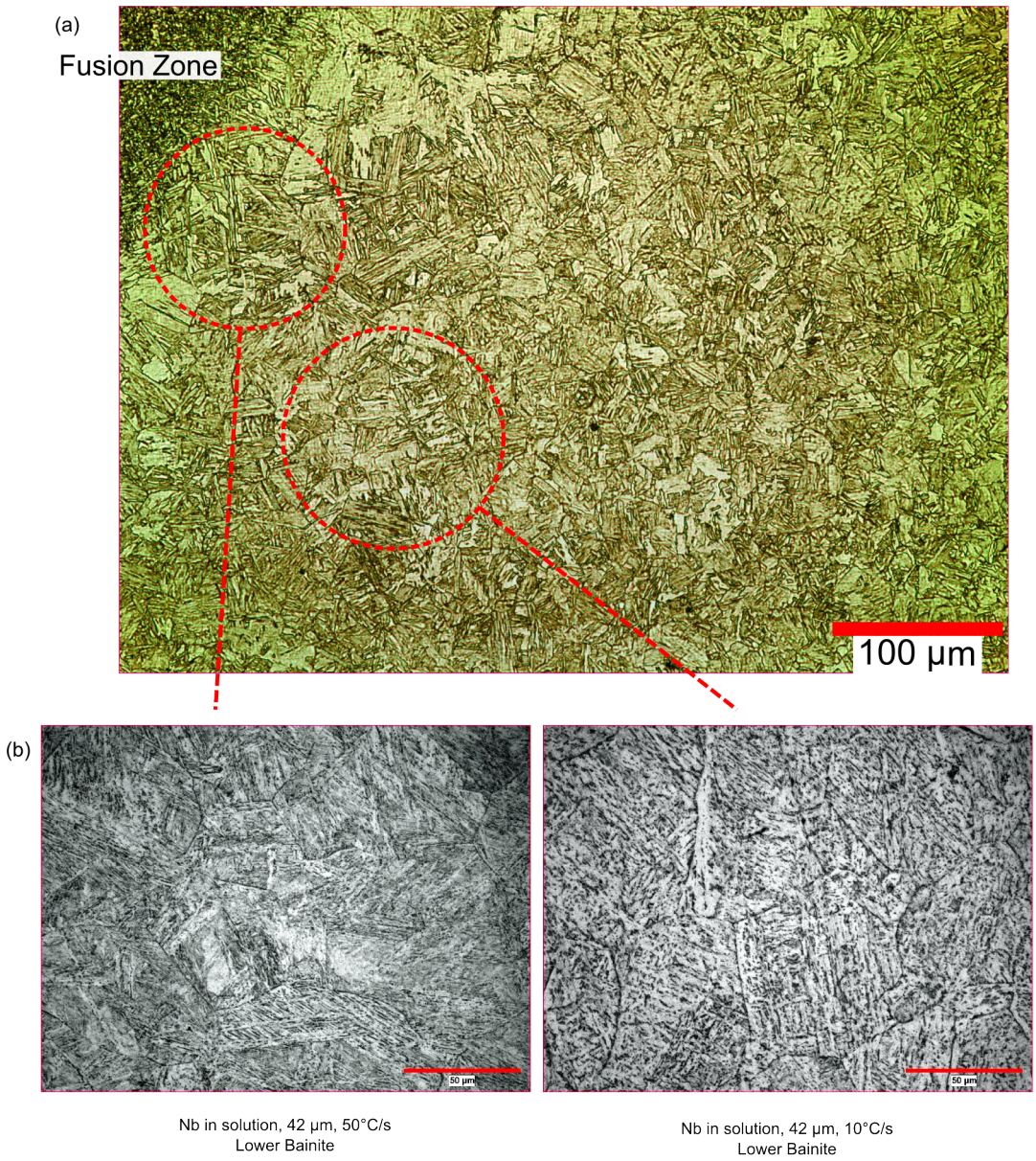

Figure 6.2: (a) Weld trial HAZ microstructure of a single torch sample compared to (b) Gleeble heat treated microstructures.

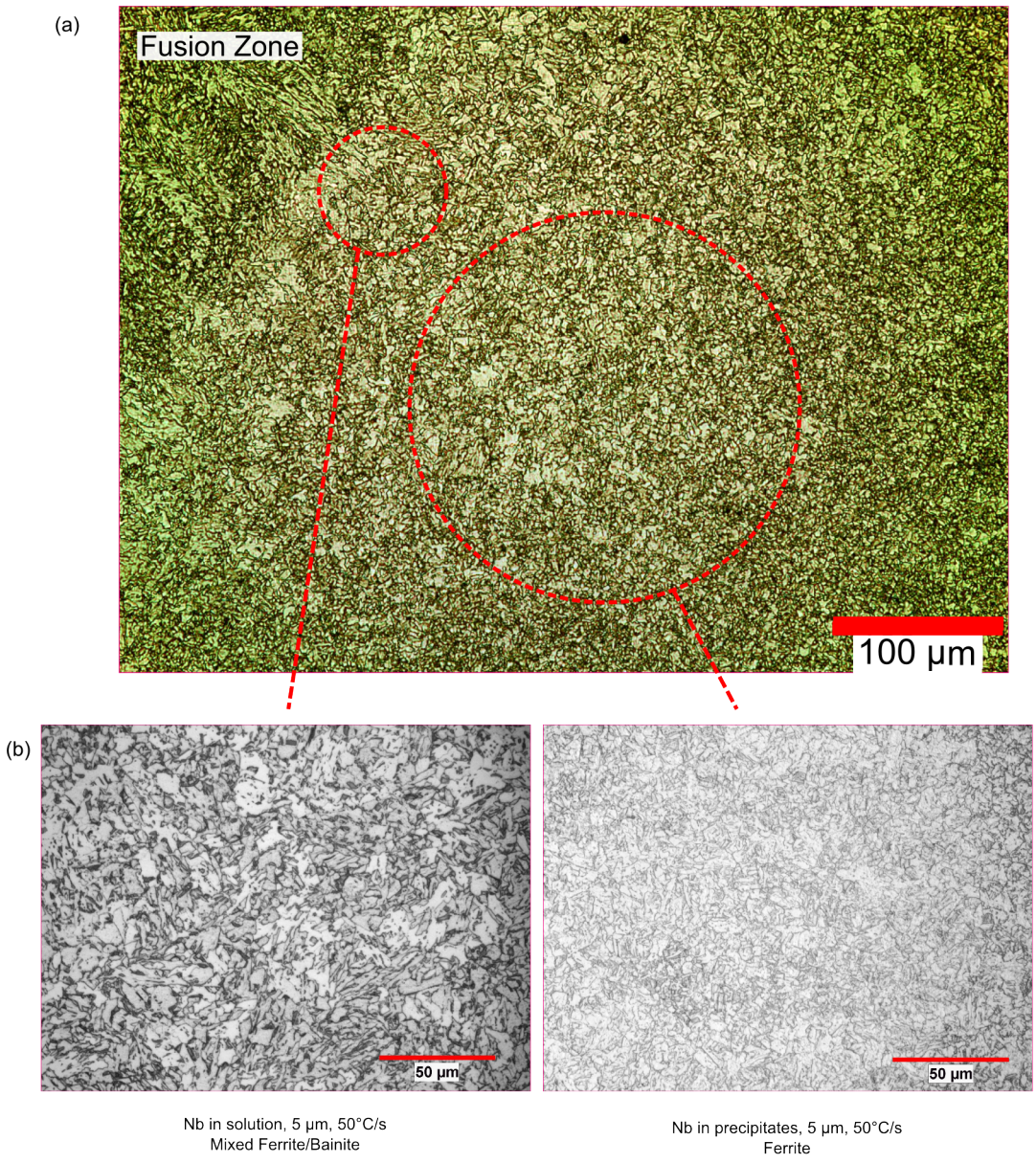

Figure 6.3: (a) Weld trial HAZ microstructure of a different single torch sample compared to (b) Gleeble heat treated microstructures.

this study is not to reproduce exactly the individual microstructures in the HAZ using Gleeble heat treatments, it is seen that the microstructures that have been produced are of relevance to the HAZ. Furthermore, it is seen in these figures that Gleeble heat treatments that would be expected to only have relevancy further from the fusion line in some cases produced microstructures that are in fact showing similarities to the microstructure observed close to the fusion line. While it is not clear why this is the case, it is probable that subsequent weld passes have affected the final microstructure in these positions, making a straightforward relation between distance from the fusion line and the Gleeble heat treatment not possible. Plausible scenarios for the observed thermal history in each case will follow. In Figure 6.1, the heating cycle in the weld may not have been enough to dissolve all of the Nb containing particles in the CGHAZ prior to cooling, resulting in a microstructure that is similar to the shown thermal cycles with 42 μm prior austenite grain size and Nb in precipitates. In Figure 6.2, the single torch weld observed close to the fusion zone is similar to the Gleeble heat treatment with Nb in solution with a large prior austenite grain size. The weld microstructure in Figure 6.3 shows fine features in the area close to the fusion zone. It is likely that in this case, the microstructure was affected by a subsequent pass of the weld torch placing the region into the FGHAZ which is well represented by the observed Gleeble heat treatments that use a small prior austenite grain size. By design, the Gleeble heat treatments did not attempt to encompass all thermal cycles and their resulting microstructures. For example, microstructures in the ICCGHAZ, the zone noted in literature [61–64,68] to be a potential site of low toughness in the HAZ, are not investigated in this study due to this microstructure being only a small portion of the HAZ, and due to constraints of time and material.

It was seen in Figure 5.5 (d) that there was some spread in peak temperatures for Gleeble heat treated samples with a prior austenite grain size of 42 μm grain size (peak temperature of 1350 °C). To assess the significance of this variation on prior austenite grain size, the microstructure prediction model of Maalekian et al. [148] was used on tests giving the lowest peak temperature (1320 °C), close to the aim peak temperature (1350 °C), and the highest peak temperature (1380 °C). For the thermal cycle giving the lowest peak temperature, the model predicts that the austenite grain size would be 39 μm which is close to the goal of reaching a 42 μm austenite grain size. For the thermal cycle resulting in the highest peak temperature, the model predicts that the austenite grain size should be 50 μm. This is noticeably higher than the aim of 42 μm. Austenite grain size

influences the transformation start temperatures; an increase in the austenite grain size correlates with a decrease of the transformation temperature, which is to say that it promotes lower bainitic and even martensitic transformation products. From the model, the predicted microstructure for the sample with the significantly higher grain size remains fully lower bainitic with a small amount of martensite, which is the same microstructure constituents observed from specimens closer to the aim peak temperature of 1350 °C. The austenite grain size also influences the packet size of the lower bainite laths. While this packet size could affect the cleavage fracture toughness, it is not expected to affect the tensile properties or ductile fracture properties. Thus the difference between samples with 39 μm and 50 μm austenite grain sizes are not significant in the context of this work.

6.3 Kocks-Mecking Analysis

Having shown that there is confidence in the Gleeble heat treatments to generate microstructures of relevance to the HAZ, the rest of the discussion focuses on the results of mechanical testing. This discussion will first examine the results from tensile testing, and then move on to the relation between microstructure and tensile properties in the following section.

The tensile testing results in Section 5.4 showed some interesting behaviour. Figure 6.4 shows the schematic of one test condition at two temperatures that typifies the stress-strain curves as observed from the thermally treated specimens. It is seen that the elastic-plastic transition for these stress-strain curves is very rounded, which is to say that there is no distinct yield point observed and that yielding occurs over a range of strain. This makes determination of the yield strength difficult, which lead to the selection of using the 0.5% offset yield strength over the typical 0.2% as this gave more consistent values across tests of the same test conditions. The strict use of an offset yield strength to characterize the yield point however ignores the details related to micro-yielding.

After yielding begins, work-hardening occurs and is measured up to the Considère condition (i.e. start of necking), which was reached in all test conditions as typified by the results shown in Figure 6.4. Work hardening is represented by the work hardening rate given by:

$$\theta = \frac{d\sigma}{d\varepsilon} \tag{6.1}$$

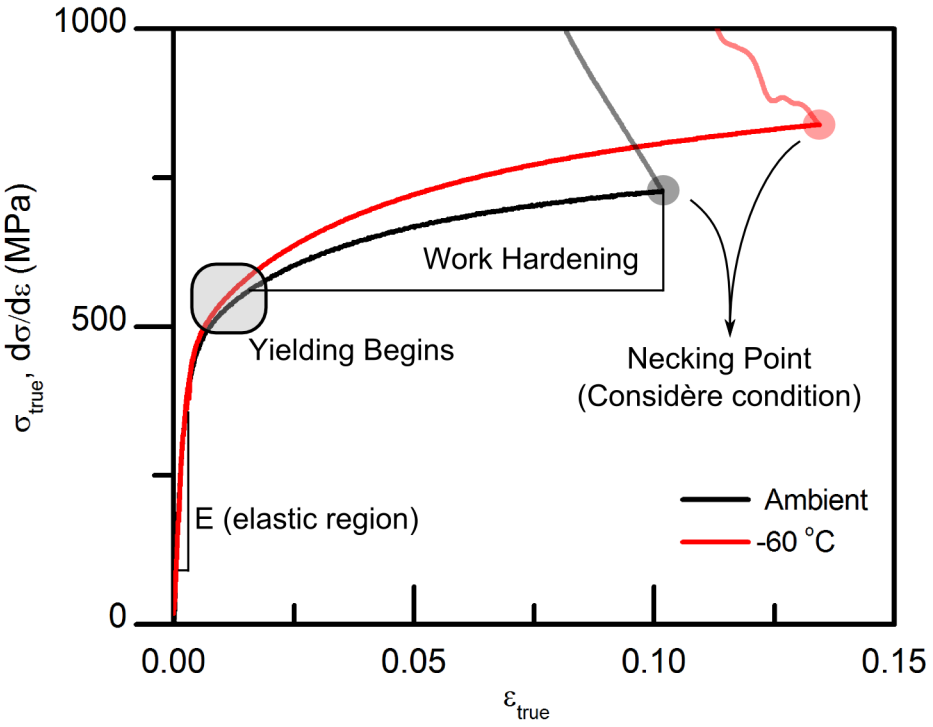

Figure 6.4: Example true stress-strain data from Nb in precipitates, 5 μm prior austenite grain size cooled at 10 °C/s at two different temperatures with labelling of notable properties.

with the Considère condition being defined as:

$$\frac{d\sigma}{d\varepsilon} = \sigma \tag{6.2}$$

After the Considère criteria is reached, the cross-sectional area in the neck changes from the initial value and to observe the work-hardening would require measurement of the changing cross-sectional area in the necked region. In this study, no such measurements were made and thus work-hardening can only be measured up to the point of necking, with the exception of the measurements made after the test and thus relating to the point of final fracture. The work-hardening behaviour in this study, typified in Figure 6.4, shows that as testing temperature decreases from ambient temperatures, greater work-hardening rates are observed, greater elongation at the Considère condition is observed, and greater stress at the Considère condition is observed. There are some exceptions to this work hardening behaviour which will be discussed shortly.

A more complete analysis of the work hardening behaviour follows the framework of Kocks-Mecking [112, 114, 149], plotting the work-hardening rate against stress and is shown schematically in Figure 6.5. From such a plot, various stages of a steel's deformation can be observed. As the stress first increases, the steel is within the linearly elastic region and θ should be equal to the Young's modulus of the material. With stress increasing further, the steel experiences the elastic-plastic transition and θ rapidly decreases. Following the elastic-plastic transition, stage III work hardening is seen with a constant (i.e. linear) decrease of θ with increasing stress, which is the stage of work hardening seen in the typical tensile test and is the most important for this investigation of work hardening behaviour. The stage IV low work hardening rate is important to high strains, which are observed in the plots of true stress-strain including the true fracture stress.

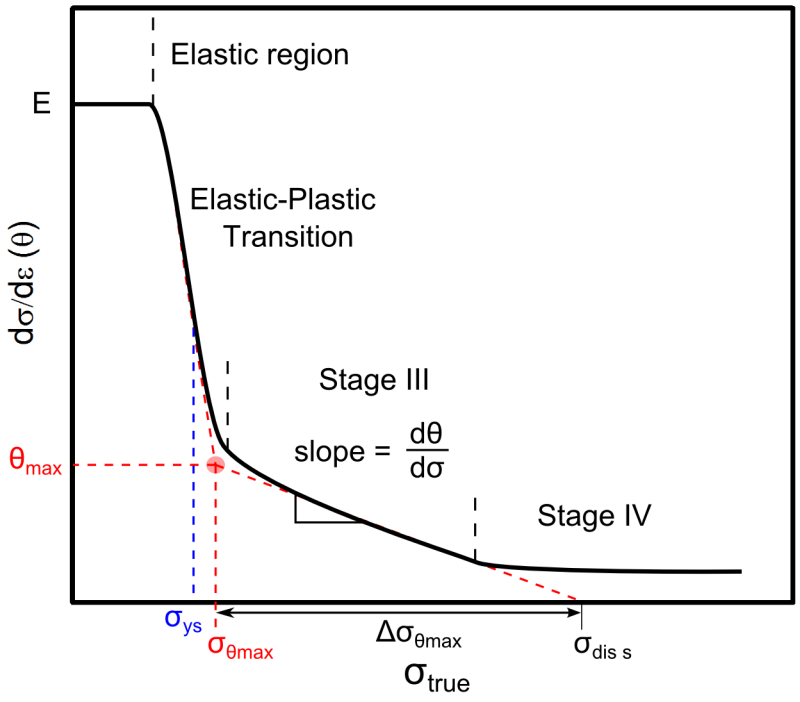

Figure 6.5: Schematic of the θ vs σ_{true} showing the definition of operational parameters.

The stage III deformation regime, with some reasonable assumptions, can give parameters with a physical basis. The strengthening contribution of work hardening was previously defined by:

$$\sigma_{dis} = \alpha M G b \rho^{1/2} \tag{6.3}$$

where the dislocation density, ρ, evolves according to:

$$\frac{d\rho}{d\varepsilon_p} = k_1\rho^{1/2} - k_2\rho \tag{6.4}$$

The theoretical dislocation hardening saturation stress, $\theta_{dis\ s}$, at which no further dislocation strengthening occurs via stage III mechanisms, can be seen in Figure 6.5, and calculated by:

$$\sigma_{dis\ s} = \frac{\alpha MGbk_1}{k_2} \tag{6.5}$$

The initial work hardening rate for dislocation contribution to flow stress is given by:

$$\theta_{dis\ 0} = \frac{\alpha MGbk_1}{2} \tag{6.6}$$

As the steel in this investigation does not have a clear yield point, it is useful to follow the work of Cheng et. al. [150]. Similar to Cheng's work, θ_{max} is defined by the intersection point between the linear extrapolation of the elastic-plastic transition region and of the stage III region on the θ versus σ_{true} graph as shown in Figure 6.5.

From the relations above, the physical basis of these parameters can be seen. θ_{max} is proportional to k_1 (the dislocation storage rate) according to equation 6.6, and thus can be used by direct comparison to examine this term. The dynamic recovery term of the work hardening equation, k_2, can be determined from the slope in stage III according to:

$$\frac{d\theta}{d\sigma} = -\frac{k_2}{2} \tag{6.7}$$

Importantly, k_1 represents an athermal term related to θ_{max} and k_2 represents a thermally dependent term related to $d\theta/d\sigma$. Consequently the value of $\Delta\sigma_{\theta max}$ (as shown in Figure 6.5) represents a combination of these terms. With these terms the effect of test temperature on work hardening can

be examined critically.

To give an example of the analysis from the current study, Figure 6.6 shows an example of the data from a single condition tested at the three testing temperatures. As it is not typical to see values plotted against stress it is helpful to recognize the trends between the more common stress-strain and θ-strain plots and θ-stress plots. At the start of the tests the hardening rate is equal to the elastic modulus, and drops from there as the material progresses into the plastic region. This effect is seen in both Figure 6.6 (b) and (c) which show hardening rate plotted against true strain and true stress respectively. The value in continuing the analysis becomes evident in Figure 6.6 (d). This plot of θ versus $\sigma - \sigma_{ys}$ reveals the θ_{max} and $d\theta/d\sigma$ at a glance which are in turn directly related to the k_1 and k_2 respectively.

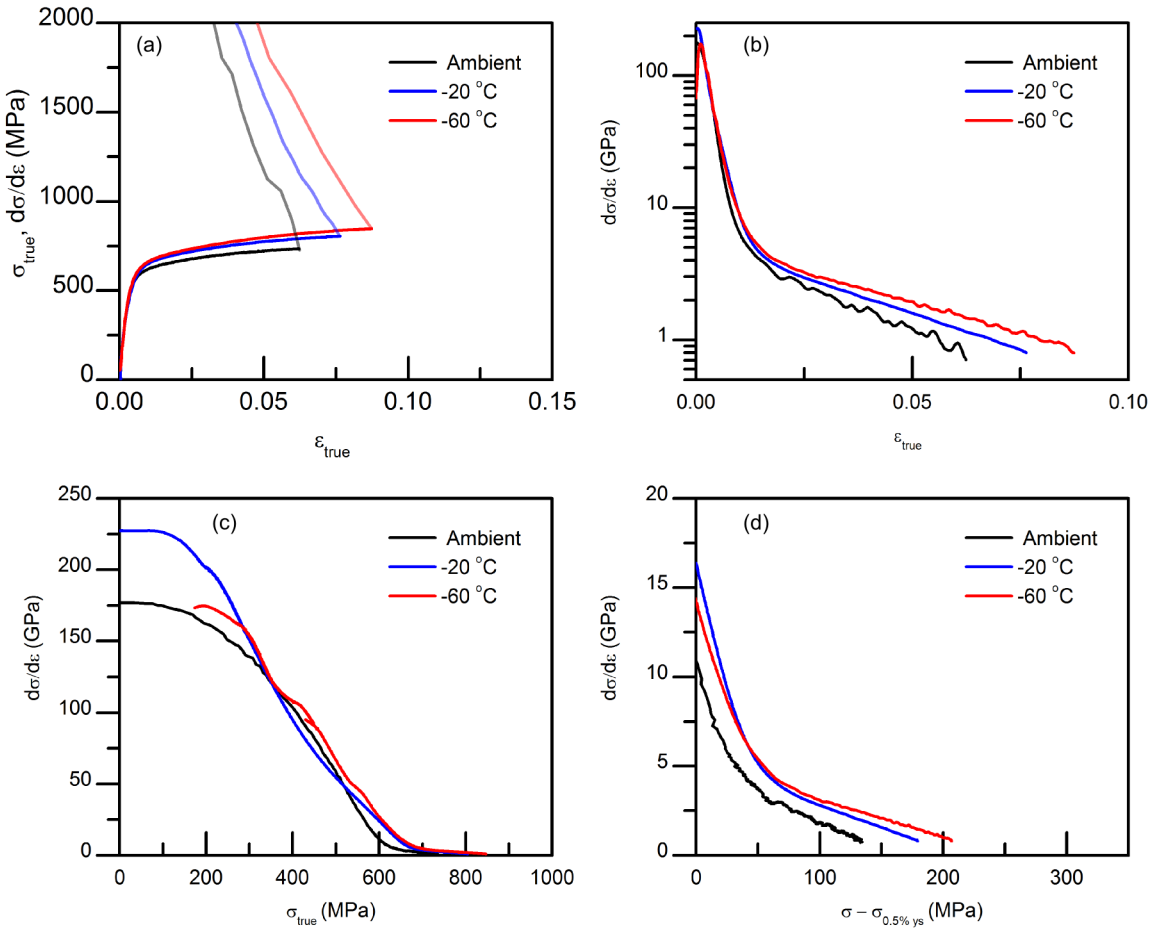

Figure 6.6: Analysis of tensile tests data from the condition with Nb in solution with a prior austenite grain size of 42 µm grain size and 10 °C/s cooling rate (lower bainite primary microstructure). Plots of (a) True stress vs true strain (b) θ vs true strain (c) θ vs true stress and (d) θ vs $\sigma - \sigma_{ys}$.

Figure 6.7 shows the comparison of the θ versus $\sigma - \sigma_{ys}$ plots at all testing temperatures for an example condition of each primary microstructure. From this figure, an important observation is that width of the curves, which is related to the extent of work hardening, decreases from the ferrite to the mixed ferrite/bainite, to the upper bainite and finally to the lowest in the lower bainite.

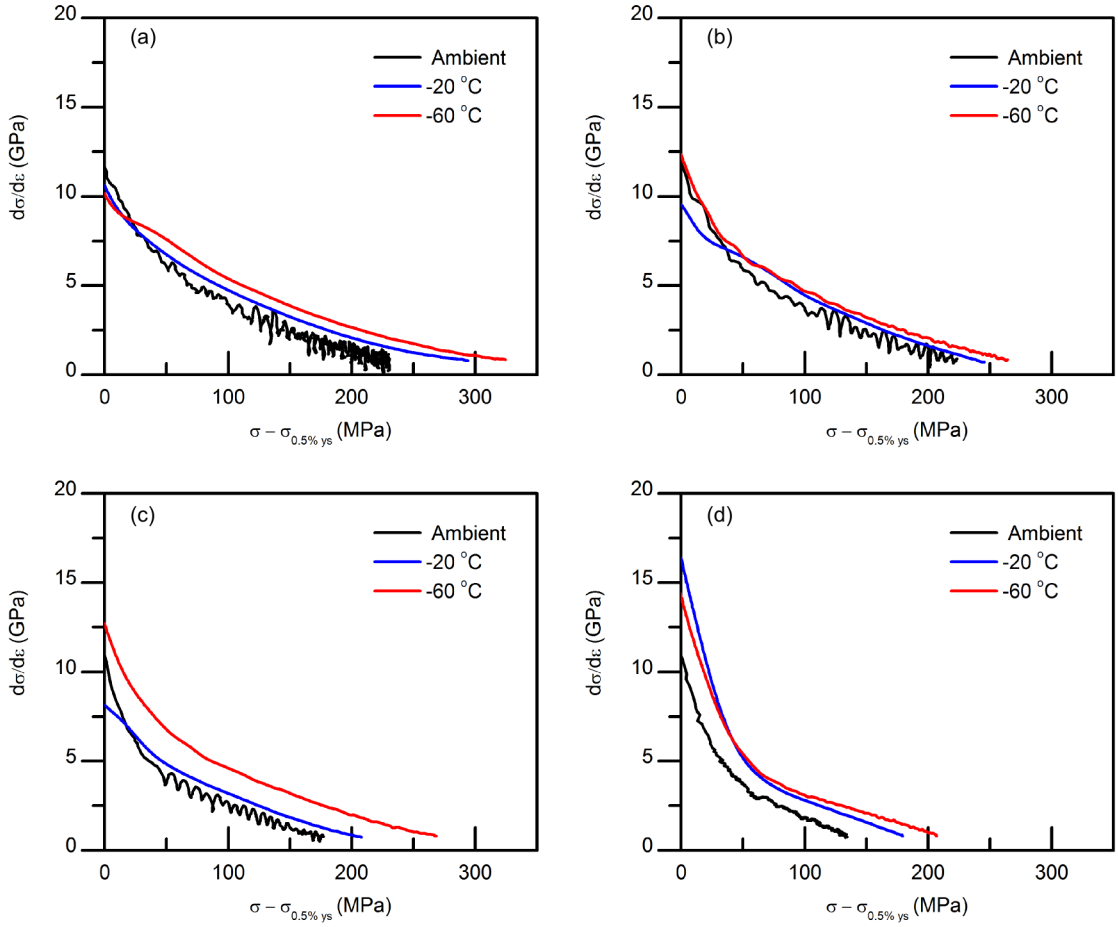

Figure 6.7: θ vs $\sigma - \sigma_{YS}$ of conditions with (a) ferrite primary microstructure (Nb in precipitates, 5 µm prior austenite grain size, 10 °C/s) (b) mixed ferrite/bainite primary microstructure(Nb in solution, 5 µm prior austenite grain size, 50 °C/s), (c) upper bainite primary microstructure (Nb in precipitates, 42 µm prior austenite grain size, 10 °C/s), and (d) lower bainite primary microstructure (Nb in solution, 42 µm prior austenite grain size, 10 °C/s).

For more detailed analysis, Table 6.1 presents the work hardening parameters for all tests and conditions while Figure 6.8 displays this data with respect to material properties (e.g. yield strength) or testing conditions (i.e. temperature).

Figure 6.8 (a) and (b) shows that the extent of work hardening ($\Delta\sigma_{\theta max}$) has correlation to both

Table 6.1: Work hardening operational parameters

Type	Temperature	θ_{max} (MPa)	$-d\theta/d\sigma$	$\Delta\sigma_{\theta max}$ (MPa)
Nb in precipitates, 5 μm @ 10 °C/s Ferrite	Ambient	6730	27	254
	-20 °C	6860	20	341
	-60 °C	7660	21	373
Nb in precipitates, 5 μm @ 50 °C/s Ferrite	Ambient	5730	24	236
Nb in solution, 5 μm @ 10 °C/s Mixed Ferrite/Bainite	Ambient	6710	24	277
	-20 °C	6610	22	302
Nb in solution, 5 μm @ 50 °C/s Mixed Ferrite/Bainite	Ambient	7280	28	257
	-20 °C	7360	26	285
	-60 °C	7280	25	296
Nb, in precipitates, 42 μm @ 10 °C/S Upper Bainite	Ambient	5430	26	206
	-20 °C	6360	24	263
	-60 °C	7100	23	311
Nb, in precipitates, 42 μm @ 50 °C/S Upper Bainite	Ambient	5350	32	166
	-20 °C	6600	27	240
	-60 °C	5260	22	240
Nb in solution, 42 μm @ 10 °C/s Lower Bainite	Ambient	5020	33	150
	-20 °C	4320	25	171
	-60 °C	4650	22	213
Nb in solution, 42 μm @ 50 °C/s Lower Bainite	Ambient	5400	47	114

yield strength and testing temperature. $\Delta\sigma_{\theta max}$ is seen to decrease with increasing yield strength in Figure 6.8 (a) and increasing with decreasing temperatures in Figure 6.8 (b). The increase of $\Delta\sigma_{\theta max}$ with decreasing temperatures can be explained in part by considering the effect of temperature on dynamic recovery as represented by $-d\theta/d\sigma$. The $-d\theta/d\sigma$ value is seen to to decrease with temperature as in Figure 6.8 (c). If θ_{max} is fixed, the influence of a lower $-d\theta/d\sigma$ would cause an increase in $\Delta\sigma_{\theta max}$ with decreasing temperature.

In Figure 6.8 (d) it can be seen that there is dependence of θ_{max} with microstructure. The microstructures with notable amounts of MA (i.e. the mixed ferrite/bainite, and the upper bainite microstructures) show a lower value of θ_{max} compared to the other microstructures. All θ_{max} values fall within the range of 5000 to 7500 MPa which compares well with literature on BCC metals which estimates θ_{max} to be equal to the shear modulus divided by 10 to 20, which works out to approximately 4000 to 8000 MPa [151] for steels. With regard to temperature, θ_{max} appears to

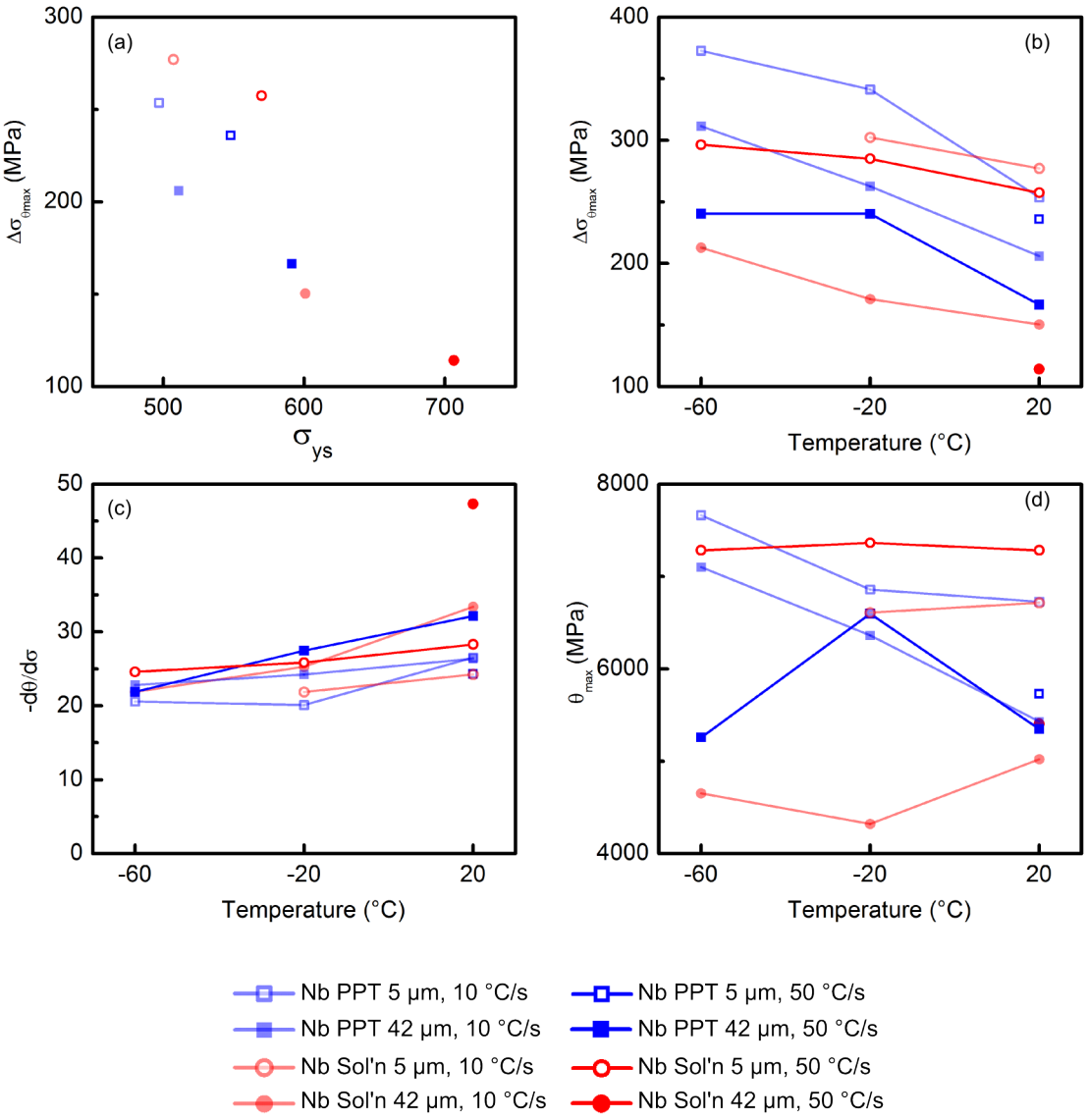

Figure 6.8: Plots of (a) $\Delta\sigma_{\theta max}$ vs $\sigma_{\text{ys 0.5\% offset}}$ at ambient testing temperature, (b) $\Delta\sigma_{\theta max}$ vs testing temperature,(c) $-d\theta/d\sigma$ vs temperature, and (d) θ_{max} vs temperature.

be temperature independent (i.e. within $\pm 10\%$) with two exceptions. The exceptions are those conditions of Nb in precipitates with a prior austenite grain size of 42 µm with cooling rates of 10 and 50 °C/s which are microstructures of mixed ferrite/bainite with significant MA which may significantly contribute to the work hardening. As θ_{max} is related to the k_1 term a temperature dependency is not expected for single phase materials.

A close examination of $-d\theta/d\sigma$ in Table 6.1 shows that the dynamic recovery term decreases most significantly in the lower bainite specimen, mainly upper bainite condition with the finer struc-

ture, and the ferrite specimen. The microstructures of primarily mixed ferrite/bainite, and upper bainite with a coarser structure show very little decrease of $-d\theta/d\sigma$ with decreasing testing temperature. This effect is clearly seen in Figure 6.8 (c), however it is not immediately clear why physically there would be such a significant difference in these specimens with respect to dynamic recovery processes between the microstructure types.

A recent approach by Bouaziz [152] to the Kocks-Mecking analysis proposes a modified dislocation density evolution law which can be applied to the current data. Bouaziz's proposed dislocation density evolution law is given as:

$$\frac{d\rho}{d\varepsilon_p} = M\left(\frac{k}{b}\sqrt{\rho}\exp(-\xi\sqrt{\rho})\right) \tag{6.8}$$

where M is the Taylor factor, k is a constant describing dislocation accumulation similar to k_1 from Kocks-Mecking analysis, and ξ is a characteristic length scale which can physically be interpreted as the capture distance for dynamic recovery. Note that this equation reduces to the Kocks-Mecking dislocation evolution equation if $\xi\sqrt{\rho} \ll 1$.

Using this evolution law, along with the dislocation density strengthening contribution a simple model of the stress strain curve can be made. In this model, the initial yield stress is set and the dislocation strengthening contribution is added to it, changing with incremental steps of strain. This model has four input parameters which are, k, the initial yield strength $\sigma_{ys\ 0}$, initial dislocation density ρ_0, and ξ value. Fitting these to the experimental curves is then done with three reasonable restrictions. Firstly, the k value is taken as a constant of 0.2 throughout all conditions and temperatures as it is assumed that the storage of dislocations in these microstructures are the same and is temperature and strain rate independent. Secondly, initial dislocation densities for a given microstructure remain the same at all test temperatures. That is to say the initial dislocation density of a microstructure is related to the transformation start temperature for given microstructure. Initial dislocation densities are selected to be within an reasonable range for a given microstructure, increasing with decreasing transformation start temperature (T_{start}) [16]. The relation between the selected ρ for the model and approximate T_{start} of the microstructures is shown in Figure 6.9. The third restriction is that for a given test temperature all test conditions should have the same ξ value. The ξ value is

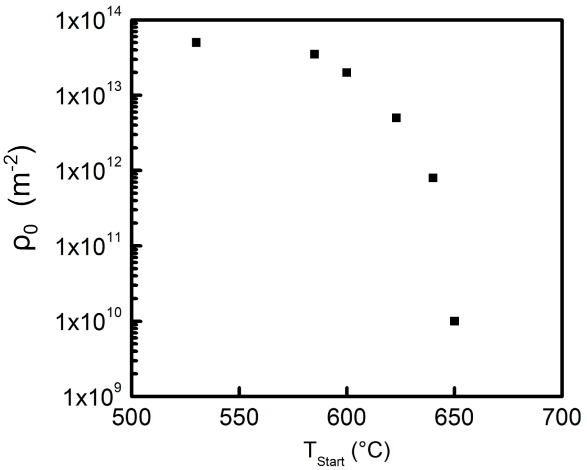

Figure 6.9: The relation between selected initial dislocation density and the approximate transformation start temperature based on the experiments of Reichert [147].

related to the rate of dynamic recovery for a given overall dislocation density. It is assumed that dynamic recovery has a temperature dependency as shown in Figure 6.10. The remaining fitting parameter then is the initial strength which is temperature dependent which is selected to give the best fit of the model to the current condition at the current temperature. By numerically integrating equation 6.8 the dislocation density evolution is determined with incremental steps of plastic strain. This contribution to the flow stress is then calculated using the Taylor equation as discussed previously and repeated here:

$$\sigma_{dis} = \alpha M G b \rho^{1/2} \tag{6.9}$$

To compare this model with the true stress-strain curves from experiments, the plastic strain for the experiments is determined according to:

$$\varepsilon_{plastic} = \varepsilon_{total} - \frac{\sigma_{true}}{E} \tag{6.10}$$

where $\varepsilon_{plastic}$ is the plastic strain, ε_{total} is the measured total strain, σ_{true} is the measured true strain, and E is the Young's modulus. Note the second term on the right hand side of the above equation represents the elastic strain. With $\varepsilon_{plastic}$ now defined, a comparison of the model to the experiment

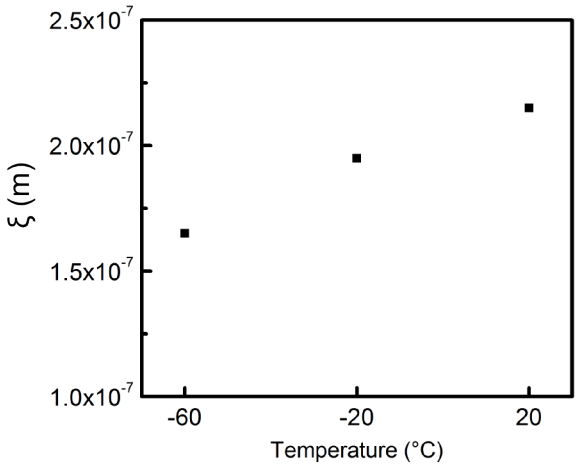

Figure 6.10: The selected value of ξ (i.e. related to dislocation capture distance for dynamic recovery) versus testing temperature

can be meed. Figures 6.11 and 6.12 shows this at all testing temperatures for tests from microstructures with a prior austenite grain size of 5 μm and 42 μm, respectively. Table 6.2 summarizes the model parameters used in fitting the model.

From the figures showing the model and experimental stress-strain curves it is seen that the model using the Bouaziz evolution dislocation density evolution law provides a good fit to all work hardening data. As this works for such a wide number of conditions with very few changes to parameters, this model is quite robust in describing work hardening behaviour. This model can be seen as a simple constitutive relation that accounts for test temperature via the initial yield strength and ξ values. However, the model does not well describe the observed elastic-plastic transition (e.g. figure 6.12 (d)), and this presents a limitations of the model. Further discussion of microstructure relations to work hardening behaviour will be revisited in the following discussion of the microstructure-property relationships.

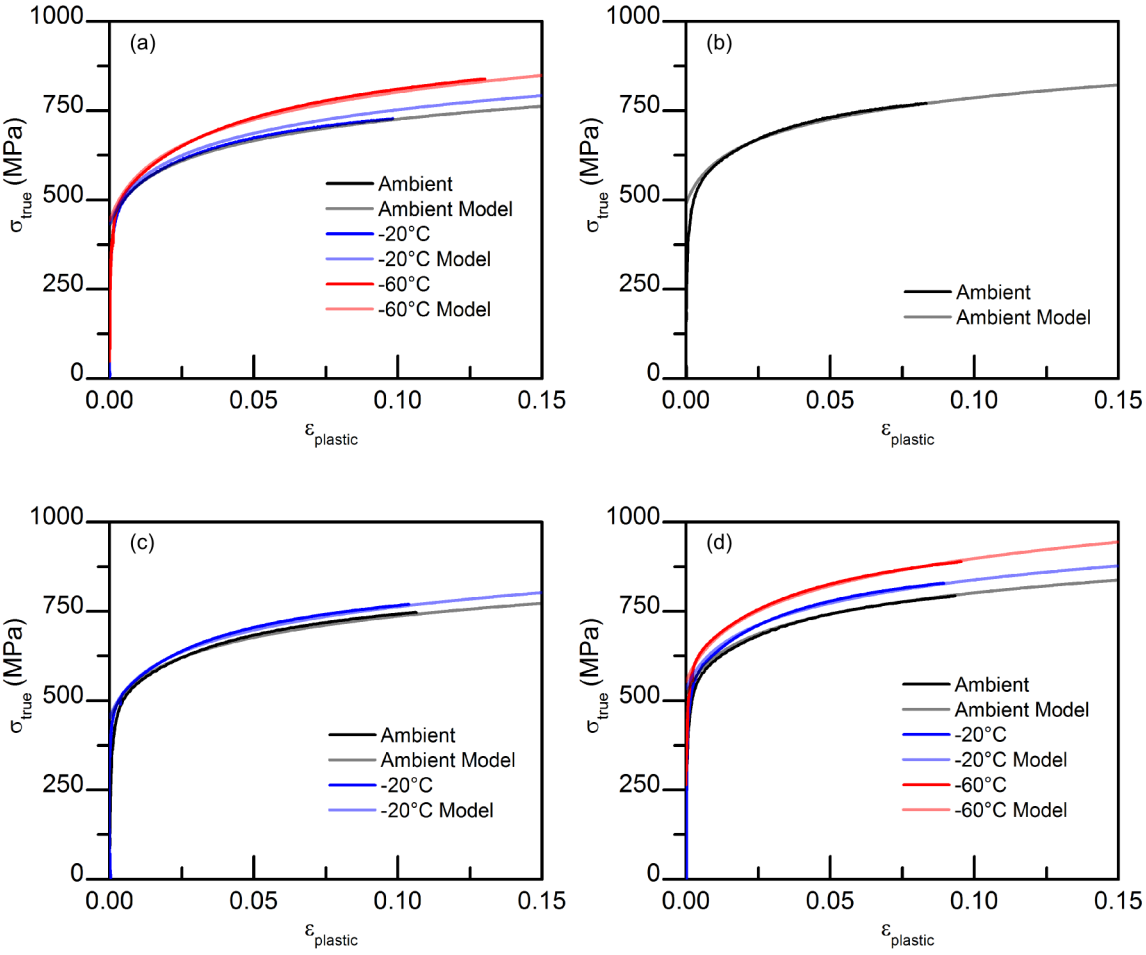

Figure 6.11: Model compared to true stress-plastic strain of 5 μm prior austenite grain size with Nb in precipitates with cooling rates of (a) 10 °C/s and (b) 50 °C/s, and Nb in solution with cooling rates of (c) 10 °C/s and (d) 50 °C/s.

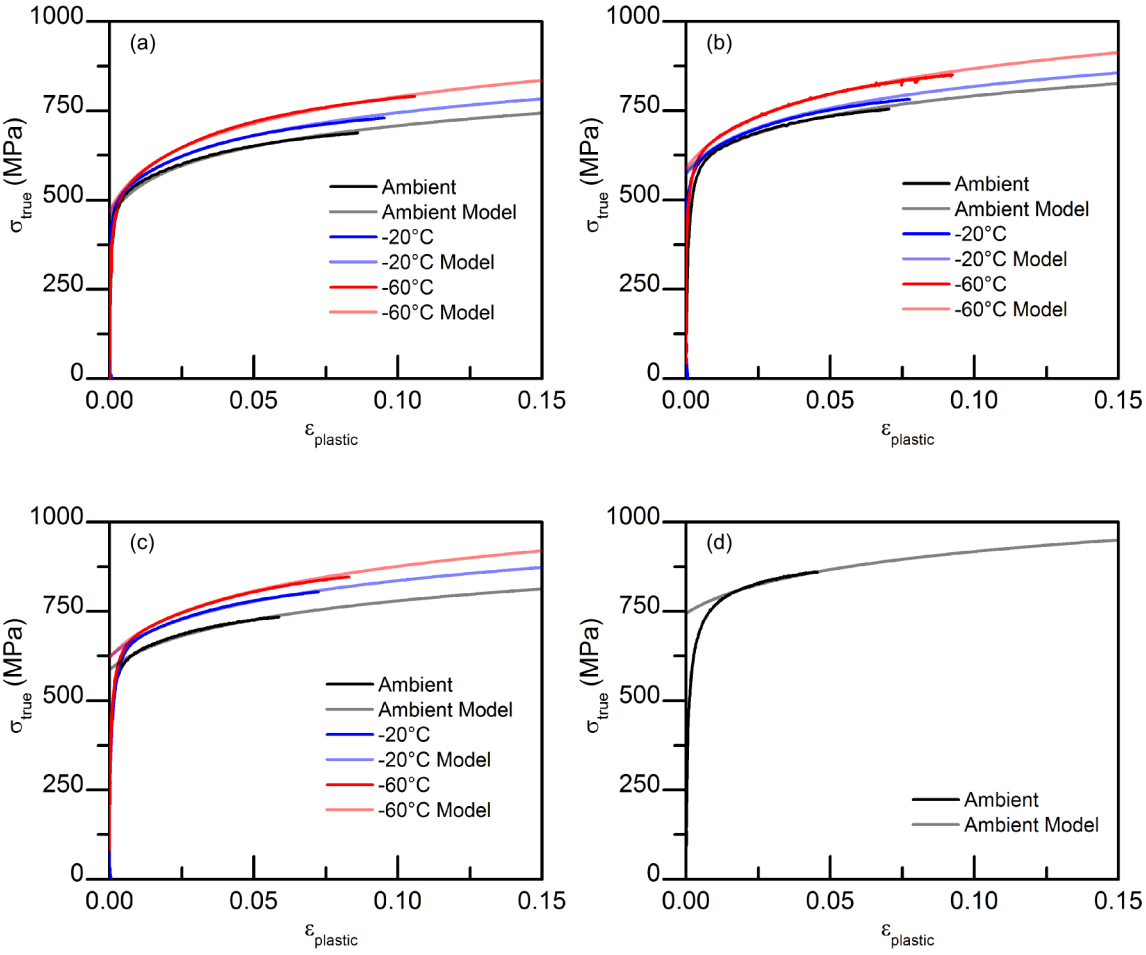

Figure 6.12: Model compared to true stress-plastic strain to failure of 42 µm prior austenite grain size with Nb in precipitates with cooling rates of (a) 10 °C/s and (b) 50 °C/s, and Nb in solution with cooling rates of (c) 10 °C/s and (d) 50 °C/s.

Table 6.2: Work hardening model parameters

Type	Temperature	ρ_0 (1/m^2)	$\sigma_{ys\ 0}$ (MPa)	ξ (m)
Nb in precipitates, 5 μm @ 10 °C/s Ferrite	Ambient	$1.0x10^{10}$	425	$2.15x10^{-7}$
	-20 °C	$1.0x10^{10}$	430	$1.95x10^{-7}$
	-60 °C	$1.0x10^{10}$	440	$1.65x10^{-7}$
Nb in precipitates, 5 μm @ 50 °C/s Ferrite	Ambient	$5.0x10^{10}$	485	$2.15x10^{-7}$
Nb in solution, 5 μm @ 10 °C/s Mixed Ferrite/Bainite	Ambient	$4.0x10^{11}$	435	$2.15x10^{-7}$
	-20 °C	$4.0x10^{11}$	440	$1.95x10^{-7}$
Nb in solution, 5 μm @ 50 °C/s Mixed Ferrite/Bainite	Ambient	$8.0x10^{11}$	500	$2.15x10^{-7}$
	-20 °C	$8.0x10^{11}$	515	$1.95x10^{-7}$
	-60 °C	$8.0x10^{11}$	535	$1.65x10^{-7}$
Nb, in precipitates, 42 μm @ 10 °C/S Upper Bainite	Ambient	$5.0x10^{12}$	405	$2.15x10^{-7}$
	-20 °C	$5.0x10^{12}$	420	$1.95x10^{-7}$
	-60 °C	$5.0x10^{12}$	425	$1.65x10^{-7}$
Nb, in precipitates, 42 μm @ 50 °C/S Upper Bainite	Ambient	$2.0x10^{13}$	485	$2.15x10^{-7}$
	-20 °C	$2.0x10^{13}$	490	$1.95x10^{-7}$
	-60 °C	$2.0x10^{13}$	500	$1.65x10^{-7}$
Nb in solution, 42 μm @ 10 °C/s Lower Bainite	Ambient	$3.5x10^{13}$	470	$2.15x10^{-7}$
	-20 °C	$3.5x10^{13}$	505	$1.95x10^{-7}$
	-60 °C	$3.5x10^{13}$	505	$1.65x10^{-7}$
Nb in solution, 42 μm @ 50 °C/s Lower Bainite	Ambient	$5.0x10^{13}$	605	$2.15x10^{-7}$

6.4 Microstructure-Tensile Properties Relationships

With results of the microstructures and the mechanical properties from the Gleeble heat treated samples having been presented, the relation of how the former leads to the latter can now be discussed. This discussion will focus on how microstructure relates to the properties determined from the tensile tests at ambient temperatures. Where prominent, the discussion is expanded to examine temperature effects on the microstructure-tensile property relationship.

The tensile properties up until necking can be seen to be primarily affected by two microstructure features. These two features are the constituents and the characteristic length scale of the microstructure. This can be seen for example in Figure 6.13 which shows the different yield strength, tensile strength and uniform elongation against the primary microstructural constituent at ambient testing temperatures. From this graph it is seen that the lowest strengths but highest uniform elongations are given by the samples with primarily ferrite as the major constituent, with a coarse mor-

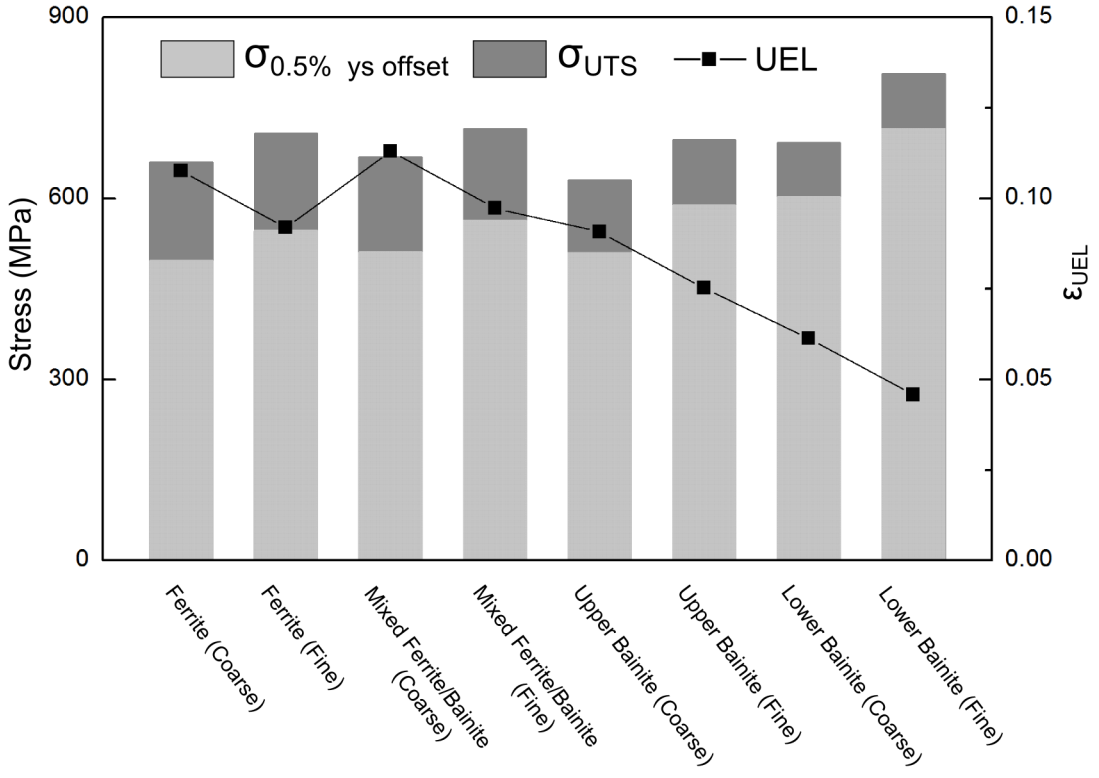

Figure 6.13: Yield strength, tensile strength and uniform elongation at ambient temperatures plotted for each microstructure.

phology. At the other extreme, the highest strengths, which correlates with lowest uniform elongation, are found in the microstructure with lower bainite as the main constituent with the finest structure. Of samples with similar microstructures, it is seen that as the microstructure is refined both yield and tensile strength increases, while uniform elongation decreases.

To discuss the relation of microstructure and tensile properties, it was seen in Section 2.8 that equation 2.5 well represented the individual contribution mechanisms to the strength of a specimen. This equation is repeated here:

$$\sigma_{tot} = \sigma_0 + \sigma_{ss} + \sigma_{ppt} + \sigma_{dis} + \sigma_{gb} \tag{6.11}$$

To examine further the differences in strength resulting from microstructural changes, it is useful to discuss the influence of the various microstructures on the strengthening terms of equation 6.11. To quickly review, the strengthening contributions can be separated into the inherent strength of the lattice to dislocation movement (σ_0), solid solution strengthening (σ_{ss}, precipitation strengthening (σ_{ppt}), dislocation interaction strengthening (σ_{dis}), and grain boundary strengthening σ_{gb}). Each of these contributions will now be discussed individually with respect to the microstructural constituents observed. As the primary microstructures (ferrite, upper bainite, lower bainite) are BCC matrices, it would be expected that σ_0 would be similar for each of these phases. On the other hand, the MA phase will have a different σ_0, as both of the structures that make up this phase have a different lattice structure (body centered tetragonal (BCT) for martensite, FCC for austenite). As the fraction of MA is relatively low in the ferrite and lower bainite specimens (i.e. less than 5%) and to a first approximation can be ignored. The more significant MA fractions (i.e. $\approx$10%) in the mixed ferrite/bainite as well as upper bainite specimens mean that the σ_0 may need to be accounted for. The relative amount of martensite and retained austenite remains difficult to characterize. It is not clear how significant the influence of these phases will be on the composite strength of the microstructures, although recent preliminary work by Reichert [153] using EBSD suggests that martensite primarily makes up the MA in these cases. The BCC structures of ferrite, upper bainite, and lower bainite along with the BCT structure of martensite would be expected to have a relatively high Peierls-Nabarro strength and strong temperature dependence. On the other

hand the FCC austenitic structure would not be expected to have a strong temperature dependence. Specimens with a high amount of MA (i.e. mixed ferrite/bainite, and upper bainite) may show less temperature dependence in the σ_0 term if the austenite is the predominate constituent of the MA phase.

Solid solution strengthening changes in two ways for this study, firstly by design wherein the presence of Nb(C,N) is controlled, and secondly how the solid solution strengthening elements are distributed in the microstructure with respect to its constituents. While Nb is noted to have a moderate solid solution strengthening effect, it is relatively unimportant compared to the interstitial solutes of C and N. Therefore it is most important to consider the amount present and the distribution of these elements, and in particular the carbon. The primary phases of ferrite, upper bainite, and lower bainite are known to have low solubilities of C. It is expected, regardless of the presence of Nb(C,N), that C which is in solution becomes distributed into the MA phase or precipitated out in another form (such as interlath carbides in upper bainite, or intralath carbides in lower bainite), or some combination thereof. In the case of C enriching the MA phase, a significant increase of the σ_{ss} component for each of these phases would be expected. In samples where Nb(C,N) has been dissolved there is potential for the MA phase to reach higher carbon contents, and consequently higher solid solution strengthening contributions. However, as there is only a limited amount of Nb in this chemistry, it can be expected that the difference is not significant. Consequently, the contribution of solid solution strengthening is likely to be similar and limited in significance for the primary microstructure constituents of ferrite, upper bainite and lower bainite.

Consideration of changes to the strengthening contribution of precipitates follows a similar argument to that of solid solution. That is, changes to σ_{ppt} are determined on one hand by the amount of Nb(C,N) precipitates present by design, and secondly by which precipitates form and how they are distributed in each constituent. Regarding the Nb(C,N) precipitates, these are found in the as-received material to be well distributed throughout the microstructure and consisting of two sets of sizes (i.e. 2 nm and 69 nm respectively) [143]. It is assumed that the majority of Nb in the as-received material is contained within the Nb(C,N) precipitates. In the case of Nb in precipitates with a 5 μm prior austenite grain size, no solutionizing treatment was applied and the final microstructures (which are the samples with the main constituent of ferrite) are expected to have the same distribution Nb(C,N) precipitates. In the sample with Nb in precipitates and a 42 μm prior austenite

grain size, which are the specimens with upper bainite as the primary constituent, the solutionizing treatment combined with the 20 minute reprecipitation only resulted in about 50% of the Nb being in precipitates [147]. As these precipitates are formed in austenite, they are expected to be relatively coarse and thus their strengthening contribution would be low.

Besides Nb(C,N) precipitates, there are many others that may contribute to the strengthening effect such as TiN, or MoC. Importantly, TiN is not significantly influenced by the thermal treatments applied here and will remain consistently distributed in all microstructures. MoC on the other hand will dissolve in solutionizing treatments and will not precipitate under the cooling conditions applied, which means this distribution should remain consistent across the microstructures as well. An important difference is recognized in the distribution of carbides between upper bainite and lower bainite constituents exists. In upper bainite, larger sized carbides are formed between bainite laths. As these are not in the matrix of the upper bainite, they will not interfere directly with the dislocation motion and their contribution to σ_{ppt} will be limited. In lower bainite, carbides also form between the bainite laths, although these precipitates are smaller. Furthermore, in lower bainite carbides also form within the laths, but as these are relatively coarse they will not likely add significant strength to σ_{ppt}.

As previously stated, there is a significant increase in strength observed for samples with the same primary microstructure but different characteristic length scales. For cases where only the length scale is changing with the same primary microstructure then the most significant change on the tensile strength would be through the grain size effect on strengthening. This contribution typically defined by the Hall-Petch equation, as given in equation 2.11, shows that grain size strengthening is inversely proportional to the square of the effective grain size. In ferrite specimens the effective grain size can be taken to be equal to the actual grain size. For microstructures with upper and lower bainite, the effective grain size can be associated with the lath size. In every case, the effect of a higher cooling rate but with a same final primary microstructure constituent results in a significant refinement of microstructure (i.e. effective grain size) and consequently a higher strength for these structures. Grain size thus has a critical influence on the strengthening contributions.

The microstructure relation to the dislocation strengthening contribution (σ_{dis}) will be discussed first in terms of the initial dislocation density which influences the yield strength, and then in terms of the evolution of the dislocation density (and thus strain hardening behaviour). The initial dis-

location density differs between the microstructural constituents. The initial dislocation density increases progressively with lower temperature transformation products, which is to say ferrite has a lower initial dislocation density than upper bainite, which is less than lower bainite, which is less than martensite. As a result, the initial dislocation strengthening contribution will follow the same trend. This effect is likely to be a major factor in this study across the various microstructures, and indeed the observed yield strength follows this trend.

The strengthening contribution and resulting work hardening behaviour is complexly related to the microstructure. The dislocation strengthening contribution, previously presented in equation 2.9, is repeated here:

$$\sigma_{dis} = \alpha M G b \rho^{1/2} \tag{6.12}$$

The dislocation evolution equation from Bouaziz, previously introduced in equation 6.8, and repeated here:

$$\frac{d\rho}{d\varepsilon_p} = M\left(\frac{k}{b}\sqrt{\rho}\exp(-\xi\sqrt{\rho})\right) \tag{6.13}$$

It is of interest to discern how the initial dislocation density, dislocation storage (k), and dynamic recovery processes (ξ) vary with microstructure. Utilizing the discussion presented on the Kocks-Mecking analysis of the results, some speculation can be made as to how microstructure affects the various parameters. The initial dislocation density varies with microstructure according to the strain of transformation. It is expected that the initial dislocation density increases with decreasing transformation start temperature of the microstructural constituent as discussed previously, and indeed correlates with the yield strengths observed from the thermally treated specimens. Alongside the grain size strengthening contribution, the dislocation strengthening contribution also represents a primary influence on the strength differences between microstructures.

So far the discussion of the dislocation strengthening contribution has focused on the initial yield strength, and thus the initial dislocation density, of the material. The evolution of strength

with strain, and thus the evolution of dislocation density is important and is seen to vary with microstructure constituent. In the Bouaziz model it was seen that the dislocation storage term k is related to θ_{max} while dynamic recovery processes represented by the ξ term are related to $-d\theta/d\sigma$. First considering the dislocation storage, it is seen that there is a weak correlation at least at ambient temperatures of θ_{max} on yield strength, with θ_{max} decreasing slightly with increased yield strength. This trend is at best weakly correlated with the initial dislocation density relation to transformation start temperatures (i.e. ferrite specimens with low initial dislocation densities give higher θ_{max} values and lower bainite specimens with higher initial dislocation densities give lower θ_{max} values).

The dynamic recovery, or the ξ term, is related to $-d\theta/d\sigma$ value from the Kocks-Mecking analysis. This value does not show any consistent trend with microstructure constituent. The majority of the $-d\theta/d\sigma$ values at ambient temperatures fall within the range of 24 to 33, but the lower bainite microstructure with the fine length scale show a significantly higher $-d\theta/d\sigma$ of 47. It is not immediately clear why $-d\theta/d\sigma$ for this exceptional condition is so high. The fact that this exceptional condition shows a very small amount of work hardening means that there is a small range to evaluate, as well the non-distinct elastic-to- plastic transition may explain some uncertainty in this value. Interestingly, it was shown that when the Bouaziz dislocation model is used, the fit even to this extreme condition appears to be fairly good with one value of ξ (i.e. capture distance for dynamic recovery) at ambient temperature. This supports the assertion that this point of $-d\theta/d\sigma$ for lower bainite is an outlier due to analysis sensitivities. Furthermore, the use of the model highlights the fact that dynamic recovery is insensitive to the differences between these microstructures.

The dynamic recovery term is also expected to have a temperature dependency. This dependence is seen with $-d\theta/d\sigma$ decreasing with decreasing test temperature. This in turn gives the work hardening behaviour a temperature dependence. This effect is significant as work hardening was seen to differ with temeprature clearly from the experimental stress-strain curves. Using the Bouaziz model, a clear temperature dependency of the ξ value was seen to fit all curves well. From observations, the decrease in $-d\theta/d\sigma$ with decreasing temperature is noted to be greatest in samples with primary microstructures of lower bainite, and of upper bainite with a finer microstructure. It is uncertain why these cases in particular show a stronger decrease of $-d\theta/d\sigma$ by observations, but as the ξ fit to the stress strain curves is robust it is likely that the stronger decrease may again, be due to an issue with sensitivity in the analysis.

The grain boundary strengthening effect was previously discussed on the basis of comparing between microstructures of the same primary constituent. It was discussed that this effect was quite significant within the basis of consideration. Considering now the difference between microstructures on the basis of their effective grain sizes (i.e. related to the typical grain size definition in ferrites, or related to lath spacings in bainites), it is reasonable to correlate the increase of yield strength microstructures with the decrease in effective grain sizes when comparing microstructures. As the effective grain sizes vary significantly with microstructure (ferrite given the largest, and lower bainite the lowest), the strength can be expected as well to vary significantly. This is indeed observed in the results.

6.5 Kahn Tear Testing

In Kahn tear testing it was seen that all conditions failed in a ductile manner. This is in line with the ductile failure seen in all conditions of the tensile tests. As such, Kahn results detail differences in ductile failure between the different microstructures. In distinction from the tensile tests, the presence of a notch then growing crack allows for the examination of this ductile failure in a state of higher stress triaxiality. Before such comparisons are made, a critical look at the testing method is presented.

The Kahn tear test was selected for this study for numerous reasons, but particularly that of its compatibility with Gleeble specimen dimensions and simplicity in setup and measurement. In turn, there were a number of issues related to using this test as a fracture test. Foremost is the fact that the plane-strain condition is not reached. A quick calculation estimates that the plane strain condition would require a thickness over 17 mm. This thickness cannot be met due to both limitations of the Gleeble testing, and the simple fact that this is actually thicker than the supplied plate. Consequently, there will be an influence of thickness and plasticity on the ability to measure a true fracture toughness in a simple manner. It was seen in testing (see Figure 5.24) that even the relative measures of toughness of E_{tear} and UPE_{d0-1} showed a dependence on thickness. While these values were corrected for thickness previously, and henceforth these corrected values are referred to as E_{tear} and UPE_{d0-1}, they still do not represent true fracture toughness. As both of these values are determined using an energy taken directly from the load displacement curve they do not only represent of the energy associated with the fracture process. Consequently, there is no

simple analytical relation between these values and typical true toughness measures.

The inability of E_{tear} and UPE_{d0-1} to measure a true fracture toughness does not preclude the use of these values to potentially represent the toughness in a relative but quantitative way of the samples tested here. As the tested conditions have somewhat similar tensile properties (i.e. yielding and strain hardening is comparable for all specimens), it is reasonable to expect that any observed differences in these values between conditions will be the result of microstructural differences on ductile fracture. That is to say the effects from different tensile properties on plastic zone size development with respect to both in-plane plastic zone size and the extent of thinning at the crack tip is relatively insignificant over the range of yield strengths, tensile strengths, and strain hardening rates as observed in tensile testing. In addition, it is important to consider the error in these measurements. Specifically, the use of a crack measurement in E_{tear} calculations introduces a possibility for greater error associated with accuracy in the crack length measurement. In developing the master curve for crack elongation with displacement at a given thickness it was seen that there was moderate but acceptable scatter in the crack length measurements. Additionally, there was an assumption of applicability of these crack curves from ambient temperatures to the lower testing temperatures. As the material largely shows comparable stress-strain responses at these temperatures it seems reasonable that crack growth will occur in a similar manner. Considering then that E_{tear} and UPE_{d0-1} can be taken as relative measures of ductile fracture toughness, the discussion can move on to examine the effectiveness of using these values in practice to compare ductile fracture resistance of different microstructures.

Between the values of E_{tear} and UPE_{d0-1} there are some differences in ranking the microstructures. E_{tear} represents a more rigorous method of measuring relative toughness to which UPE_{d0-1} value can be compared. However, given the practical difficulties with determining the E_{tear} value the question remains if UPE_{d0-1} can adequately be used. This comparison can easily be observed by plotting E_{tear} against UPE_{d0-1} normalized by their maximum values, as shown in Figure 6.14. Note for this figure, and future figures referring to Kahn properties, error bars are defined based on the standard deviation of nine tests of the as-received material. In this figure, if these two values were perfectly proportional the data would collapse to a direct relation. In doing so, some differences are noted. Notably, for the condition with Nb in precipitates, prior austenite grain size of 5 μm and 10 °C/s cooling show quite low values of E_{tear}, indeed the lowest values, but

from the UPE_{d0-1} this condition is not so low compared to the other conditions. The condition with Nb in solution, prior austenite grain size of 5 µm and 50 °C/s cooling shows a significant increase in ranking when comparing E_{tear} and UPE_{d0-1} values. In fact, this condition results in one highest corrected UPE_{d0-1}. Consequently, the use of UPE_{d0-1} values is not recom-

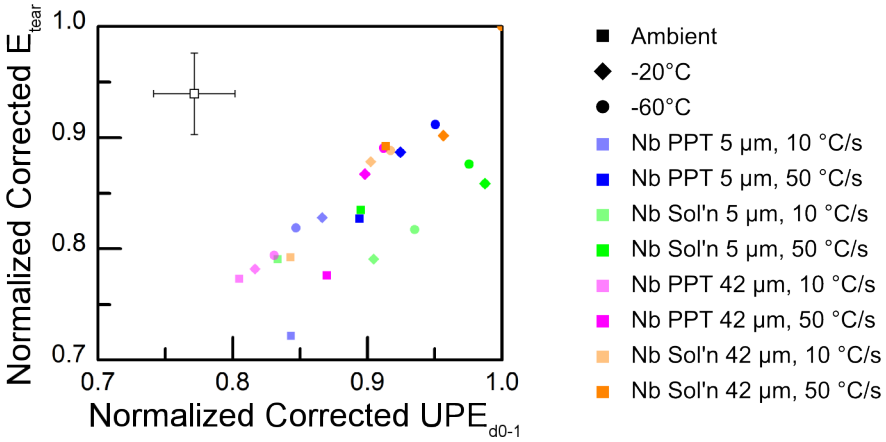

Figure 6.14: Corrected and normalized E_{tear} plotted against corrected and normalized UPE_{d0-1}. The symbol in the upper left represents the uncertainty for each data point in the figure.

mended over E_{tear} for comparing relative toughness values as it will lead to a potentially different ranking. Only when the difficulty of obtaining crack length measurements prohibits determination of E_{tear} values should the UPE_{d0-1} value be used.

Using the E_{tear} value then, it is possible to look into microstructure property relationship. Figure 6.15 plots the E_{tear} value at various temperatures against the testing condition. There are three notable trends. First, decreasing testing temperatures tends to be associated with an increase in the E_{tear} value, with the most notable exception of this trend being the condition of Nb in precipitates with a cooling rate of 10 °C/s. It is possible considering the error within the experimental data that this is not actually an exception, and other may be exceptions to this trend, however it is expected that for every condition there would be no exception to the stated trend. Secondly, there is an increase of E_{tear} with a higher cooling rate which creates a finer final microstructure. Finally, as the E_{tear} appears to have a modest increase with increasing amounts of bainite, with the highest values being observed in lower bainite.

In ductile failure, voids nucleate, then grow and finally coalesce causing fracture. In stable crack

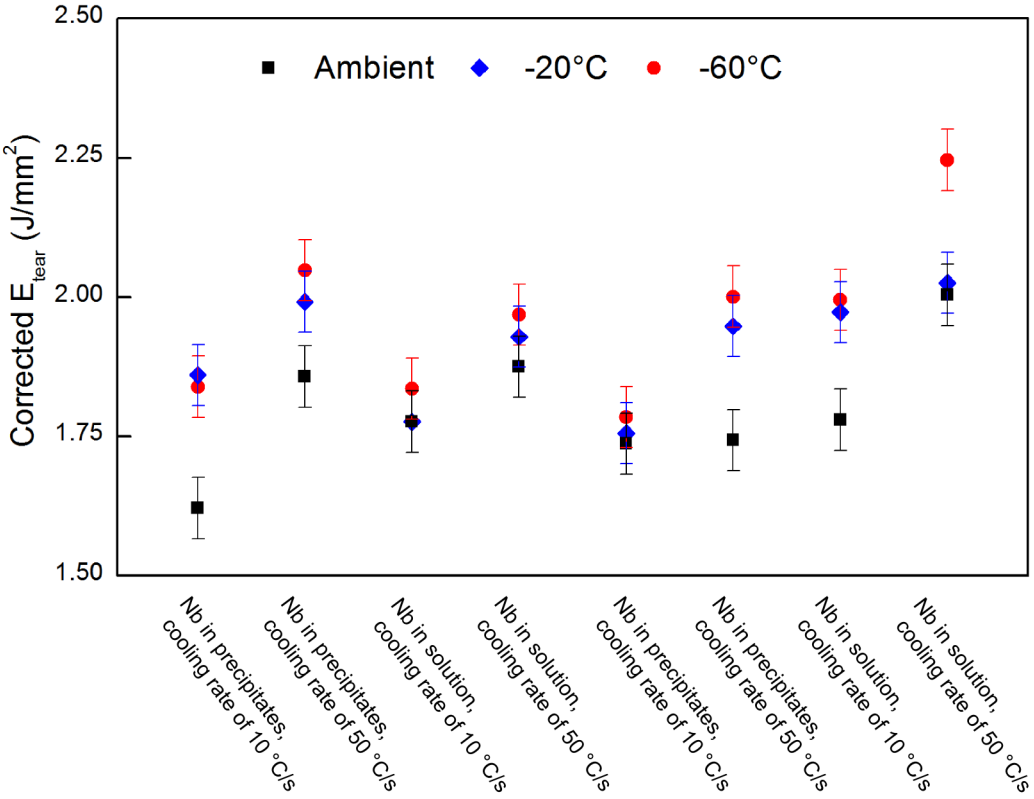

Figure 6.15: Corrected E_{tear} plotted against the testing condition.

growth, this process occurs continuously. The mechanism by which ductile voids grow involve the plastic motion of dislocations. As such, influences on yield strength will also effect the ductile fracture energy. It is unsurprising to find that a decrease in temperature, known and shown previously here to cause an increase in yield stress, has resulted in the observed positive correlation between test temperature and E_{tear}. Similar to this, the decrease in coarseness of a microstructure correlates with an increase to yield strength, and as such can explain the increase of E_{tear} with increasing cooling rate for a given primary microstructure. In general, this trend of yield strength correlating to an increase of E_{tear} seems to hold fairly well and may also in part explain the differences between microstructures. This is exemplified in Figure 6.16 which plots the tensile yield strength against the E_{tear} value. Note there are two exceptional cases, that of the fine upper bainite microstructure and that of the coarse lower bainite microstructure, showing lower E_{tear} values then expected for their $\sigma_{0.5\%ys}$ values. Unexpectedly, this relatively low E_{tear} value is seen only for these conditions at ambient temperatures.

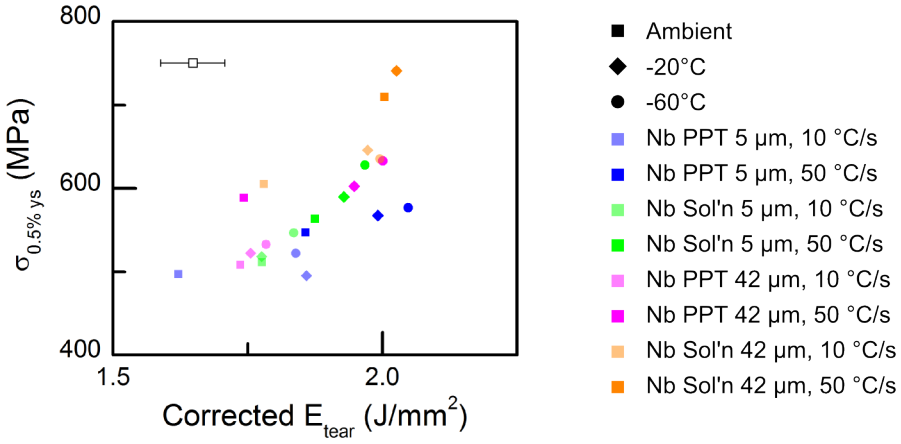

Figure 6.16: $\sigma_{0.5\%ys}$ plotted against corrected E_{tear}.

Figure 6.16 showed that there may be relations that can be made between Kahn and tensile tests, specifically between $\sigma_{0.5\%ys}$ and E_{tear}. It may be insightful to examine data between these tests to reveal any other potential relations. Figure 6.17 shows a number of plots comparing tensile to Kahn test properties. First, Figure 6.17 (a) and (b) show the expected relation of strength values (yield and tensile strengths respectively) to the tear strength. The fact that these both relate to the tear strength is unsurprising but lends confidence to the consistency of the testing method. Figure 6.17 (c) shows the tensile fracture strain plotted against E_{tear} while Figure 6.17 (d) shows the corrected tensile fracture stress plotted against the tear strength. What is seen is a lack of any correlation between measured tensile properties at fracture and properties from the Kahn tear test. This shows the practical limitation of tensile testing to characterize the ductile tearing behaviour. It also validates the use of Kahn tear tests in this work as it provides insight into the ductile fracture properties that otherwise would not have been observed.

To emphasize again, no brittle behaviour is observed. As such, the relative comparison of toughness is based on the ductile fracture of these specimens. While it was not possible to expand the testing matrix due to limited materials and time, it would have been informative to continue Kahn testing to colder temperatures or increase the crosshead speed so as to observe and compare the conditions under which these microstructures undergo the ductile to brittle transition. While thicker specimens would also have been desirable (e.g. would have provided more constraint at the notch root), producing these microstructures in a controlled and consistent way as was done in

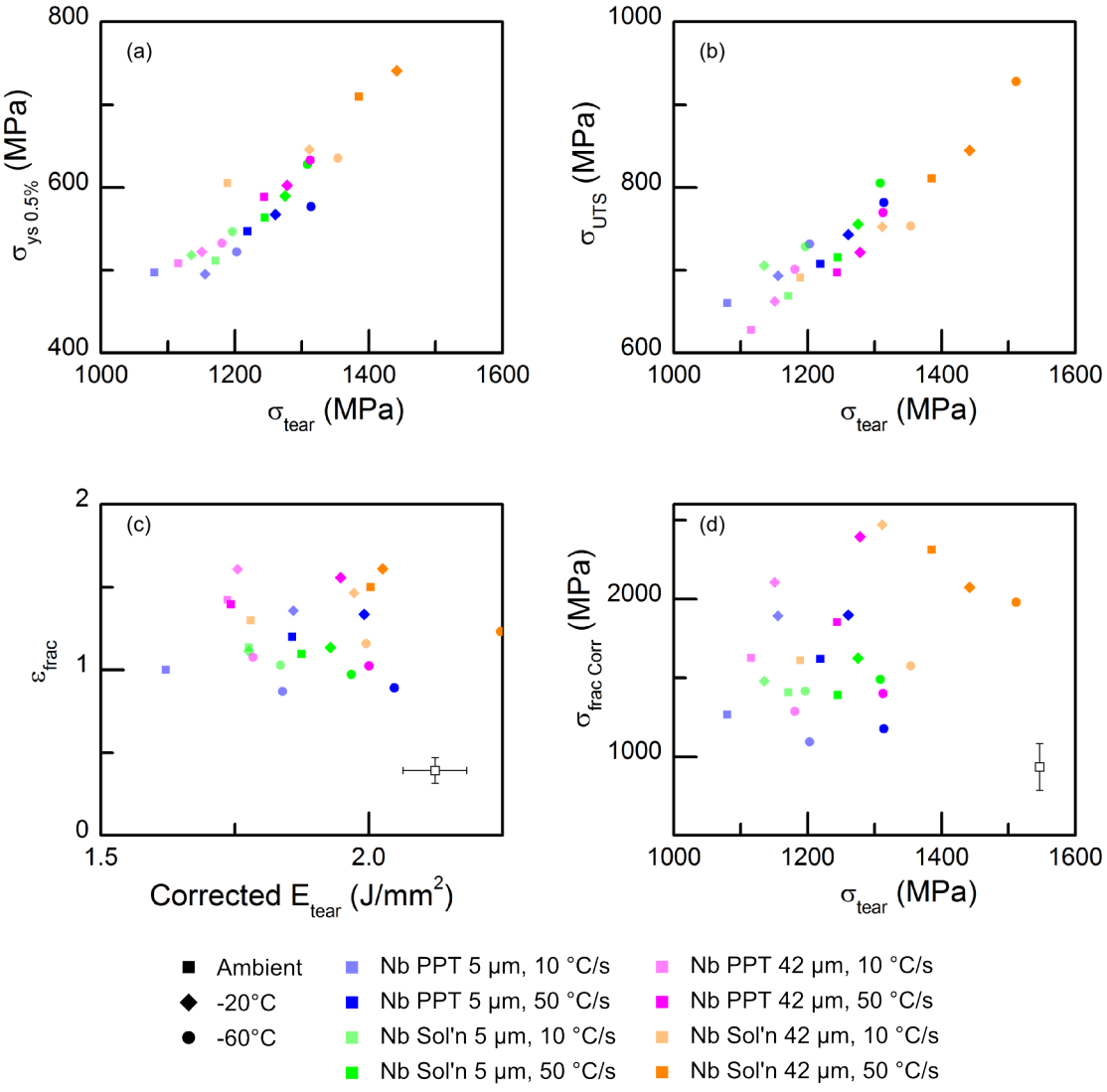

Figure 6.17: Tensile properties compared to Kahn properties. (a) $\sigma_{0.5\%ys}$ plotted against σ_{tear}, (b) σ_{UTS} plotted against σ_{tear}, (c) ε_{frac} plotted against corrected E_{tear}, and (d) corrected σ_{frac} plotted against σ_{tear}. The symbol in the bottom right of (c) and (d) represents the uncertainty for each data point in the figure.

this study would not have been possible. Ultimately, this leaves a significant gap in evaluating the toughness of these microstructures relevant to the HAZ. On the other hand, the testing conditions reached a fairly extreme temperature (-60 °C) with all microstructures showing a ductile failure. This in and of itself suggests that these microstructures are inherently tough, and consequently the steel chemistry used here is robust.

CHAPTER 7

Concluding Remarks

7.1 Summary

The HAZ of single and dual torch welds experience a very complicated thermal history. This history varies spatially around the weld and produces a gradient of microstructures. The mechanical properties are directly related to the microstructure and as a result any tests on actual welds will sample a range of microstructures. The objective in this work was to create bulk specimens of individual microstructures so that detailed characterization of the structure property relationship could be carried out. This was accomplished by first making temperature measurements in the real HAZ of a full thickness pipeline GMAW weld performed with parameters expected to be in use in field conditions, and with single torch, as well with dual torch with spacings of 2.75", 4", and 7". Based on microstructure work from the real HAZ, and from project work from colleagues, specific microstructures were selected then reproduced in bulk specimens for mechanical testing. Tensile and Kahn tear testing was performed at ambient, -20 °C, and -60°C in order to investigate how these microstructures perform under the potentially extreme service conditions that they may be exposed to.

The following summarizes the primary results of this work:

- Cooling rates in the HAZ for the main fill passes were observed to be on average 100 °C/sec in single torch welds, on average 54 °C/sec in leading torch of dual torch welds, and on average

18 °C/sec in the trailing torch of a dual torch welds. Microstructures observed in the HAZ showed varying amounts of ferrite, upper bainite, lower bainite, and MA.

- Thermal simulations for creating bulk specimens suitable for mechanical testing were refined in order to produce microstructures relevant to the observed HAZ. Microstructures consisting primarily of ferrite, primarily of upper bainite, and primarily of lower bainite were produced with at least two different refinements. All microstructures were characterized with respect to the amount of primary microstructural constituents as well as for their amount of MA phase.

- Tensile testing showed that the highest strengths and lowest ductility was observed in microstructures with the primary constituent of lower bainite. Ferrite, mixed ferrite/bainite and upper bainite showed comparable strength levels, however it is seen that ductility was decreased for samples with a primarily upper bainitic microstructure.

- The Bouzaiz dislocation based model for work hardening was shown to provide a good fit across all temperatures and conditions with minimal fitting parameters. Interestingly, it was seen that the ξ value, which is related to the dislocation capture distance for dynamic recovery, was observed to linearly decrease with temperature.

- The Kahn tear testing was investigated in terms of its ability to study the fracture of steel. It was found that the method cannot easily provide fracture toughness parameters such as K_{IC}, but can provide a relative measure of toughness. Kahn tear testing showed that even in the presence of a stress concentration at cold temperatures (-60 °C) that all microstructures failed in a ductile manner at the strain rates used.

There are a number of important outcomes from this work. The temperature measurements of the dual torch welds in the HAZ represents a completely novel data set. This data can be used, as was the case in this work, to guide microstructure evolution work through the use of thermal simulations. It was a technical achievement to produce thermally treated specimens of a bulk microstructure based on this data that was suitable in size for both tensile and Kahn tear testing. Most importantly, by examining conditions and microstructures that bound those observed in the real HAZ and then measuring tensile and Kahn tear properties there is potential to utilize this work to form the basis of a full microstructure-property relationship to determine the local properties of microstructures

in the HAZ at a wide range of potential operating temperatures. This is particularly useful if a microstructural evolution model, as has been developed in the group at UBC, is created and used as an input for such a model. Furthermore, there is the potential to use this data to model the overall HAZ mechanical behaviour by combining each of the local microstructural responses.

7.2 Future Work

This work has left a number of potential opportunities for future work to follow:

- Conduct additional testing of existing conditions where tests either failed or were limited in number in order to improve confidence of results observed in this work.

- Investigate opportunities for improvement to Kahn tear testing, both in general and with respect to properties relevant to this study. Specific to this study, it would be of interest to extend testing to colder temperatures, or at higher strain rates in order to investigate the transition from ductile to brittle fracture. Using digital image correlation to examine crack growth and plastic zone development could be considered for a greater understanding of ductile fracture at room temperatures. The use of anti-buckling guides to prevent or delay buckling at the far side of the ligament could be a way to extend the range over which useful information can be observed. Additional analysis, such as utilizing two extensometers and accounting for the geometry in rotation, could potentially be of interest in trying to obtain a more suitable direct measure of fracture toughness properties.

- Perform additional fracture testing with other methods, such as Charpy V-notch. This would be useful in providing toughness properties that could be compared to the relative toughness rankings observed from Kahn tear testing of the microstructures in this study.

- Integrate the observations from this study into a combined model to determine overall mechanical properties in the HAZ of a weld. In one such model, the welding parameters would be taken as inputs to determine the thermal cycles at different positions in the HAZ, which then would be used to determine the microstructure evolution. The microstructures modeled at different positions are then used as an input into a mechanical model that utilizes observations from this study to determine the mechanical properties in the HAZ.

Bibliography

[1] Bing Liu, X.J. Liu, and Hong Zhang. Strain-based design criteria of pipelines. *Journal of Loss Prevention in the Process Industries*, 22(6):884–888, November 2009. *(Cited on page 1.)*

[2] V. N. Marchenko and B. F. Zinko. Current trends in the development and production of steels and pipes for gas and oil pipelines: An international scientific-technical conference. *Metallurgist*, 52(3-4):167–174, 2008. *(Cited on page 1.)*

[3] Laurie E. Collins, Dengqi Bai, Fathi Hamad, and Xiande Chen. High strength spiral linepipe for strain-based pipeline designs. *The Seventeenth International Offshore and Polar Engineering Conference*, January 2007. *(Cited on pages 1 and 4.)*

[4] M. K. Gräf, H. Hillenbrand, C. J. Heckmann, and K. A. Niederhoff. High-strength large-diameter pipe for long-distance high-pressure gas pipelines. *International Journal of Offshore and Polar Engineering*, 14(1):69–74, 2004. *(Cited on page 1.)*

[5] A. C. Walker and K. A. J. Williams. Strain based design of pipelines. *The Fourteenth International Conference on Offshore Mechanics and Arctic Engineering*, 5:345–350, 1995. *(Cited on page 1.)*

[6] Koui Kim, Wei Zhou, and Scott L. Huang. Frost heave predictions of buried chilled gas pipelines with the effect of permafrost. *Cold Regions Science and Technology*, 53(3):382–396, August 2008. *(Cited on page 1.)*

[7] Jean-Marie Konrad. Estimation of the segregation potential of fine-grained soils using the frost heave response of two reference soils. *Canadian Geotechnical Journal*, 42(1):38–50, February 2005. *(Cited on page 1.)*

[8] Scott L. Huang, Matthew T. Bray, Satoshi Akagawa, and Masami Fukuda. Field investigation of soil heave by a large diameter chilled gas pipeline experiment, fairbanks, alaska. *Journal of cold regions engineering*, 18(1):2–34, 2004. *(Cited on page 1.)*

[9] A. G. Razaqpur and Daiyu Wang. Frost-induced deformations and stresses in pipelines. *International journal of pressure vessels and piping*, 69(2):105–118, 1996. *(Cited on page 1.)*

[10] T. Gladman. *The Physical Metallurgy of Microalloyed Steels*. Maney for the Institute of Materials, 1997. *(Cited on pages 4, 6, 7, 8, 9, 23, 24, 25, 26, and 28.)*

[11] ASM International Handbook Committee. *ASM Handbook, Volume 01 - Properties and Selection: Irons, Steels, and High-Performance Alloys*. ASM International, 1990. *(Cited on page 4.)*

[12] Daniel B. Lillig, Douglas S. Hoyt, Martin W. Hukle, John P. Dwyer, Agnes M. Horn, and Keith Manton. Materials and welding engineering for ExxonMobil high strain pipelines. In *The proceedings of the Sixteenth (2006) International Offshore and Polar Engineering Conference ISOPE*, volume 4. International Society of Offshore and Polar Engineers, 2006. *(Cited on page 4.)*

[13] A. J. DeArdo. Metallurgical basis for thermomechanical processing of microalloyed steels. *Ironmaking & Steelmaking*, 28(2):138–144, 2001. *(Cited on page 4.)*

[14] J. P. Ormandy, M. Strangwood, and C. L. Davis. Effect of microalloying additions on steel plate to pipe property variations during UOE linepipe processing. *Materials Science and Technology*, 19(5):595–601, May 2003. *(Cited on page 4.)*

[15] H. Okamoto. C-Fe (Carbon - Iron), C (Carbon) Binary Alloy Phase Diagrams. In *Alloy Phase Diagrams, ASM Handbook*, volume 3. ASM Handbooks Online, http://www.asmmaterials.info ASM International, 1992. *(Cited on page 5.)*

[16] Harry Bhadeshia and Robert Honeycombe. *Steels: Microstructure and Properties: Microstructure and Properties*. Butterworth-Heinemann, April 2011. *(Cited on pages 6 and 104.)*

[17] Nobutaka Yurioka. Physical metallurgy of steel weldability. *ISIJ international*, 41(6):566–570, 2001. *(Cited on page 7.)*

[18] W.T. Reynolds, F.Z. Li, C.K. Shui, and H.I. Aaronson. The Incomplete transformation phenomenon in Fe-C-Mo alloys. *Metallurgical Transactions A*, 21(6):1433–1463, 1990. *(Cited on page 8.)*

[19] Seung Youb Han, Sang Yong Shin, Chang-Hyo Seo, Hakcheol Lee, Jin-Ho Bae, Kisoo Kim, Sunghak Lee, and Nack J. Kim. Effects of Mo, Cr, and V Additions on Tensile and Charpy Impact Properties of API X80 Pipeline Steels. *Metallurgical and Materials Transactions A*, 40(8):1851–1862, August 2009. *(Cited on page 8.)*

[20] Yong-Yi Wang, David Rudland, Rudi Denys, and David Horsley. A preliminary strain-based design criterion for pipeline girth welds. In *2002 4th International Pipeline Conference*, pages 415–427. American Society of Mechanical Engineers, January 2002. *(Cited on page 9.)*

[21] William Mohr, Robin Gordon, and Robert Smith. Strain-based design guidelines for pipeline girth welds. *The Fourteenth International Offshore and Polar Engineering Conference*, 1:10–17, January 2004. *(Cited on page 9.)*

[22] Martin W. Hukle, Agnes M. Horn, Douglas S. Hoyt, and James B. LeBleu. Girth weld qualification for high strain pipeline applications. In *ASME 2005 24th International Conference on Offshore Mechanics and Arctic Engineering*, pages 369–374. American Society of Mechanical Engineers, 2005. *(Cited on page 9.)*

[23] D. P. Fairchild, M. D. Crawford, W. Cheng, M. L. Macia, N. E. Nissley, S. J. Ford, D. B. Lillig, and J. Sleigh. Girth welds for strain-based design pipelines. In *Proceedings of the 18th International Offshore and Polar Engineering Conference, Vancouver, BC, Canada*, pages 48–56. International Society of Offshore and Polar Engineers, 2008. *(Cited on page 9.)*

[24] Fathi Hamad, Xiande Chen, and Laurie Collins. High toughness, submerged arc girth weld for northern pipeline applications. In *2006 International Pipeline Conference*, pages 917–925. American Society of Mechanical Engineers, January 2006. *(Cited on page 9.)*

[25] R. A. Teale and Milton Randall. Automatic Welding Procedures For X80 Pipeline Systems. *The Third International Offshore and Polar Engineering Conference*, pages 441–444, 1993. *(Cited on page 9.)*

[26] J. A. Gianetto, J. T. Bowker, D. V. Dorling, and D. Horsley. Structure and Properties of X80 and X100 Pipeline Girth Welds. In *2004 International Pipeline Conference*, pages 1485–1497. American Society of Mechanical Engineers, January 2004. *(Cited on pages 9 and 11.)*

[27] Susan R. Fiore, James A. Gianetto, Mark G. Hudson, Suhas Vaze, Shuchi Khurana, John T. Bowker, and David V. Dorling. Development of optimized weld metal chemistries for pipeline girth welding of high strength line pipe. In *7th International Pipeline Conference*, pages 417–428. American Society of Mechanical Engineers, 2008. *(Cited on page 9.)*

[28] Masahiko Hamada, Hidenori Shitamoto, and Hiroyuki Hirata. Tensile properties and microstructure of girth welds for high strength linepipe. *The Nineteenth International Offshore and Polar Engineering Conference*, January 2009. *(Cited on pages 9 and 11.)*

[29] J. T. Bowker, J. A. Gianetto, G. Shen, W. Tyson, and D. Horsley. Cross-weld tensile properties of girth welds for strain-based designed pipelines. In *2006 International Pipeline Conference*, pages 485–496. American Society of Mechanical Engineers, 2006. *(Cited on page 9.)*

[30] Hiroyuki Motohashi and Naoto Hagiwara. Effect of Strength Matching and Strain Hardening Capacity on Fracture Performance of X80 Line Pipe Girth Welded Joint Subjected to Uniaxial Tensile Loading. *Journal of Offshore Mechanics and Arctic Engineering*, 129(4):318–326, 2007. *(Cited on page 9.)*

[31] T. A. Netto, A. Botto, and M. I. Loureno. Fatigue performance of pre-strained pipes with girth weld defects: Local deformation mechanisms under bending. *International Journal of Fatigue*, 30(6):1080–1091, June 2008. *(Cited on page 9.)*

[32] T. A. Netto, M. I. Loureno, and A. Botto. Fatigue performance of pre-strained pipes with girth weld defects: Full-scale experiments and analyses. *International Journal of Fatigue*, 30(5):767–778, May 2008. *(Cited on page 9.)*

[33] Satoshi Igi, Teruki Sadasue, Takahiro Kubo, Nobuyuki Ishikawa, and Nobuhisa Suzuki. Effect of Crack Geometry And Tensile Properties On Tensile Strain Limit of X80 Linepipe. *The Eighteenth International Offshore and Polar Engineering Conference*, January 2008. *(Cited on page 9.)*

[34] James A. Gianetto, John T. Bowker, David V. Dorling, David Taylor, David Horsley, and Susan R. Fiore. Overview of Tensile and Toughness Testing Protocols for Assessment of X100 Pipeline Girth Welds. In *2008 7th International Pipeline Conference*, pages 463–472. American Society of Mechanical Engineers, 2008. *(Cited on page 9.)*

[35] Mark G. Hudson. *Welding of X100 linepipe*. PhD thesis, Cranfield University, 2004. *(Cited on pages 11 and 12.)*

[36] Fathi Hamad, Laurie Collins, and Riny Volkers. Effect of GMAW procedure on the heat-affected zone (HAZ) toughness of X80 (grade 550) linepipe. In *7th International Pipeline Conference*, pages 553–569. American Society of Mechanical Engineers, 2008. *(Cited on pages 11, 16, 17, 29, and 31.)*

[37] Øystein Grong. *Metallurgical Modelling of Welding*. Maney Publishing, 2nd edition, 1997. *(Cited on pages 11, 13, and 15.)*

[38] Y. Chen, Y. Wang, and J. Gianetto. Thermal and microstructure simulation of high strength pipeline girth welds. In *Proceedings of the 18th International Conference on Offshore and Polar Engineering (ISOPE 2008), Vancouver, Canada*, pages 33–39, 2008. *(Cited on page 11.)*

[39] Ibrahim K. Nuruddin. *Effect of welding thermal cycles on the heat affected zone microstructure and toughness of multi-pass welded pipeline steels*. PhD thesis, Cranfield University, 2012. *(Cited on page 12.)*

[40] A. S. Bilat, A. F. Gourgues-Lorenzon, J. Besson, and A. Pineau. Brittle Fracture in Heat-Affected Zones of Girth Welds of Modern Line Pipe Steel (X100). In *Fracture of Nano and Engineering Materials and Structures*, pages 109–110. Springer, 2006. *(Cited on page 12.)*

[41] Kioumars Poorhaydari-Anaraki. *Microstructure and Property Examination of the Weld HAZ in Grade 100 Microalloyed Steel*. PhD thesis, University of Alberta, 2005. *(Cited on page 12.)*

[42] S. Kou and Y. Le. Three-dimensional heat flow and solidification during the autogenous GTA welding of aluminum plates. *Metallurgical Transactions A*, 14(11):2245–2253, 1983. *(Cited on page 12.)*

[43] S Murugan, P. V Kumar, B Raj, and M. S. C Bose. Temperature distribution during multipass welding of plates. *International Journal of Pressure Vessels and Piping*, 75(12):891–905, October 1998. *(Cited on page 13.)*

[44] V.K. Goyal, P.K. Ghosh, and J.S. Saini. Process-controlled microstructure and cast morphology of dendrite in pulsed-current gas-metal arc weld deposits of aluminum and al-mg alloy. *Metallurgical and Materials Transactions A*, 38(8):1794–1805, July 2007. *(Cited on page 13.)*

[45] V.K. Goyal, P.K. Ghosh, and J.S. Saini. Analytical studies on thermal behaviour and geometry of weld pool in pulsed current gas metal arc welding. *Journal of Materials Processing Technology*, 209(3):1318–1336, February 2009. *(Cited on page 13.)*

[46] Abhay Sharma, Ajay Kumar Chaudhary, Navneet Arora, and Bhanu K. Mishra. Estimation of heat source model parameters for twin-wire submerged arc welding. *The International Journal of Advanced Manufacturing Technology*, 45(11-12):1096–1103, December 2009. *(Cited on page 13.)*

[47] Kenneth Easterling, editor. *Introduction to the Physical Metallurgy of Welding*. Butterworth-Heinemann, 2nd edition, 1992. *(Cited on pages 13, 15, 17, and 29.)*

[48] B. de Meester. The Weldability of Modern Structural TMCP Steels. *ISIJ International*, 37(6):537–551, 1997. *(Cited on page 15.)*

[49] Shi Zhong Liu. Metallography of HSLA steel weldments. *Key Engineering Materials*, 69-70:1–20, 1992. *(Cited on page 15.)*

[50] E. A. Wilson. The gamma-alpha transformation in low carbon irons. *ISIJ International*, 34(8):615–630, 1994. *(Cited on page 15.)*

[51] George Krauss and Steven W. Thompson. Ferritic microstructures in continuously cooled low- and ultralow-carbon steels. *ISIJ International*, 35(8):937–945, 1995. *(Cited on page 15.)*

[52] G. Thewlis. Classification and quantification of microstructures in steels. *Materials Science and Technology*, 20(2):143–160, February 2004. *(Cited on page 15.)*

[53] P. L. Harrison and R. A. Farrar. Application of continuous cooling transformation diagrams for welding of steels. *International Materials Reviews*, 34(1):35–51, January 1989. *(Cited on page 15.)*

[54] G. Spanos, R. W. Fonda, R. A. Vandermeer, and A. Matuszeski. Microstructural changes in HSLA-100 steel thermally cycled to simulate the heat-affected zone during welding. *Metallurgical and Materials Transactions A*, 26(12):3277–3293, 1995. *(Cited on page 15.)*

[55] M. Shome and O. N. Mohanty. Continuous cooling transformation diagrams applicable to the heat-affected zone of HSLA-80 and HSLA-100 steels. *Metallurgical and Materials Transactions A*, 37(7):2159–2169, 2006. *(Cited on page 15.)*

[56] M. Shome, O. P. Gupta, and O. N. Mohanty. Effect of simulated thermal cycles on the microstructure of the heat-affected zone in HSLA-80 and HSLA-100 steel plates. *Metallurgical and Materials Transactions A*, 35(3):985–996, 2004. *(Cited on page 16.)*

[57] E. J. Palmiere, C. I. Garcia, and A. J. De Ardo. Compositional and microstructural changes which attend reheating and grain coarsening in steels containing niobium. *Metallurgical and Materials Transactions A*, 25(2):277–286, 1994. *(Cited on page 16.)*

[58] L. J. Cuddy and J. C. Raley. Austenite grain coarsening in microalloyed steels. *Metallurgical Transactions A*, 14(10):1989–1995, 1983. *(Cited on page 16.)*

[59] Kook-soo Bang, Chan Park, and Stephen Liu. Effects of nitrogen content and weld cooling time on the simulated heat-affected zone toughness in a Ti-containing steel. *Journal of Materials Science*, 41(18):5994–6000, September 2006. *(Cited on page 16.)*

[60] Joonoh Moon, Sanghoon Kim, Hongchul Jeong, Jongbong Lee, and Changhee Lee. Influence of Nb addition on the particle coarsening and microstructure evolution in a Ti-containing steel weld HAZ. *Materials Science and Engineering: A*, 454-455:648–653, April 2007. *(Cited on page 16.)*

[61] Sunghak Lee, Byung Chun Kim, and Dongil Kwon. Correlation of microstructure and fracture properties in weld heat-affected zones of thermomechanically controlled process steels. *Metallurgical transactions. A, Physical metallurgy and materials science*, 23 A(10):2803–2816, 1992. *(Cited on pages 16, 30, and 95.)*

[62] C. L. Davis and J. E. King. Cleavage initiation in the intercritically reheated coarse-grained heat-affected zone: Part I. Fractographic evidence. *Metallurgical and materials transactions A*, 25(3):563–573, 1994. *(Cited on pages 16, 29, 30, and 95.)*

[63] Y. Li, D. N. Crowther, M. J. W. Green, P. S. Mitchell, and T. N. Baker. The effect of vanadium and niobium on the properties and microstructure of the intercritically reheated coarse grained heat affected zone in low carbon microalloyed steels. *ISIJ international*, 41(1):46–55, 2001. *(Cited on pages 16, 29, and 95.)*

[64] E. Bonnevie, G. Ferrire, A. Ikhlef, D. Kaplan, and J.M. Orain. Morphological aspects of martensiteaustenite constituents in intercritical and coarse grain heat affected zones of structural steels. *Materials Science and Engineering: A*, 385(1-2):352–358, November 2004. *(Cited on pages 16, 29, and 95.)*

[65] Emin Bayraktar and Dominique Kaplan. Mechanical and metallurgical investigation of martensiteaustenite constituents in simulated welding conditions. *Journal of Materials Processing Technology*, 153-154:87–92, November 2004. *(Cited on pages 16 and 29.)*

[66] J. A. Gianetto, J. E. M. Braid, J. T. Bowker, and W. R. Tyson. Heat-affected zone toughness of a TMCP steel designed for low-temperature applications. *Journal of Offshore Mechanics and Arctic Engineering*, 119(2):134–144, May 1997. *(Cited on pages 16, 17, and 18.)*

[67] D. P. Fairchild, D. G. Howden, and W. A. T. Clark. The mechanism of brittle fracture in a microalloyed steel: Part i. inclusion-induced cleavage. *Metallurgical and Materials Transactions A*, 31(3):641–652, 2000. *(Cited on pages 16, 17, 18, and 30.)*

[68] S. Moeinifar, A.H. Kokabi, and H.R. Madaah Hosseini. Influence of peak temperature during simulation and real thermal cycles on microstructure and fracture properties of the reheated zones. *Materials & Design*, 31(6):2948–2955, June 2010. *(Cited on pages 16, 17, 18, 29, and 95.)*

[69] E28 Committee. Test methods for notched bar impact testing of metallic materials. Technical report, ASTM International, 2012. *(Cited on page 18.)*

[70] E08 Committee. Test method for linear-elastic plane-strain fracture toughness K_{IC} of metallic materials. Technical report, ASTM International, 2012. *(Cited on pages 18 and 19.)*

[71] E08 Committee. Test method for drop-weight tear tests of ferritic steels. Technical report, ASTM International, 2008. *(Cited on page 18.)*

[72] S. Xu, R. Bouchard, and W.R. Tyson. Simplified single-specimen method for evaluating CTOA. *Engineering Fracture Mechanics*, 74(15):2459–2464, October 2007. *(Cited on page 19.)*

[73] Ph.P. Darcis, C.N. McCowan, H. Windhoff, J.D. McColskey, and T.A. Siewert. Crack tip opening angle optical measurement methods in five pipeline steels. *Engineering Fracture Mechanics*, 75(8):2453–2468, May 2008. *(Cited on page 19.)*

[74] Hyo Kyung Sung, Seok Su Sohn, Sang Yong Shin, Sunghak Lee, Nack J. Kim, Seung Hwan Chon, and Jang Yong Yoo. Effects of finish rolling temperature on inverse fracture occurring during drop weight tear test of API X80 pipeline steels. *Materials Science and Engineering: A*, 541:181–189, April 2012. *(Cited on page 19.)*

[75] Robert Eiber. Drop-weight tear test application to natural gas pipeline fracture control. *Journal of Pipeline Engineering*, 12(3), 2013. *(Cited on page 19.)*

[76] C. Hari Manoj Simha, Su Xu, and W.R. Tyson. Non-local phenomenological damage-mechanics-based modeling of the drop-weight tear test. *Engineering Fracture Mechanics*, 118:66–82, March 2014. *(Cited on page 19.)*

[77] Richard W. Hertzberg. *Deformation and fracture mechanics of engineering materials*. John Wiley & Sons, Inc, Hoboken, NJ, 5th edition, 2013. *(Cited on pages 19, 24, and 28.)*

[78] E08 Committee. Test method for crack-tip opening displacement (CTOD) fracture toughness measurement. Technical report, ASTM International, 2008. *(Cited on page 19.)*

[79] S. Xu, N. Petri, and W.R. Tyson. Evaluation of CTOA from load vs. load-line displacement for c(t) specimen. *Engineering Fracture Mechanics*, 76(13):2126–2134, September 2009. *(Cited on page 19.)*

[80] Xian-Kui Zhu and James A. Joyce. Review of fracture toughness (G, K, J, CTOD, CTOA) testing and standardization. *Engineering Fracture Mechanics*, 85:1–46, May 2012. *(Cited on page 19.)*

[81] N.A. Kahn and E.A. Imbembo. Method of evaluating transition from shear to cleavage failure in ship plate and its correlation with large-scale plate tests. *Welding Journal*, 27(4):169–182, 1948. *(Cited on page 20.)*

[82] N.A. Kahn and E.A. Imbembo. Notch sensitivity of steel evaluated by tear test. *Welding Journal*, 28(4):153–165, 1949. *(Cited on page 20.)*

[83] N.A. Kahn and E.A. Imbembo. Further study of navy tear test. *Welding Journal*, 29(2):84–96, 1950. *(Cited on page 20.)*

[84] J.G. Kaufman and A.H. Knoll. Kahn-type tear tests and crack toughness of aluminum alloy sheet. *Materials Research and Standards*, 4(4):151–156, 1964. *(Cited on page 21.)*

[85] B07 Committee. Test method for tear testing of aluminum alloy products. Technical report, ASTM International, 2013. *(Cited on page 21.)*

[86] I Kirman. The relation between microstructure and toughness in 7075 aluminum alloy. *Metallurgical Transactions*, 2(7):1761–1770, 1971. *(Cited on page 21.)*

[87] Richard R. Senz and Edwin H. Spuhler. Fracture mechanics' impact on specifications and supply. *Metal Progress*, 107(3):64–66, 1975. *(Cited on page 21.)*

[88] D. Dumont, A. Deschamps, and Y. Bréchet. On the relationship between microstructure, strength and toughness in AA7050 aluminum alloy. *Materials Science and Engineering: A*, 356(1-2):326–336, September 2003. *(Cited on page 21.)*

[89] D. Dumont, A. Deschamps, and Y. Bréchet. A model for predicting fracture mode and toughness in 7000 series aluminium alloys. *Acta Materialia*, 52(9):2529–2540, May 2004. *(Cited on page 21.)*

[90] D. Dumont, A. Deschamps, Y. Bréchet, C. Sigli, and J. C. Ehrstrm. Characterisation of precipitation microstructures in aluminium alloys 7040 and 7050 and their relationship to mechanical behaviour. *Materials Science and Technology*, 20(5):567–576, May 2004. *(Cited on page 21.)*

[91] F Bron, J Besson, and A Pineau. Ductile rupture in thin sheets of two grades of 2024 aluminum alloy. *Materials Science and Engineering: A*, 380(1-2):356–364, August 2004. *(Cited on page 22.)*

[92] F. Bron and J. Besson. Simulation of the ductile tearing for two grades of 2024 aluminum alloy thin sheets. *Engineering Fracture Mechanics*, 73(11):1531–1552, July 2006. *(Cited on page 22.)*

[93] A. AsserinLebert, J. Besson, and A.F. Gourgues. Fracture of 6056 aluminum sheet materials: effect of specimen thickness and hardening behavior on strain localization and toughness. *Materials Science and Engineering: A*, 395(1-2):186–194, March 2005. *(Cited on page 22.)*

[94] A. Pirondi and D. Fersini. Simulation of ductile crack growth in thin panels using the crack tip opening angle. *Engineering Fracture Mechanics*, 76(1):88–100, January 2009. *(Cited on page 22.)*

[95] Mohan S. Devgun, Antonio J. Carrillo, and Tomas A. Roosen. Mechanical properties and tensile fracture characteristics of partially annealed low carbon mild steel sheet. *Materials science and engineering*, 59(1):49–57, 1983. *(Cited on page 22.)*

[96] Liang Ying, Ying Chang, Ping Hu, Guo Zhe Shen, Li Zhong Liu, and Xiao Dong Li. Influence of low tempering temperature on fracture toughness of ultra high strength boron steel for hot forming. *Advanced Materials Research*, 146-147:160–165, October 2010. *(Cited on page 22.)*

[97] D. V. Edmonds and R. C. Cochrane. Structure-property relationships in bainitic steels. *Metallurgical transactions a*, 21(6):1527–1540, 1990. *(Cited on page 23.)*

[98] C.H. Young and H.K.D.H. Bhadeshaa. Strength of mixtures of bainite and martensite. *Materials Science and Technology*, 10(3):209–214, 1994. *(Cited on page 23.)*

[99] J. Y. Koo, M. J. Luton, N. V. Bangaru, R. Petkovic, D. P. Fairchild, C. W. Petersen, H. Asahi, T. Hara, Y. Terada, and M. Sugiyama. Metallurgical design of ultra high-strength steels for gas pipelines. *International Journal of Offshore and Polar Engineering*, 14(1):2–10, 2004. *(Cited on pages 23 and 28.)*

[100] J Bouquerel, K Verbeken, and B De Cooman. Microstructure-based model for the static mechanical behaviour of multiphase steels. *Acta Materialia*, 54(6):1443–1456, April 2006. *(Cited on pages 23 and 27.)*

[101] M. Delincé, Y. Bréchet, J.D. Embury, M.G.D. Geers, P.J. Jacques, and T. Pardoen. Structure-property optimization of ultrafine-grained dual-phase steels using a microstructure-based strain hardening model. *Acta Materialia*, 55(7):2337–2350, April 2007. *(Cited on page 23.)*

[102] I.A. Yakubtsov, P. Poruks, and J.D. Boyd. Microstructure and mechanical properties of bainitic low carbon high strength plate steels. *Materials Science and Engineering: A*, 480(1-2):109–116, May 2008. *(Cited on page 23.)*

[103] Derek Hull and D. J. Bacon. *Introduction to Dislocations*. Elsevier, February 2011. *(Cited on page 24.)*

[104] F.B. Pickering and T. Gladman. Investigation into some factors which control strength of carbon steels. Technical report, Iron and Steel Institute, 1963. *(Cited on page 24.)*

[105] R. L Fleisgher. Solution hardening. *Acta Metallurgica*, 9(11):996–1000, November 1961. *(Cited on page 25.)*

[106] R. L Fleischer. Substitutional solution hardening. *Acta Metallurgica*, 11(3):203–209, March 1963. *(Cited on page 25.)*

[107] R. Labusch. A statistical theory of solid solution hardening. *physica status solidi (b)*, 41(2):659–669, January 1970. *(Cited on page 25.)*

[108] T. Gladman. Precipitation hardening in metals. *Materials Science and Technology*, 15(1):30–36, 1999. *(Cited on page 25.)*

[109] Harold J. Frost and M. F. Ashby. *Deformation-Mechanism Maps: The Plasticity and Creep of Metals and Ceramics*. Pergamon Press, Oxford Oxfordshire ; New York, 1st edition, October 1982. *(Cited on page 25.)*

[110] G. I. Taylor. The mechanism of plastic deformation of crystals. part I. theoretical. *Proceedings of the Royal Society of London. Series A*, 145(855):362–387, July 1934. *(Cited on page 26.)*

[111] G. I. Taylor. The mechanism of plastic deformation of crystals. part II. comparison with observations. *Proceedings of the Royal Society of London. Series A*, 145(855):388–404, July 1934. *(Cited on page 26.)*

[112] H. Mecking and U. F. Kocks. Kinetics of flow and strain-hardening. *Acta Metallurgica*, 29(11):1865–1875, November 1981. *(Cited on pages 26 and 98.)*

[113] Marc A Meyers and Krishan K Chawla. *Mechanical Behavior of Materials*. Cambridge University Press, 2009. *(Cited on pages 26 and 27.)*

[114] U. F. Kocks and H. Mecking. Physics and phenomenology of strain hardening: the FCC case. *Progress in Materials Science*, 48(3):171–273, 2003. *(Cited on pages 26 and 98.)*

[115] David J Horsley. Background to the use of CTOA for prediction of dynamic ductile fracture arrest in pipelines. *Engineering Fracture Mechanics*, 70(34):547–552, February 2003. *(Cited on page 27.)*

[116] P. F. Thomason. *Ductile Fracture of Metals*. Pergamon Press, 1990. *(Cited on pages 27 and 28.)*

[117] A. Pineau. Modeling ductile to brittle fracture transition in steelsmicromechanical and physical challenges. *International Journal of Fracture*, 150(1-2):129–156, June 2008. *(Cited on page 27.)*

[118] A. Pineau. Development of the local approach to fracture over the past 25 years: Theory and applications. *International Journal of Fracture*, 138(1-4):139–166, March 2006. *(Cited on page 28.)*

[119] P. Spätig, G. R. Odette, E. Donahue, and G. E. Lucas. Constitutive behavior and fracture toughness properties of the F82H ferritic/martensitic steel. *Journal of nuclear materials*, 283:721–726, 2000. *(Cited on page 29.)*

[120] Jung-Suk Lee, Jang-Bog Ju, Jae-il Jang, Woo-Sik Kim, and Dongil Kwon. Weld crack assessments in API X65 pipeline: Failure assessment diagrams with variations in representative mechanical properties. *Materials Science and Engineering A*, 373(1-2):122–130, 2004. *(Cited on page 29.)*

[121] K. L. Murty, P. Q. Miraglia, M. D. Mathew, V. N. Shah, and F. M. Haggag. Characterization of gradients in mechanical properties of SA-533B steel welds using ball indentation. *International journal of pressure vessels and piping*, 76(6):361–369, 1999. *(Cited on page 29.)*

[122] Hakan Aydin and Tracy W. Nelson. Microstructure and mechanical properties of hard zone in friction stir welded X80 pipeline steel relative to different heat input. *Materials Science and Engineering: A*, 586:313–322, December 2013. *(Cited on page 29.)*

[123] X.P. Zhang and L. Dorn. Estimation of the local mechanical properties of pipeline steels and welded joints by use of the microshear test method. *International Journal of Pressure Vessels and Piping*, 75(1):37–42, 1998. *(Cited on page 29.)*

[124] G.R. Stewart, A.M. Elwazri, R. Varano, N. Pokutylowicz, S. Yue, and J.J. Jonas. Shear punch testing of welded pipeline steel. *Materials Science and Engineering: A*, 420(1-2):115–121, March 2006. *(Cited on page 29.)*

[125] M. Kocak, L. Chen, G. Terlinde, G. Gnirss, and K.-H. Schwalbe. CTOD testing of HAZ and analysis of pop-in behavior. *Journal of Offshore Mechanics and Arctic Engineering*, 112(3):214–222, 1990. *(Cited on page 29.)*

[126] J.H. Kim and E.P. Yoon. Notch position in the HAZ specimen of reactor pressure vessel steel. *Journal of Nuclear Materials*, 257(3):303–308, 1998. *(Cited on page 29.)*

[127] Y.C. Jang, J.K. Hong, J.H. Park, D.W. Kim, and Y. Lee. Effects of notch position of the charpy impact specimen on the failure behavior in heat affected zone. *Journal of Materials Processing Technology*, 201(1-3):419–424, 2008. *(Cited on page 29.)*

[128] Kenji Ohya, Jongseop Kim, Ken'ichi Yokoyama, and Michihiko Nagumo. Microstructures relevant to brittle fracture initiation at the heat-affected zone of weldment of a low carbon steel. *Metallurgical and Materials Transactions A: Physical Metallurgy and Materials Science*, 27 A(9):2574–2582, 1996. *(Cited on pages 29 and 30.)*

[129] Koji Homma, Chitoshi Miki, and Hang Yang. Fracture toughness of cold worked and simulated heat affected structural steel. *Engineering Fracture Mechanics*, 59(1):17–28, 1998. *(Cited on page 29.)*

[130] H. Qiu, H. Mori, M. Enoki, and T. Kishi. Fracture mechanism and toughness of the welding heat-affected zone in structural steel under static and dynamic loading. *Metallurgical and Materials Transactions A*, 31(11):2785–2791, 2000. *(Cited on page 29.)*

[131] Sangho Kim, Young-Roc Im, Sunghak Lee, Hu-Chul Lee, Sung-Joon Kim, and Jun Hwa Hong. Effects of alloying elements on fracture toughness in the transition temperature region of base metals and simulated heat-affected zones of mn-mo-ni low-alloy steels. *Metallurgical and Materials Transactions A*, 35(7):2027–2037, 2004. *(Cited on page 29.)*

[132] Yaowu Shi and Zhunxiang Han. Effect of weld thermal cycle on microstructure and fracture toughness of simulated heat-affected zone for a 800MPa grade high strength low alloy steel. *Journal of Materials Processing Technology*, 207(1-3):30–39, October 2008. *(Cited on pages 29 and 30.)*

[133] Fukuhisa Matsuda, Kenji Ikeuchi, Hitoshi Okada, Ivan Hrivnak, and Hwa-Soon Park. Effect of m-a constituent on fracture behavior of 780 and 980MPa class HSLA steels subjected to weld HAZ thermal cycles. *Transactions of JWRI*, 23(2):231–238, December 1994. *(Cited on page 29.)*

[134] Astrid Lambert-Perlade, Anne-Franoise Gourgues, Jacques Besson, T. Sturel, and Andr Pineau. Mechanisms and modeling of cleavage fracture in simulated heat-affected zone microstructures of a high-strength low alloy steel. *Metallurgical and Materials Transactions A*, 35(13):1039–1053, 2004. *(Cited on page 29.)*

[135] Amer E. Amer, Min Y. Koo, Kyong H. Lee, Sang H. Kim, and Soon H. Hong. Effect of welding heat input on microstructure and mechanical properties of simulated HAZ in aCu containing microalloyed steel. *Journal of Materials Science*, 45(5):1248–1254, March 2010. *(Cited on page 29.)*

[136] Y. Li and T. N. Baker. Effect of morphology of martensiteaustenite phase on fracture of weld heat affected zone in vanadium and niobium microalloyed steels. *Materials Science and Technology*, 26(9):1029–1040, September 2010. *(Cited on pages 29 and 30.)*

[137] Yang You, Chengjia Shang, Nie Wenjin, and Sundaresa Subramanian. Investigation on the microstructure and toughness of coarse grained heat affected zone in X-100 multi-phase pipeline steel with high Nb content. *Materials Science and Engineering: A*, 558:692–701, December 2012. *(Cited on page 29.)*

[138] Peyman Mohseni. *Brittle and Ductile Fracture of X80 Arctic Steel*. PhD thesis, Norwegian University of Science and Technology, 2012. *(Cited on page 30.)*

[139] Graeme Robertson Goodall. *Welding High Strength Modern Line Pipe Steel*. PhD thesis, McGill University, 2011. *(Cited on page 31.)*

[140] Wengui Zhao, Wei Wang, Shaohui Chen, and Jinbo Qu. Effect of simulated welding thermal cycle on microstructure and mechanical properties of X90 pipeline steel. *Materials Science and Engineering: A*, 528(24):7417–7422, September 2011. *(Cited on pages 31 and 32.)*

[141] Gui Ying Qiao, Ming Zheng, Yu Gu, Xiu Lin Han, Xu Wang, Fu Ren Xiao, and Bo Liao. Mechanical properties of the heat affected zone of an x100 grade pipeline steel. *Materials Science Forum*, 773-774:795–802, November 2013. *(Cited on pages 31 and 32.)*

[142] Reza Tafteh. Personal communication. *(Cited on page 35.)*

[143] Kumkum Banerjee, Matthias Militzer, Michel Perez, and Xiang Wang. Nonisothermal austenite grain growth kinetics in a microalloyed X80 linepipe steel. *Metallurgical and Materials Transactions A*, 41(12):3161–3172, December 2010. *(Cited on pages 35, 53, and 112.)*

[144] Jenny Reichert. Personal communication, 2014. *(Cited on pages 37 and 41.)*

[145] Reza Tafteh. *Austenite decomposition in an X80 linepipe steel*. PhD thesis, University of British Columbia, 2011. *(Cited on page 41.)*

[146] Quentin Puydt. Personal communication, 2013. *(Cited on page 44.)*

[147] Jennifer M. Reichert, Thomas Garcin, Matthias Militzer, and Warren J. Poole. Formation of Martensite/Austenite (M/A) in X80 Linepipe Steel. In *2012 9th International Pipeline Conference*, pages 483–489. American Society of Mechanical Engineers, September 2012. *(Cited on pages 52, 105, and 113.)*

[148] M. Maalekian, R. Radis, M. Militzer, A. Moreau, and W. J. Poole. In situ measurement and modelling of austenite grain growth in a Ti/Nb microalloyed steel. *Acta Materialia*, 60(3):1015–1026, February 2012. *(Cited on page 95.)*

[149] H Mecking, UF Kocks, and H Fischer. Hardening, recovery, and creep in FCC mono-and polycrystals. In *Presented at the 4th Intern. Conf. on Strength of Metals and Alloys, Nancy, 30 Aug.-3 Sep. 1976*, volume 1, pages 334–339, 1976. *(Cited on page 98.)*

[150] L. M. Cheng, W. J. Poole, J. D. Embury, and D. J. Lloyd. The influence of precipitation on the work-hardening behavior of the aluminum alloys AA6111 and AA7030. *Metallurgical and Materials Transactions A*, 34(11):2473–2481, November 2003. *(Cited on page 99.)*

[151] Javier Gil Sevillano. Flow stress and work hardening. In RW Cahn, P Hassen, and EJ Kramer, editors, *Materials Science and Technology. A Comprehensive Treatment, vol. 6, VCH*, pages 19–88. Weinheim, 1993. *(Cited on page 102.)*

[152] O. Bouaziz. Revisited storage and dynamic recovery of dislocation density evolution law: Toward a generalized KocksMecking model of strain-hardening. *Advanced Engineering Materials*, 14(9):759–761, 2012. *(Cited on page 104.)*

[153] Jennifer M. Reichert, Matthias Militzer, Warren J. Poole, and Laurie Collins. A new approach using EBSD to quantitatively distinguish complex transformation products along the HAZ in X80 linepipe steel. In *2014 10th International Pipeline Conference*. American Society of Mechanical Engineers, 2014. *(Cited on page 111.)*